

Supplementary Information for:

Designed nanomolar small-molecule inhibitors of Ena/VASP EVH1 interaction impair invasion and extravasation of breast cancer cells

Matthias Barone^a, Matthias Müller^a, Slim Chiha^b, Jiang Ren^c, Dominik Albat^b, Arne Soike^b, Stephan Dohmen^b, Marco Klein^b, Judith Bruns^b, Maarten van Dinther^c, Robert Opitz^a, Peter Lindemann^a, Monika Beerbaum^a, Kathrin Motzny^a, Yvette Roske^d, Peter Schmieder^a, Rudolf Volkmer^a, Marc Nazaré^a, Udo Heinemann^d, Hartmut Oschkinat^a, Peter ten Dijke^{c,1}, Hans-Günther Schmalz^{b,1}, and Ronald Kühne^{a,1}

^aLeibniz-Forschungsinstitut für Molekulare Pharmakologie, 13125 Berlin, Germany; ^bDepartment of Chemistry, University of Cologne, Greinstraße 4, 50939 Köln, Germany; ^cOncode Institute, Department of Cell and Chemical Biology, Leiden University Medical Center, 2333 Leiden, The Netherlands; ^dMax-Delbrück-Centrum für Molekulare Medizin, 13125 Berlin, Germany

¹To whom correspondence should be addressed. E-mail: p.ten_dijke@lumc.nl, schmalz@uni-koeln.de, kuehne@fmp-berlin.de.

This PDF file includes:

Supplementary text

Figures S1 to S44

Tables S1 to S14

SI references

Methods.

Scaffold design and synthesis. Structure-based design was performed with ultra-high resolution structures using Sybyl or MOLOC. The stereoselective synthesis strategy via Ru-catalyzed ring closing metathesis and their assembly to synthetic inhibitors was performed according to the methods described before (1–8). In short, the ProM-based inhibitors were synthesized by liquid phase peptide coupling from the corresponding scaffolds according to established methodology and fully characterized (1H NMR, 13C NMR, HRMS, IR and optical rotation) as methyl esters (SI Appendix Figs. S27–S30). Ethyl esters were obtained by late stage transesterification, via saponification and re-esterification under Steglich conditions (EtOH, EDC·HCl, DMAP). For inhibitors that entered cellular assays, purity of the dissolved inhibitor batches was proven by LCMS, HPLC and MALDI analytics (SI Appendix Figs. S31–S34) while for the peptides, chimeras and inhibitors used in *in vitro* assays, characterization included HPLC traces and MALDI TOF (SI Appendix Figs. S35–S44).

Protein purification. BL21 DE3 transformed bacteria grown in 2YT medium over night were sonicated, centrifuged and supernatant loaded on glutathione sepharose high performance matrix (GE). GST-fusion protein was eluted with GSH and cleaved with thrombin over night. EVH1 domains were bound on SP sepharose ion exchange column (GE) and eluted with a NaCl gradient. Domains were re-buffered into crystallization buffer (20 mM NaCl, 5 mM TCEP, 10 mM HEPES pH 7.0) or affinity measurement buffer (40 mM sodium phosphate pH 7.3, 100 mM NaCl and 2 mM TCEP) by passing through a HiLoad 16/60 Superdex 75 size exclusion column (GE). Using vivaspin concentrators (Sartorius Stedim Biotech), Ena/VASP EVH1 domains were brought up to concentrations of 40 mg/ml and shock-frozen in liquid nitrogen for storage.

Affinity measurement: Fluorescence titration. FT experiments were carried out with a Jasco spectrofluorometer (FP-6500) at 25°C using a 10×4 mm precision cell made from quartz suprasil with conical bore for a stirring magnet (Hellma, 109.004F-QS), filled to 800 µl. Changes in the tryptophane fluorescence were detected at 340 nm, using slits opened to 1–3 nm (excitation) and 3–5 nm (emission) and a photomultiplier voltage to load the detector

with around 30% arbitrary starting signal. Ligand was titrated with 20 injections to roughly five times nominal excess. Protein concentration was set to around 5 times K_d , and ligand stock solution prepared to inject $20 \times 5 \mu\text{l}$. Depending on the protein concentration, excitation wavelength was set between 298–305 nm to keep starting protein absorbance below 0.04 cm^{-1} . Data points were averaged during one second and spacing of one minute ensured homogeneous mixing of the cell content. In total three to four replicas were made, combined with two background measurements titrating ligand into buffer. Parameters were optimized iteratively until standard errors reached less than 20% for the K_d and less than 0.5 kJ/mol for ΔG .

A one-to-one model for ligand-bound protein was assumed:

$$[\text{PL}] = \frac{1}{2} \left(P_{\text{tot}} + L_{\text{tot}} + K_d - \sqrt{(P_{\text{tot}} + L_{\text{tot}} + K_d)^2 - 4 P_{\text{tot}} L_{\text{tot}}} \right)$$

The nominal ligand concentration was multiplied by a factor $0 < M \leq 1$ to determine the amount of active ligand and the fitting procedure was carried out by an script written in R language as described earlier (6). An exhaustive list of affinities for different inhibitor compositions can be found in SI *Appendix* Tabs. S7 and S8.

Affinity measurement: Isothermal calorimetry. ITC experiments were performed at 25°C using 40 mM sodium phosphate pH 7.3, 100 mM NaCl and 1 mM DTT. Protein concentration was set to around 5 times K_d , and ligand stock solution prepared to inject $11 \times 2 \mu\text{l}$. Reference power was set to $18 \mu\text{cal/sec}$ with a stirring speed of 1000 s^{-1} and 2 s filter period. In total three to four replicas were made, combined with two background measurements titrating ligand into buffer.

A one-to-one model was assumed and the nominal ligand concentration was multiplied by a factor $0 < M \leq 1$ to determine the amount of active ligand. The fitting procedure was carried out by an script written in R language as described earlier (6).

SPOT substitution assay. SPOT array was prepared by an automated spot synthesis protocol on whatman-50-Cellulose (9). Membrane and bound peptides were washed with ethanol and washing buffer (3% (v/v) tween 20, 1x TBS pH 8.6) and subsequently blocked (5% (w/v) milk powder, 3% (v/v) tween 20, 1x TBS pH 8.6) for 3 min at room temperature. Each membrane was covered with GST-fused EVH1 domains (10 $\mu\text{l}/\text{ml}$ GST-VASP EVH1, GST-ENAH EVH1, GST-EVL EVH1, and GST) in sample buffer (3% (w/v) milk powder, 3% (v/v) tween 20, 1x TBS pH 8.6) and incubated at 7°C over night. After extensive washing, the anti GST antibody (Z-5 polyclonal rabbit IgG, Santa Cruz Biotech 200 $\mu\text{g}/\text{ml}$) was added as 1:1000 (v/v) dilution in sample buffer and incubated over night at 4°C . Membranes were then washed and covered with anti-rabbit antibody (IRDye800, Santa Cruz Biotech), diluted 1:20000 (v/v) in sample buffer. After binding took place over 45 min at room temperature, excess antibody was washed away and membranes transferred into 1x TBS. Binding was detected with fluorescence signal on Odessey infrared imaging system (Li-Cor, v2.0.40) at a resolution of $84 \mu\text{m}$.

Crystallization and structure determination. Inhibitors were added to protein solution and mixture diluted to 8–26 mg/ml. Molar excess and final concentration depended on inhibitor affinity and activity. Crystals were grown by sitting vapor-diffusion method (Art Instruments Gryphon). For initial experiments, Quiagen Sciences Suites and equal volumes of reservoir and protein-ligand solutions were used. Single, well diffracting crystals suitable for high-resolution structures were achieved by switching to micro-seeding (volume ratio reservoir:protein:seed 3:2:1) and/or adjusting temperature. Crystallization plates were stored in plate hotels (Formulatrix RockImager), in an incubator or on a precision thermal plate for temperature drift experiments. Fully grown crystals were flash-frozen in mother liquor containing 20% glycerol as cryo protectant and measured at the BESSY-II radiation light source (MX-beamlines 14.1 and 14.2 in Adlershof, Berlin). Diffraction data was indexed, processed and scaled with XDS (10–12). Molecular replacement started with unliganded EVH1 structures as search model using Phaser (13). Ligands were visible in the experimental map right after molecular replacement but were included in later rounds of model building. Non-natural ligands were built, minimized and docked with MOLOC (14) while the restraint files were generated on the PRODRG2 server (15). Peptidic chimeras were assembled in JLigand (16). All structures were refined with the PHENIX program suite (17) and rebuilt with COOT (18) and MOLOC. Of most complex structures existed multiple crystal data sets that were recorded during the process of crystal quality optimization. Isomorphous data sets were merged by XSCALE and paired refinement was carried out with the unmerged and merged data sets

at lowest resolution. For deposition, the most accurate model was chosen according to the free R value calculated at the same resolution limit (11). Final complex structures were deposited in protein data bank (rcsb.org). Diffraction and refinement statistics of all 21 complex structures are listed in the SI *Appendix* Tabs. S1-S6.

Graphical depiction. Molecular structures were rendered by Chimera (19) (v1.10.1 and v1.13.1). Chains within asymmetric units were superposed in MOLOC using the atomic positions W23NE, W23N, F77CG, Y16CG, and Q79CD to calculate a rigid body match. Inhibitors were therefore positioned over the epitope-shaping amino acids as riding atoms. For better visibility the surveying superpositions contain only one protein complex each, while in detailed views shown in the SI *Appendix* contain all chains of the asymmetric unit.

^1H - ^{15}N HSQC-measurements. Fluorescence titrations were performed prior to the HSQC NMR experiments to assess the activity of the ligand. To stably fit affinities from peak perturbations, 10-26 subsequent spectra were recorded with constant protein concentration (100-250 μM ^{15}N -labeled protein) and increasing molar ligand excess. For this, an unbound and a nearly fully ligand-saturated protein sample were prepared and spectra recorded first. Protein saturation was then increased step by step by adding ligand-bound sample to the previous experiment while the rest of the samples were stored on ice. A Hamilton syringe with a customized long needle was used to remove the entire sample (typically 200 μl initial volume) from 3 mm NMR tubes for homogeneous mixing in the low-bind Eppendorf tube of the unbound protein sample and transferring the new mixture back into the NMR tube. A script written in R language was used to optimize ligand consumption and protein saturation curves by adjusting maximal molar excess (final protein saturation), protein concentration and the ligand excess of the intermediate titration points.

HSQC spectra were recorded at 300 K with 16 scans at a resolution of 1024 (^1H) times 256 (^{15}N) complex points on an AV600 Bruker spectrometer (600 MHz proton frequency) using a 5 mm TCI cryoprobe equipped with self-shielded z-gradient and processed with TopSpin. Sparky-readable spectra were generated using bruk2ucsf to convert 2rr raw files to ucsf format and perturbations tracked in Sparky (v3.114) (20). Peak perturbation trajectories were calculated as euclidean distances of chemical shifts $\Delta\delta$ and fitted against the one-to-one binding model mentioned above:

$$f(L_{\text{tot}}) = \Delta\delta \propto [PL]$$

$$\sqrt{(\Delta\delta^1\text{H})^2 + (0.1\Delta\delta^{15}\text{N})^2} \propto [PL]$$

$$\sqrt{(\Delta\delta^1\text{H})^2 + (0.1\Delta\delta^{15}\text{N})^2} = A \left(P_{\text{tot}} + L_{\text{tot}} + K_d - \sqrt{(P_{\text{tot}} + L_{\text{tot}} + K_d)^2 - 4P_{\text{tot}}L_{\text{tot}}} \right)$$

The peak tables written by Sparky were processed, the trajectories calculated and fitted by a script written in R language. The script allowed sorting the HSQC data for certain exclusion criteria, such as minimal perturbation or goodness of the fits before producing the graphs seen in SI *Appendix* Figs. S13-S21.

Cell culture. MDA-MB-231 (ATCC HTB-26) were cultured in RPMI with 10% FBS at 37°C and 5% CO₂ atmosphere. Cells were regularly tested for absence of mycoplasma and authenticity test was performed by SNP analysis (Eurofins Genomics). MDA-MB-231 cells stably expressing mCherry were obtained by transducting pLV-mCherry lentivirally. pLV-mCherry was a gift from Pantelis Tsoulfas (Addgene plasmid # 36084 ; <http://n2t.net/addgene:36084> ; RRID: Addgene_36084).

Pulldown. Pulldown experiments were performed by N-terminally GST-tagged ENAH EVH1 (100 pmol/condition) immobilized on glutathione Sepharose 4B beads (GE) using MDA-MB-231 cell lysate (200 μl /condition) with a total protein concentration of 2 mg/ml, measured by BCA Protein Assay Kit (Novagen) UV/VIS spectroscopy (NanoDrop 1000; Thermo Scientific). Displacement of RAPH1, RIAM and Zyxin was achieved by adding different concentrations of inhibitors **1** or **6** to the lysate incubating overnight on beads at 4°C. As a control, GST alone was immobilized on the beads and treated with lysate. The Western blot with target-specific antibody against RAPH1 (H-5, scbt), RIAM (EPR2806, Abcam), Zyxin (Z4751, Sigma) and GST (Z-5, scbt) and fluorescence of secondary antibody (IRDye 800; Licor) was measured on an infrared scanner (ODYSSEY; Licor). Fluorescence signals were then processed with a script written in R language. IC50 values were fitted using

$$f(x) = \min + (\max - \min) (1 + (x/\text{IC50})^{\text{exp}})^{-1}$$

with \min and \max being the upper and lower baselines, x the ligand concentration and exp the slope steepness around IC50. Statistical difference between the IC50 values obtained for inhibitor **1** and **7** were determined by the t-test ($P=1.4\text{e-}6$).

IncuCyte chemotaxis assay. Migration of MDA-MB-231 cells toward serum was measured using the IncuCyte chemotaxis cell migration assay. We seeded 2000 cells per well in 40 μ l DMEM high glucose (GIBCO, 41966) with 0.25% FBS (Biowest, S1860-500) in the upper chamber of an IncuCyte Clearview 96-well Cell Migration Plate (Essen Bioscience, 4582). The cells were left to settle for 15 minutes at ambient temperature. Next the insert was transferred to the plate containing the chemoattractant (DMEM high glucose with 1% FBS) and the compounds. The FBS gradient over the two chambers was optimized and is shown in SI Appendix Fig. S23. The experiment was set up as triplet for the inhibitor concentrations and quadruplets for the positive (PBS) and negative controls (20 μ M PI3K inhibitor LY294002). Compounds were also added to the upper chamber so that the concentrations were equal in both chambers. Migration across the membrane was monitored by the IncuCyte S3 live cell imaging system (Essen Bioscience). Images were taken every three hours and the data was analyzed using the IncuCyte image analysis software (Essen Bioscience).

Raw data were processed with a script written in R language. Triplet and quadruplets of each condition were averaged without sorting for outliers nor zeroing the lower well signal at the beginning of the experiment. IC₅₀ values were calculated only after the phase object signal started increasing linearly and stopped before confluence in the top well reached a plateau. At these time points, the IC₅₀ was fitted using the same equation as mentioned above. Since the chemotactic response of MDA-MB-231 was lost at high inhibitor concentrations (6), *min* was forced to 0 to gain a degree of freedom (DOF) and only fits with P<0.05 for the fitted IC₅₀ coefficient were taken into account. Statistical differences between the IC₅₀ values obtained for inhibitor 1, 4a, 6, and 7 were determined by the t-test. P values are as follows: 1 vs. 4a P=6.8e-9, 1 vs. 6 P=8.4e-12, 4a vs. 6 P<2.2e-16, 6 vs. 7 P=0.55. For the IC₅₀ curves shown in the main text, the dashed lines were calculated by using the upper and lower confidence intervals of the fitted coefficients at the 99.87th percentile (3σ) and grouped DOF of 5 (8 inhibitor concentrations minus 3 fitting variables). Two graphs each using the upper or lower confidence interval were then plotted as dashed lines over the raw data and the fitted variables. For better visibility, each inhibitor signal was subsequently normalized to the fitted *max* value, even though these values varied only between 250 and 320 phase object count.

Evaluation of cancer cell extravasation in embryonic zebrafish xenograft model. Zebrafish experiments were performed at 48 hours post fertilization as described before (21). Approximately 400 mCherry-labeled MDA-MB-231 cells were injected into duct of curvier (DoC) of transgenic zebrafish embryos (*fli*:EGFP), which vasculatures are marked in green. After verification by microscope only correctly injected zebrafish were divided randomly and administrated with corresponding inhibitor treatment. Thereafter zebrafish were maintained at 34°C, a compromise for both the fish and the human cell lines. Five days after of DoC injection, the number of MDA-MB-231 cells that extravasated individually from circulation into the collagen fibres of the tail fin were analyzed under a confocal microscopy (SP5 STED, Leica Microsystems). Inhibitors were refreshed at the midterm of treatment. All experiments were repeated at least two times independently, and representative experiments are shown. Statistical differences between the control, inhibitor 1, 4a, 6, and 7 were determined by the t-test. P values are as follows: control vs. 1 P=0.26, control vs. 4a P=3.6e-9, control vs. 6 P=0.0035, control vs. 7 P=1.7e-8.

Statistics. Statistical analysis of the results was carried out with the two R packages *ggplot2* and *ggsignif*. Differences were considered significant at confidence levels greater than 95% (two-tailed). Three levels of statistical significance are distinguished and plotted in the figures of the main text: * P<0.05; ** P<0.01; *** P<0.001.

Supplementary Tables and Figures.

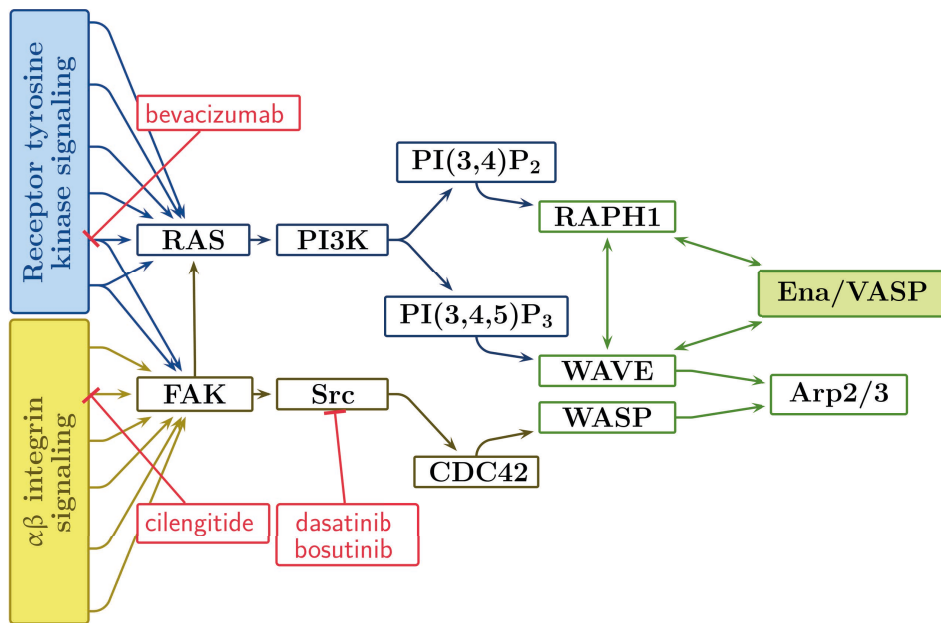


Fig. S1. Antimetastatic drugs upstream of the actin interactome

Ena/VASP proteins are elongation factors of F-actin at the very end of tumorigenic pathways (blue and yellow). Antimetastatic drugs (red) inhibit signaling towards actin-associated proteins (green) that connect the actin cytoskeleton to the extracellular matrix via integrin-mediated adhesions and invadopodia. The actin interactome is governed by weak protein-protein interactions that are transient by necessity and is therefore viewed as undruggable.

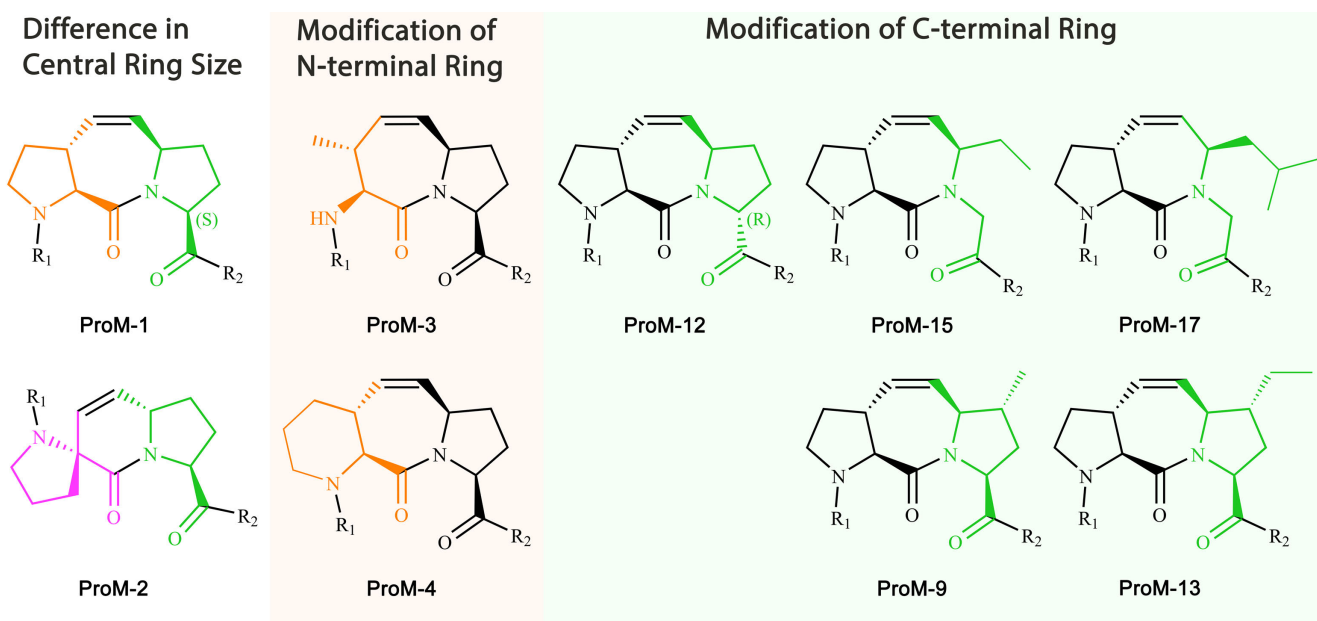


Fig. S2. Overview and relations between ProM scaffold chemical structures

Related ProM scaffolds are sorted in columns. The two initial scaffolds ProM-1 and ProM-2 differ in the central ring size. Modifications of the N-terminal ring of ProM-1 yielded ProM-3 and ProM-4 (see section on page 23 of the SI Appendix). Modifications of the C-terminal ring of ProM-1 can be divided into two categories. Scaffolds ProM-12, ProM-15, ProM-17 in the upper row were *in silico* designed to establish a polar interaction on the protein surface via their C-terminus. ProM-9 and ProM-13 on the lower row represent directed modifications to increase contact area over an apolar patch of the protein surface.

ENAH EVH1	Ac-[2-Cl-Phe] PPPP-OH	Ac-[2-Cl-Phe] PP[ProM-1]-OH	Ac-[2-Cl-Phe] PP[ProM-1]-NH ₂	Ac-[2-Cl-Phe] [ProM-1][ProM-1]- OH
<i>Diffraction statistics^a</i>				
Spacegroup	P1	P1	P3 ₁ 21	P2 ₁ 2 ₁ 2
Cell dimension [Å, °]	a=34.91 b=43.37 c=43.65 α=61.15 β=84.25 γ=84.33	a=34.76 b=43.39 c=43.59 α=61.40 β=84.03 γ=84.10	a=47.27 b=47.27 c=202.72	a=73.71 b=78.02 c=80.85
Resolution [Å]	38–1.49 (1.58–1.49)	38–1.16 (1.23–1.16)	41–1.80 (1.91–1.80)	45–1.46 (1.55–1.46)
Unique reflections	33987 (5476)	71797 (11195)	25337 (4010)	81310 (12951)
Completeness [%]	93.0 (92.6)	93.1 (90.0)	99.4 (99.7)	99.7 (99.6)
Redundancy	2.7.7)	2.0 (1.9)	5.4 (5.6)	5.4 (5.5)
$\langle I/\sigma \rangle_{\text{mrgd}}$	12.58 (1.36)	11.24 (1.86)	14.61 (1.49)	11.79 (1.66)
CC _{1/2}	99.9 (59.5)	99.9 (82.6)	99.9 (58.1)	99.8 (62.1)
R _{meas} ^b [%]	5.5 (96.5)	4.8 (51.7)	8.6 (113)	9.6 (101)
IS _a	26.18	36.57	45.41	21.62
<i>Refinement statistics</i>				
Solvent content [%]	45.5	45.9	52.3	46.2
V _M [Å ³ /Da]	2.26	2.25	2.58	2.28
Molecules per AU	2	2	2	4
R _{fact} ^c [%]	17.9	13.9	20.21	17.8
R _{free} ^d [%]	20.1	14.1	21.66	19.9
rmsd _{bond} [Å]	0.06	0.01	0.007	0.008
rmsd _{angle} [°]	1.2	1.7	1.4	1.28
PDB code	5N91	5N9C	5N9P	5NAJ

^a Numbers in parentheses correspond to outer shell

^b R_{meas}: redundancy-independent R factor

^c R_{fact}= $\sum |F_0 - F_c| / \sum |F_0|$ (22)
the observed and calculated structure factors

^d R_{free} set contains 5% of total reflections (23)

Tab. S1. Diffraction and refinement statistics

Deposited crystal structures with ProM-1-based inhibitor compositions successfully replacing the core motif of ActA-derived peptide FPPPP.

ENAH EVH1	Ac-[2-Cl-Phe] [ProM-2] [ProM-1]-NH ₂	Ac-[2-Cl-Phe] [ProM-2] [ProM-1]-OH	Ac-[2-Cl-Phe] [ProM-2] [ProM-3]-OH	Ac-[2-Cl-Phe] [ProM-2] [ProM-4]-OH				
Inhibitor number	1b							
<i>Diffraction statistics^a</i>								
Spacegroup	C222 ₁	C222	P2	P1				
Cell dimension [Å, °]	a=24.70 b=60.69 c=89.06	a=89.83 b=131.42 c=35.56	a=34.61 b=38.25 c=44.00 β=90.59	a=34.72 b=43.36 c=44.18 α=60.97 β=84.19 γ=84.16				
Resolution [Å]	46–1.36 (1.47–1.36)	32–1.7 (1.74–1.70)	44–1.15 (1.22–1.15)	50–1.40 (1.48–1.40)				
Unique reflections	20643 (4246)	23659 (1704)	38436 (6060)	41864 (6668)				
Completeness [%]	100 (100)	99.8 (99.9)	93.5 (92.0)	94.6 (93.3)				
Redundancy	14 (15)	4 (4.1)	2.2 (2.1)	2.3 (2.3)				
$\langle I/\sigma \rangle_{\text{mrgd}}$	11.48 (0.61)	12.86 (2.35)	13.15 (1.44)	10.39 (1.12)				
CC _{1/2}	99.9 (27.3)	99.8 (76.8)	99.9 (59.1)	99.9 (60.2)				
R _{meas} ^b [%]	13.1 (535)	8.2 (64.6)	4.5 (78.2)	7.3 (99.5)				
IS _a	14.62	19.92	34.82	36.01				
<i>Refinement statistics</i>								
Solvent content [%]	33.3	40.9	47.2	46.3				
V _M [Å ³ / Da]	1.84	2.08	2.33	2.29				
Molecules per AU	1	2	1	2				
R _{fact} ^c [%]	20.1	19.0	15.7	22.0				
R _{free} ^d [%]	23.6	23.6	18.6	26.0				
rmsd _{bond} [Å]	0.01	0.01	0.01	0.009				
rmsd _{angle} [°]	1.6	1.6	1.60	1.16				
PDB code	7AKI	4MY6	5NBF	5NCF				

^a Numbers in parentheses correspond to outer shell

^b R_{meas}: redundancy-independent R factor

^c R_{fact} = $\sum |F_0 - F_c| / \sum |F_0|$ (22)
the observed and calculated structure factors

^d R_{free} set contains 5% of total reflections (23)

Tab. S2. Diffraction and refinement statistics

Deposited crystal structures of ProM-2-based inhibitors composed of unsuccessful modifications on the N-terminal building blocks ProM-3 and ProM-4. These scaffolds are discussed in the SI Appendix on pages 23 and 24.

ENAH EVH1	Ac-W ¹ PPPP TEDEL-NH ₂	Ac-[2-Cl-Phe] PPPP TEDEL-NH ₂	Ac-[2-Cl-Phe] PPPP TEDDL-NH ₂	Ac-[2-Cl-Phe] PPPP TEDEA-NH ₂
<i>Diffraction statistics^a</i>				
Spacegroup	C2	C2	P1	P1
Cell dimension [Å, °]	a=187.92 b=34.42 c=110.96 β=91.53	a=147.78 b=44.02 c=34.67 β=102.13	a=34.65 b=44.28 c=43.16 α=60.85 β=84.04 γ=84.01	a=34.74 b=43.19 44.01 α=61.04 β=84.20 γ=84.21
Resolution [Å]	48–2.70 (2.80–2.70)	42–1.58 (1.68–1.58)	39–1.40 (1.48–1.40)	38–1.48 (1.59–1.48)
Unique reflections	20211 (2039)	29131 (4618)	42224 (6456)	35565 (6688)
Completeness [%]	98.8 (100)	96.8 (95.7)	96.0 (95.2)	95.7 (93.5)
Redundancy	5.3 (5.3)	2.3 (2.3)	3.8 (3.8)	3.1 (2.8)
$\langle I/\sigma \rangle_{\text{mrgd}}$	8.60 (1.53)	10.23 (1.47)	9.48 (1.00)	3.86 (0.58)
CC _{1/2}	98.9 (58.7)	99.8 (60.5)	99.8 (47.9)	98.4 (37.6)
R _{meas} ^b [%]	23.0 (153)	8.5 (97.5)	9.3 (155)	22.1 (194)
ISa	18.40	29.34	21.81	22.88
<i>Refinement statistics</i>				
Solvent content [%]	65.2	44.2	45.6	45.5
V _M [Å ³ /Da]	3.53	2.20	2.26	2.26
Molecules per AU	4	2	2	2
R _{fact} ^c [%]	20.1	24.6	20.1	24.6
R _{free} ^d [%]	27.0	19.9	23.1	26.9
rmsd _{bond} [Å]	0.009	0.01	0.009	0.024
rmsd _{angle} [°]	1.10	1.17	1.63	1.67
PDB code	5NC7	5NC2	6XVT	6XXR

^a Numbers in parentheses correspond to outer shell

^b R_{meas}: redundancy-independent R factor

^c R_{fact}= $\sum |F_0 - F_c| / \sum |F_0|$ (22)
the observed and calculated structure factors

^d R_{free} set contains 5% of total reflections (23)

Tab. S3. Diffraction and refinement statistics

Deposited crystal structures with C-terminally elongated ActA-derived peptide Ac-¹F²PPPTEDEL-NH₂ as well as the single point mutations from ⁹Glu to ⁹Asp and ¹⁰Leu to ¹⁰Ala (Relative affinity losses of these two peptides are found in SI Appendix Fig. S4c).

ENAH EVH1	Ac-[2-Cl-Phe] PP[ProM-1] TEDEL-NH ₂	Ac-[2-Cl-Phe] [ProM-2][ProM-1] TEDEL-NH ₂
Inhibitor number	2ΔN	
<i>Diffraction statistics^a</i>		
Spacegroup	C2	C2
Cell dimension [Å, °]	a=149.74 b=44.24 c= 34.83 β=101.47	a=148.39 b=44.00 c= 34.83 β=102.17
Resolution [Å]	42–1.45 (1.54–1.45)	42–1.00 (1.06–1.00)
Unique reflections	39592 (6309)	118323 (18886)
Completeness [%]	99.4 (99.2)	99.9 (99.7)
Redundancy	3.3 (3.1)	14 (13)
$\langle I/\sigma \rangle_{\text{mrgd}}$	7.69 (1.32)	5.26 (0.0)
CC _{1/2}	98.9 (58.7)	98.8 (14.4)
R _{meas} ^b [%]	11.3 (104)	23.9 (-99.9)
ISa	13.37	23.36
<i>Refinement statistics</i>		
Solvent content [%]	44.7	44.3
V _M [Å ³ / Da]	2.22	2.21
Molecules per AU	2	2
R _{fact} ^c [%]	18.2	19.8
R _{free} ^d [%]	20.4	22.4
rmsd _{bond} [Å]	0.004	0.016
rmsd _{angle} [°]	0.977	1.58
PDB code	5ND0	6RD2

^a Numbers in parentheses correspond to outer shell

^b R_{meas}: redundancy-independent R factor

^c R_{fact}= $\sum |F_0 - F_c| / \sum |F_0|$ (22)
the observed and calculated structure factors

^d R_{free} set contains 5% of total reflections (23)

Tab. S4. Diffraction and refinement statistics

Deposited crystal structures with C-terminally elongated ActA-derived, ProM-containing chimeras.

ENAH EVH1	Ac-[2-Cl-Phe] [ProM-2] [ProM-12]-OH	Ac-[2-Cl-Phe] [ProM-2] [ProM-12]-OMe	Ac-[2-Cl-Phe] [ProM-2] [ProM-15]-OH	Ac-[2-Cl-Phe] [ProM-2] [ProM-15]-OMe
Inhibitor number	3b	3a	4b	4a
<i>Diffraction statistics^a</i>				
Spacegroup	C222	C2	C222	C222
Cell dimension [Å, °]	a=44.14 b=141.37 c=34.71 β=96.93	a=136.15 b=34.57 c=44.24	a=43.38 b=141.46 c=34.80	a=44.00 b=141.53 c=34.73
Resolution [Å]	42–1.65 (1.75–1.65)	44–1.42 (1.50–1.42)	41–1.10 (1.17–1.10)	42–1.35 (1.43–1.35)
Unique reflections	13548 (2144)	38981 (5889)	42538 (6649)	24264 (3860)
Completeness [%]	99.9 (100)	99.9 (99.9)	96.5 (94.4)	99.4 (99.5)
Redundancy	8.5 (8.4)	6.4 (5.8)	6.5 (6.6)	6.5 (6.4)
$\langle I/\sigma \rangle_{\text{mrgd}}$	9.14 (0.97)	11.46 (1.25)	9.43 (0.55)	13.69 (1.21)
CC _{1/2}	99.7 (43.3)	99.9 (59.3)	99.9 (27.8)	99.9 (56.3)
R _{meas} ^b [%]	20 (210)	12 (170)	9.3 (310)	8.0 (143)
ISa	19.13	17.26	18.54	27.72
<i>Refinement statistics</i>				
Solvent content [%]	42.3	39.5	41.5	42.2
V _M [Å ³ /Da]	2.13	2.03	2.10	2.13
Molecules per AU	1	2	1	1
R _{fact} ^c [%]	18.3	17.0	16.5	17.1
R _{free} ^d [%]	20.8	19.8	20.1	20.2
rmsd _{bond} [Å]	0.009	0.02	0.019	0.020
rmsd _{angle} [°]	1.27	1.86	1.69	1.88
PDB code	5NCP	5NDU	6RCF	6RCJ

^a Numbers in parentheses correspond to outer shell

^b R_{meas}: redundancy-independent R factor

^c R_{fact}= $\sum |F_0 - F_c| / \sum |F_0|$ (22)
the observed and calculated structure factors

^d R_{free} set contains 5% of total reflections (23)

Tab. S5. Diffraction and refinement statistics

Deposited crystal structures with scaffolds yielded through structure-based drug design. These scaffolds allow replacement of the core motif of ActA-derived peptide Ac–FPPPTTEDEL–NH₂ and mimic the polar interaction of TEDEL.

ENAH EVH1	Ac-[2-Cl-Phe] [ProM-2] [ProM-17]-OMe	Ac-[2-Cl-Phe] PP [ProM-9]-OH	Ac-[2-Cl-Phe] [ProM-2] [ProM-9]-OH	Ac-[2-Cl-Phe] [ProM-2] [ProM-13]-OEt
Inhibitor number	5a	6c	6b	7
<i>Diffraction statistics^a</i>				
Spacegroup	C222 ₁	C222	P2 ₁ 2 ₁ 2 ₁	P2
Cell dimension [Å, °]	a=35.15 b=61.36 c=88.94	a=90.15 b=131.52 c=35.68	a=35.02 b=61.27 c=89.26	a=34.81 b=44.36 c=72.47 β=90.56
Resolution [Å]	30–0.78 (0.85–0.78)	45–1.65 (1.75–1.65)	36–1.02 (1.08–1.02)	44–1.29 (1.39–1.29)
Unique reflections	106735 (23284)	25469 (3536)	172743 (26288)	53114 (9979)
Completeness [%]	97.7 (94.7)	97.3 (85.3)	91.4 (86)	99.4 (69.4)
Redundancy	19.0 (15.8)	4.1 (2.8)	3.0 (2.9)	4.7 (2.7)
<I>/σ(I)>	23.1 (1.1)	12.7 (1.7)	12.4 (2.49)	6.76 (1.94)
CC _{1/2}	100 (53.9)	99.8 (60.7)	99.9 (80.1)	99.4 (76.4)
R _{meas} ^b [%]	5.1 (281)	8.6 (74.6)	6.2 (52.6)	15.6 (65.6)
IS _a	26.65	21.54	25.51	19.34
<i>Refinement statistics</i>				
Solvent content [%]	34.8	41.0	34.7	43.8
V _M [Å ³ /Da]	1.89	2.08	1.88	2.19
Molecules per AU	1	2	2	2
R _{fact} ^c [%]	12.0	16.5	12.4	15.1
R _{free} ^d [%]	14.0	19.4	15.0	19.0
rmsd _{bond} [Å]	0.022	0.01	0.01	0.008
rmsd _{angle} [°]	2.38	1.26	1.72	1.21
PDB code	7A5M	5NBX	5NCG	5NEG

^a Numbers in parentheses correspond to outer shell

^b R_{meas}: redundancy-independent R factor

^c R_{fact}= $\sum|F_0 - F_c|/\sum|F_0|$ (22)

the observed and calculated structure factors

^d R_{free} set contains 5% of total reflections (23)

Tab. S6. Diffraction and refinement statistics

Deposited crystal structures with scaffolds yielded through structure-based drug design. These scaffolds allow replacement of the core motif of ActA-derived peptide Ac-FPPPTEDEL-NH₂ and mimic the polar (ProM-17) or hydrophobic (ProM-9 and ProM-13) interaction of TEDEL.

	ENAH EVH1 + inhibitor composition					$K_{d,FT}$ [μM]	ΔG [kJ/mol]
wt2	Ac-SFE	F	PP	PP	TEDEL-NH ₂	13 (1)	-27.9 (0.1)
	Ac-SFE	[2-Cl-Phe]	PP	PP	TEDEL-NH ₂	0.79 (0.05)	-34.8 (0.2)
	Ac-SFE	[2-Cl-Phe]	PP	PP	TEDDL-NH ₂	1.43 (0.09)	-33.4 (0.1)
	Ac-	[2-Cl-Phe]	PP	PP	TEDEL-NH ₂	1.25 (0.04)	-33.7 (0.07)
	Ac-	[2-Cl-Phe]	PP	PP	TEDDL-NH ₂	3.8 (0.2)	-30.9 (0.1)
	Ac-	[2-Cl-Phe]	PP	PP	TEDEA-NH ₂	3.5 (0.1)	-31.4 (0.1)
	Ac-	[2-Cl-Phe]	PP	[ProM-1]	TEDEL-NH ₂	0.60 (0.04)	-35.5 (0.2)
	Ac-SFE	[2-Cl-Phe]	PP	PP	-OH	4.6 (0.2)	-30.5 (0.1)
	Ac-SFE	F	[ProM-2]	PP	TEDEL-NH ₂	12 (1)	-28.2 (0.3)
	Ac-SFE	F	[ProM-2]	PP	TEDEL-NH ₂	8 (1)	-29.1 (0.3)
	Ac-	F	PP	PP	-OH	500 (70)	-19 (0.4)
wt1	Ac-	F	PP	PP	-OEt	153 (8)	-21.8 (0.1)
	Ac-	[2-Cl-Phe]	PP	PP	-OH	9.9 (0.8)	-28.6 (0.2)
1c	Ac-	[2-Cl-Phe]	PP	[ProM-1]	-OH	2.4 (0.4)	-32.0 (0.4)
1b	Ac-	[2-Cl-Phe]	[ProM-2]	[ProM-1]	-OH	2.3 (0.2)	-32.2 (0.2)
1	Ac-	[2-Cl-Phe]	[ProM-2]	[ProM-1]	-OEt	4.1 (0.3)	-30.8 (0.2)
	Ac-	[2-Cl-Phe]	[ProM-2]	[ProM-4]	-OH	3.0 (0.3)	-31.5 (0.2)
	Ac-	[2-Cl-Phe]	[ProM-2]	[ProM-3]	-OH	9.7 (0.8)	-28.6 (0.2)
	Ac-SFE	[2-Cl-Phe]	PP	[ProM-1]	TEDEL-NH ₂	0.21 (0.05)	-38.1 (0.6)
2	Ac-SFE	[2-Cl-Phe]	[ProM-2]	[ProM-1]	TEDEL-NH ₂	0.15 (0.02)	-38.9 (0.2)
6c	Ac-	[2-Cl-Phe]	PP	[ProM-9]	-OH	0.23 (0.05)	-37.9 (0.5)
6b	Ac-	[2-Cl-Phe]	[ProM-2]	[ProM-9]	-OH	0.12 (0.02)	-39.5 (0.3)
6	Ac-	[2-Cl-Phe]	[ProM-2]	[ProM-9]	-OEt	0.38 (0.05)	-36.6 (0.3)
7	Ac-	[2-Cl-Phe]	[ProM-2]	[ProM-13]	-OEt	0.12 (0.01)	-39.5 (0.3)
3a	Ac-	[2-Cl-Phe]	[ProM-2]	[ProM-12]	-OMe	15 (1)	-27.6 (0.2)
3b	Ac-	[2-Cl-Phe]	[ProM-2]	[ProM-12]	-OH	13.5 (0.5)	-27.8 (0.1)
4a	Ac-	[2-Cl-Phe]	[ProM-2]	[ProM-15]	-OMe	0.47 (0.03)	-36.1 (0.1)
4b	Ac-	[2-Cl-Phe]	[ProM-2]	[ProM-15]	-OH	0.32 (0.04)	-37.0 (0.3)
5a	Ac-	[2-Cl-Phe]	[ProM-2]	[ProM-17]	-OMe	0.53 (0.09)	-35.8 (0.4)

Tab. S7. Affinities of inhibitor compositions binding to ENAH EVH1

Binding studies based on fluorescence titration (FT) using ENAH EVH1 at 25 °C. Chemical structures of the mentioned ProM scaffolds are printed in SI Appendix Fig. S2.

	VASP EVH1 + inhibitor composition					$K_{d,FT}$ [μM]	ΔG [kJ/mol]
wt2	Ac-SFE	F	PP	PP	TEDEL-NH ₂	19 (2)	-26.9 (0.3)
	Ac-SFE	[2-Cl-Phe]	PP	PP	TEDEL-NH ₂	1.5 (0.3)	-33.3 (0.5)
	Ac-SFE	F	[ProM-1]	PP	TEDEL-NH ₂	40 (4)	-25.1 (0.2)
	Ac-SFE	F	PP	[ProM-1]	TEDEL-NH ₂	5.7 (0.3)	-29.9 (0.1)
	Ac-SFE	F	[ProM-1]	[ProM-1]	TEDEL-NH ₂	19 (6)	-26.9 (0.8)
	Ac-	F	PP	PP	-OH	800 (80)	-17.7 (0.2)
	Ac-	[2-Cl-Phe]	PP	PP	-OH	13 (2)	-27.8 (0.3)
1c	Ac-	[2-Cl-Phe]	PP	[ProM-1]	-OH	3.2 (0.3)	-31.4 (0.3)
1b	Ac-	[2-Cl-Phe]	[ProM-2]	[ProM-1]	-OH	2.3 (0.1)	-32.2 (0.2)
1	Ac-	[2-Cl-Phe]	[ProM-2]	[ProM-1]	-OEt	6.3 (0.6)	-29.7 (0.3)
	Ac-	[2-Cl-Phe]	[ProM-2]	[ProM-4]	-OH	1.6 (0.2)	-33.1 (0.4)
	Ac-SFE	[2-Cl-Phe]	PP	[ProM-1]	TEDEL-NH ₂	0.31 (0.05)	-37.2 (0.4)
2	Ac-SFE	[2-Cl-Phe]	[ProM-2]	[ProM-1]	TEDEL-NH ₂	0.25 (0.07)	-37.7 (0.7)
	Ac-SFE	[2-Cl-Phe]	PP	[ProM-3]	TEDEL-NH ₂	1.5 (0.2)	-33.2 (0.3)
	Ac-SFE	[2-Cl-Phe]	[ProM-1]	[ProM-1]	TEDEL-NH ₂	0.3 (0.1)	-37.1 (0.8)
6c	Ac-	[2-Cl-Phe]	PP	[ProM-9]	-OH	0.38 (0.09)	-36.7 (0.5)
6b	Ac-	[2-Cl-Phe]	[ProM-2]	[ProM-9]	-OH	0.28 (0.06)	-37.4 (0.5)
6	Ac-	[2-Cl-Phe]	[ProM-2]	[ProM-9]	-OEt	0.78 (0.09)	-34.9 (0.3)
7	Ac-	[2-Cl-Phe]	[ProM-2]	[ProM-13]	-OEt	0.4 (0.1)	-36.6 (0.6)

Tab. S8. Affinities of inhibitor compositions binding to VASP EVH1

Binding studies based on fluorescence titration (FT) using VASP EVH1 at 25 °C. Chemical structures of the mentioned ProM scaffolds are printed in SI Appendix Fig. S2.

	2	1	6	7
VASP EVH1				
$K_{d,FT}$ [nM]	250 (70)	6200 (600)	780 (90)	400 (100)
$K_{d,ITC}$ [nM]	560 (40)	9400 (500)	1400 (200)	490 (60)
ENAH EVH1				
$K_{d,FT}$ [nM]	150 (60)	4100 (300)	380 (50)	120 (10)
$K_{d,ITC}$ [nM]	340 (30)	7800 (400)	800 (100)	310 (40)
EVL EVH1				
$K_{d,FT}$ [nM]	190 (60)	4100 (500)	280 (50)	130 (20)
$K_{d,ITC}$ [nM]	260 (10)	5800 (700)	670 (70)	280 (30)
	2	1	6	7
VASP EVH1				
LE_{FT} [$J(\text{mol HA})^{-1}$]	-330 (6)	-590 (6)	-680 (6)	-700 (10)
LE_{ITC} [$J(\text{mol HA})^{-1}$]	-310 (2)	-570 (2)	-660 (6)	-690 (6)
ENAH EVH1				
LE_{FT} [$J(\text{mol HA})^{-1}$]	-340 (9)	-620 (4)	-720 (6)	-760 (6)
LE_{ITC} [$J(\text{mol HA})^{-1}$]	-320 (2)	-580 (4)	-680 (4)	-710 (6)
EVL EVH1				
LE_{FT} [$J(\text{mol HA})^{-1}$]	-330 (7)	-610 (6)	-730 (8)	-750 (8)
LE_{ITC} [$J(\text{mol HA})^{-1}$]	-327 (1)	-600 (8)	-690 (6)	-720 (6)

Tab. S9. Comparison of affinities and ligand efficiencies of final inhibitors **6 and **7** with parent inhibitor **1****

7 regained the affinity of the peptidic chimera **2** by introducing only two heavy atoms (HA). The improved ligand efficiency (LE: ΔG per HA) for both inhibitors **6** and **7** justified the increase of the molecular weight.

SPOT substitution assay. Single residue substitution experiments are reported only for VASP EVH1 (24). SPOT array substitution for all three Ena/VASP EVH1 paralogs revealed two conserved binding epitopes within the main binding groove that accepted other amino acids than the core motif sequence $^1\text{FPPPP}$. The first epitope, a deep pocket that EVH1 domains provide for ^1Phe , was optimized earlier (6). Optimization of the second epitope, a apolar patch formed by Phe77 that contacts ^4Pro (orange), was not successful. The structural insights of the scaffold modifications to probe this apolar patch are discussed here in the SI Appendix on pages 23-24.

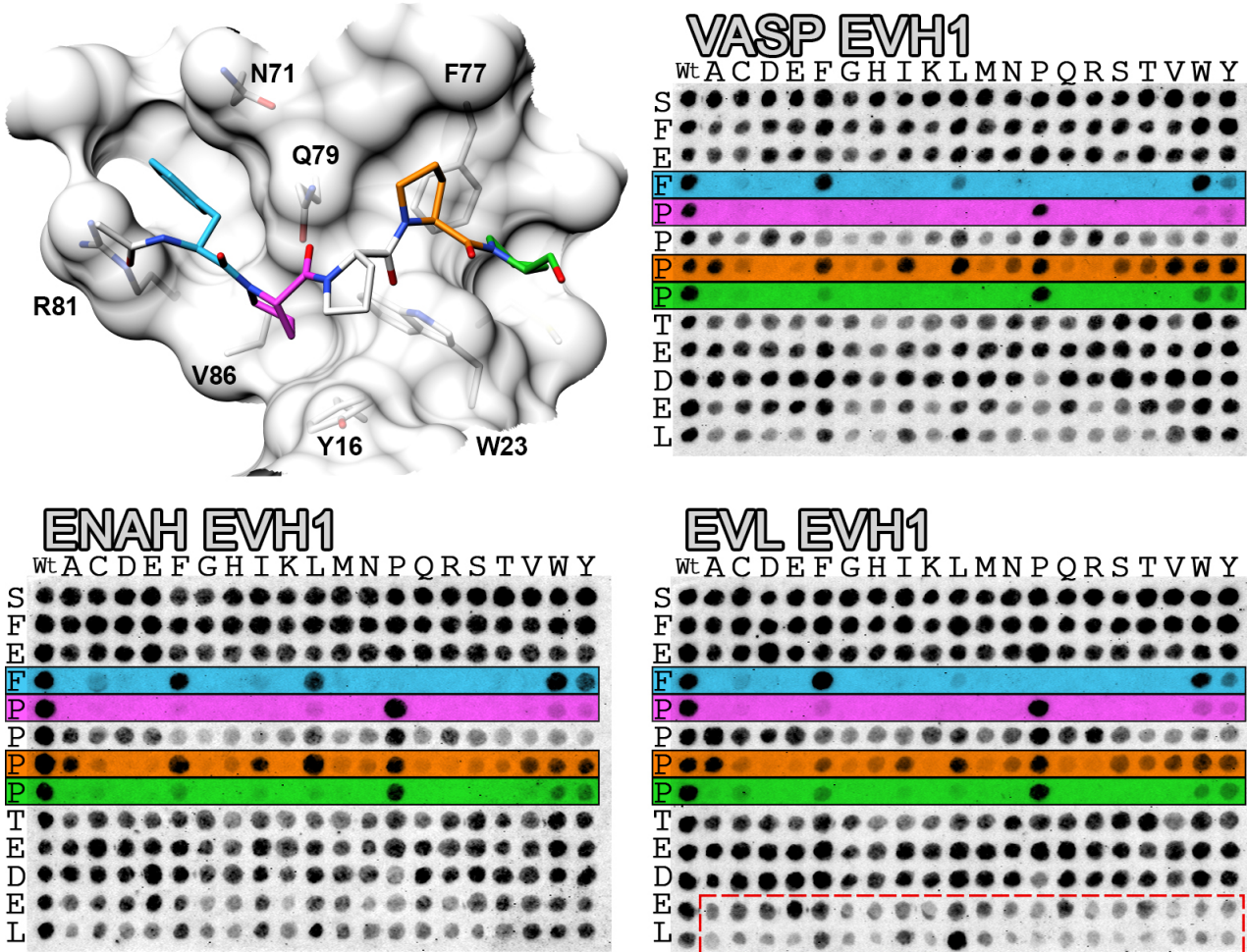


Fig. S3. Substitution spot array of *L. monocytogenes*' surface protein ActA-derived peptide SFEFPPPTEDEL, color-coded according to the crystal structure of Ac-FPPPPT bound to Mena EVH1 (PDB code 1EVH). ENAH-, VASP-, and EVL EVH1 reveal a PxxP-binding mode in which the first and last proline can not be exchanged at all. Ena/VASP accepts for the preceding Phe of the core motif mainly aromatic residues but also Leu, while exchange to aliphatic residues are valid instead of the third proline. A more intimate contact of the terminal residues Glu-Leu of TEDEL is visible from more thinned out spots compared to the preceding TED, even though no clear recognition pattern is notable (best visible on EVL EVH1).

The conformation of TEDEL. Two of the crystallized ligands resembled the proline-rich core of the **wt2** peptide, the other two ligand compositions contained the scaffold ProM-1 designated to mimic the additional interactions (SI Appendix Fig. S4a). Consistent with our finding, the secondary structure prediction server PSIPRED (25, 26) calculates helix propensity for amino acids succeeding Thr for all four proline-rich repeats (27, 28) of ActA. Within the flanking epitope, ⁶Thr is solvent-exposed but conserved in all four repeats of ActA, emphasizing its function as helix capping motif (29).

a

	Ligand composition	Resolution	PDB code
	Ac-WPPPTEDEL-NH ₂	2.8 Å	5NC7
	Ac-[2-Cl-Phe]PPPTEDEL-NH ₂	1.6 Å	5NC2
	Ac-[2-Cl-Phe]PP[ProM-1]TEDEL-NH ₂	1.45 Å	5ND0
2ΔN	Ac-[2-Cl-Phe][ProM-2][ProM-1]TEDEL-NH ₂	1.00 Å	6RD2

b



c

	Ligand composition	K _{d,FT} [μM]	ΔG [kJ/mol]	ΔΔG [kJ/mol]	PDB code
	Ac-[2-Cl-Phe]PPPTEDEL-NH ₂	1.25 (0.04)	-33.7 (0.07)	(ref)	5NC2
	Ac-[2-Cl-Phe]PPPTEDDL-NH ₂	3.8 (0.2)	-30.9 (0.1)	+2.8 (0.1)	6XVT
	Ac-[2-Cl-Phe]PPPTEDEA-NH ₂	3.5 (0.1)	-31.4 (0.1)	+2.3 (0.1)	6XXR

Fig. S4. Structure of the second binding epitope of *L. monocytogenes*' surface protein ActA

(a) Complex structures of four TEDEL-containing ligand compositions were crystallized. (b) The proline-rich portion of the 10-mer adopts PPII conformation (blue), whereas the ⁷EDEL forms an α-helical loop (yellow). Ramachandran inlay shows the according phi/psi backbone angles of the TEDEL residues. Superposition of 27 ENAH EVH1 chains of 12 asymmetric units reveals a stable and conserved protein epitope as well as TEDEL binding canonically to the domain, independent of the presence of ProM scaffolds (represented by ribbons calculated by the backbone atoms within). (c) Single point mutations from ⁹Glu to ⁹Asp, as well as ¹⁰Leu to ¹⁰Ala loose significant affinity for ENAH EVH1. The crystal structures of ENAH EVH1 with either point-mutated peptide reveal very weak electron density or even an unresolved α-helical portion after Thr. Interestingly however, the conserved water bound to W23NH is clearly visible in both complex structures, indicating that the loop structures with either point mutation might be severely disturbed, allowing the water molecule to remain bound to W23NH in the crystal packing.

Ligands of Homer- and ENAH EVH1 use a diametric binding mode to access the hydrophobic patch. The mGluR-derived peptide ¹TPPSPF is the only known ligand that interacts close to the hydrophobic patch that binds TEDEL. ¹TPPSPF is recognized by Homer EVH1, a class II EVH1 domain displaying crucial point mutations in both epitopes that bind ¹Phe and ⁹EL of ¹FPPPTEDEL to ENAH EVH1. The C-terminal cleft hosting ¹Phe is nonexistent on Homer1 EVH1 due to two mutations (R81A and Y16I) that flatten the surface of Homer EVH1 and allow TPPSPF to bind C-terminally shifted within the binding groove (SI Appendix Fig. S5a). The hydrophobic patch around of Phe77 and Met14 is also flattened due to an Asn90 to Gly89 mutation (SI Appendix Fig. S5b), which alters the epitope severely. ¹TPPSPF adopts a unique conformation with ³Pro adopting *cis*-conformation, followed by a tight type VIa β -turn that brings ⁶Phe straight down over Homer EVH1 Gly89 (30). The tight turn within the ligand and the conserved Gly89 are crucial to provide enough space for ⁶Phe to access the patch (30). Like Gly89 in Homer EVH1, the solvent-exposed Asn90 is conserved among the Ena/VASP EVH1 domains and sterically blocks the volume needed for ligands accessing the hydrophobic patch with a binding mode seen by ¹TPPSPF. Hence, the hydrophobic patch is reachable only from the other side and seems to require a second intermolecular contact via W23NH to stabilize the hydrophobic interaction. SI Appendix Fig. S5b highlights that ¹⁰Leu of TEDEL and ⁶Phe of TPPSPF bind to the same hydrophobic patch in close vicinity of the main binding groove.

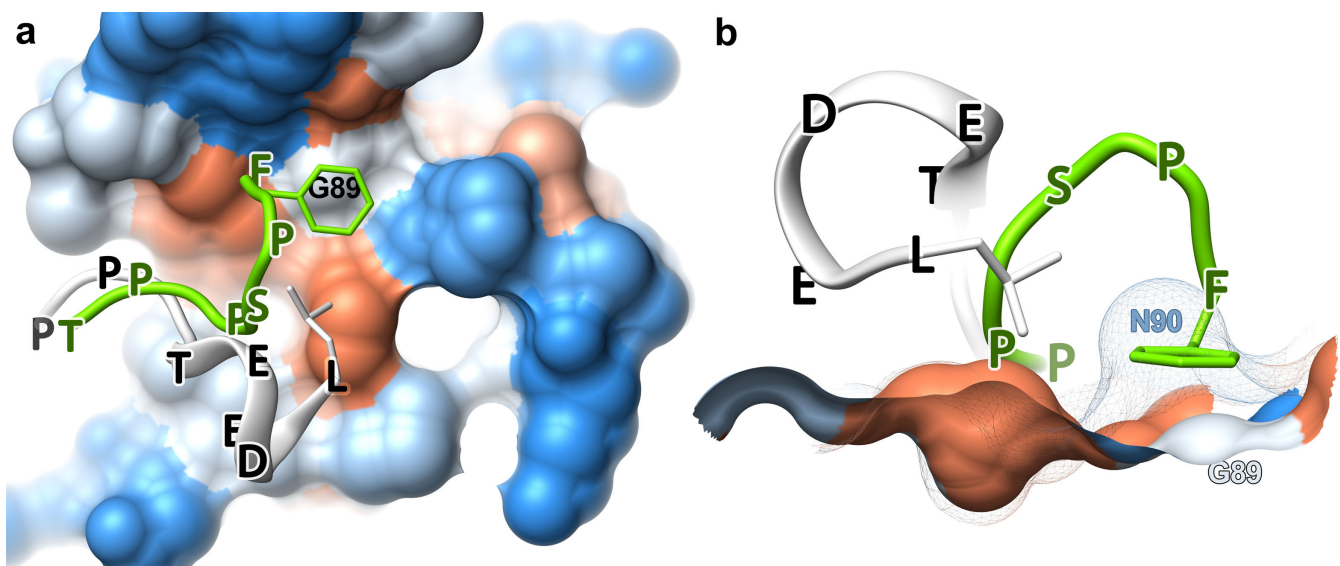


Fig. S5. Class I ENAH EVH1 and class II Homer EVH1 use of the apolar patch to bind their ligands

(a) Solvent-accessible surface of Homer EVH1 bound to TPPSPF (green, PDB code 1DDV) in superposition with ENAH EVH1 bound to Ac-[2-Cl-Phe]PPPTEDEL-NH₂ (white, PDB code 5NC2). TPPSPF binds Homer1 EVH1 C-terminally shifted and interacts with G89. (b) The same superposition and coloring but the solvent accessible surface of ENAH EVH1 added as mesh. The Gly to Asn mutation sterically blocks the hydrophobic patch for ligands with a binding modes like TPPSPF.

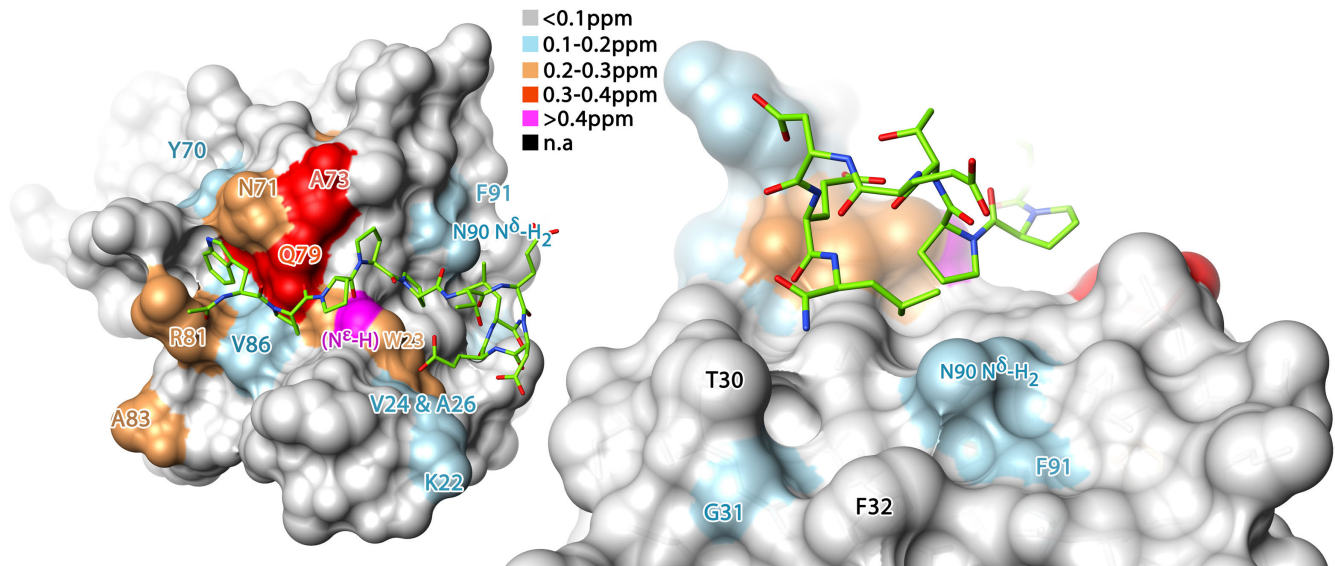


Fig. S6. ^1H - ^{15}N HSQC titration of ENAH EVH1 and Ac-WPPPPTEDEL-NH₂

Maximal euclidean distance of peak perturbations reached with a final 10-fold molar ligand excess. Perturbations further than 0.1 ppm mapped on the solvent accessible surface of ENAH EVH1 (PDB code 5NC7). Due to the flexibility of the loop, T30 and F32 could not be assigned.

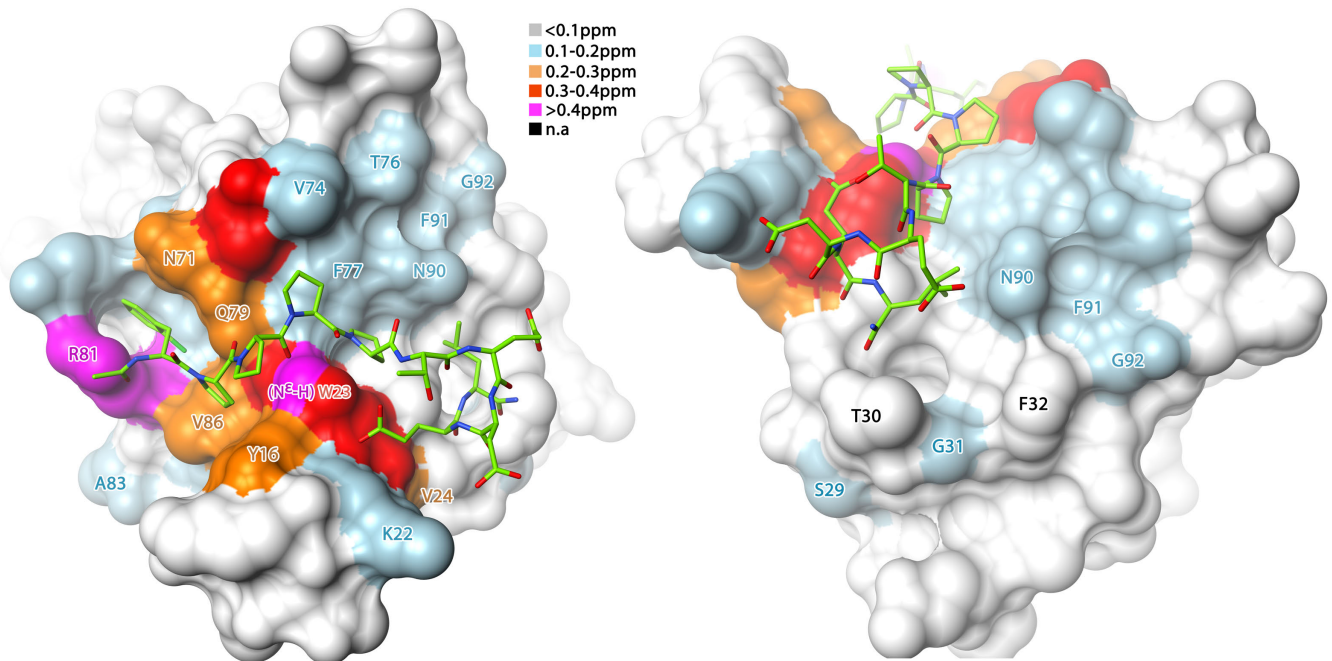


Fig. S7. ^1H - ^{15}N HSQC titration of ENAH EVH1 and Ac-[2-Cl-Phe]PPPTEDEL-NH₂

Maximal euclidean distance of peak perturbations reached with a final 4-fold molar excess. Perturbations further than 0.1 ppm mapped on the solvent accessible surface of ENAH EVH1 (PDB code 5NC2). Due to the flexibility of the loop, T30 and F32 could not be assigned.

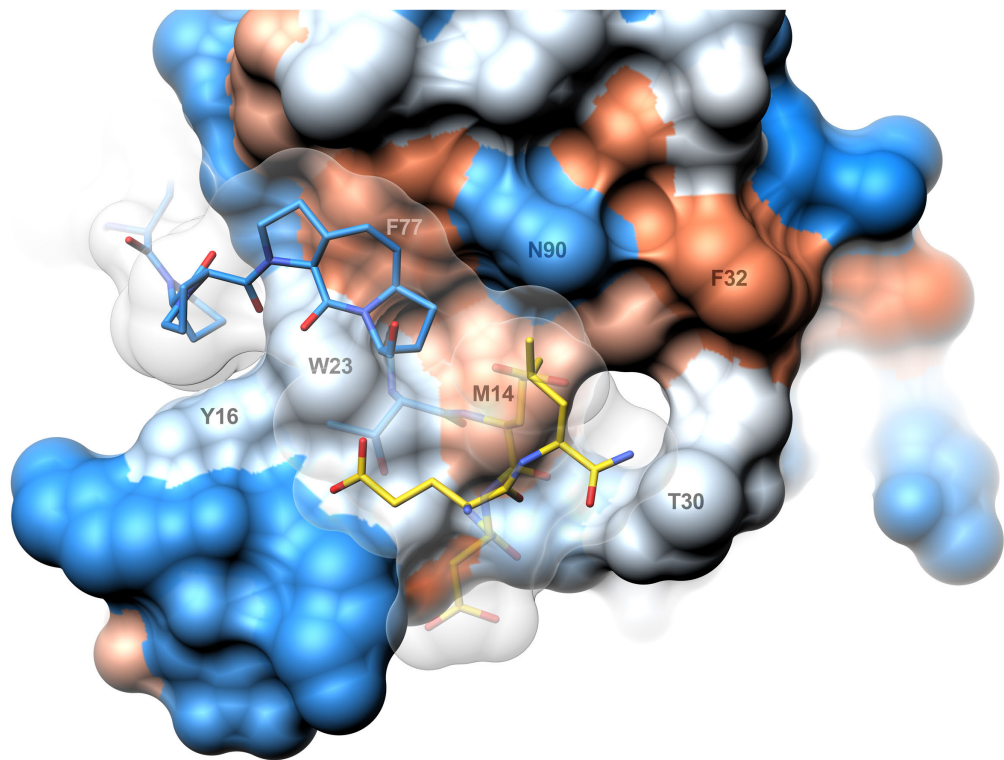


Fig. S8. TEDEL-elongated ligands entirely shield the apolar patch from solvent

ProM-1 and ¹⁰Leu cover an apolar patch that extends from the rigidly shaped binding groove (Y16, W23, F77, M14). Drawn are the solvent accessible surfaces of the chimeric inhibitor **2ΔN** (white) and ENAH EVH1 (blue-white-red for hydrophilic-hydrophobic, PDB code 6RD2). For better visibility amino acids ⁶TED are transparent.

Electron densities of the bound water contacted by ProM-12 and ProM-15-based inhibitors. The two scaffold modifications ProM-12 and ProM-15 aimed to establish contact to a conserved water molecule bound to Trp23 backbone (red sphere drawn with its electron density in SI Appendix Fig. S9). While inhibitors with ProM-12 (upper panel SI Appendix Fig. S9) showed relatively strong and clear difference signal for this water, ProM-15 seemed to compete the bound water off and occupancy dropped notably, which is visible in composite maps at 1σ (lower panel).

Inhibitor composition	Occupancy	B-factor	Fig. S9	PBD code
3b Ac-[2-Cl-Phe][ProM-2][ProM-12]-OH	100%	37 Å ²	(a)	5NCP
4b Ac-[2-Cl-Phe][ProM-2][ProM-15]-OH	95%	31 Å ²	(c)	6RCF
3a Ac-[2-Cl-Phe][ProM-2][ProM-12]-OMe	73%	24 Å ²	(b)	5NDU
4a Ac-[2-Cl-Phe][ProM-2][ProM-15]-OMe	62%	27 Å ²	(d)	6RCJ

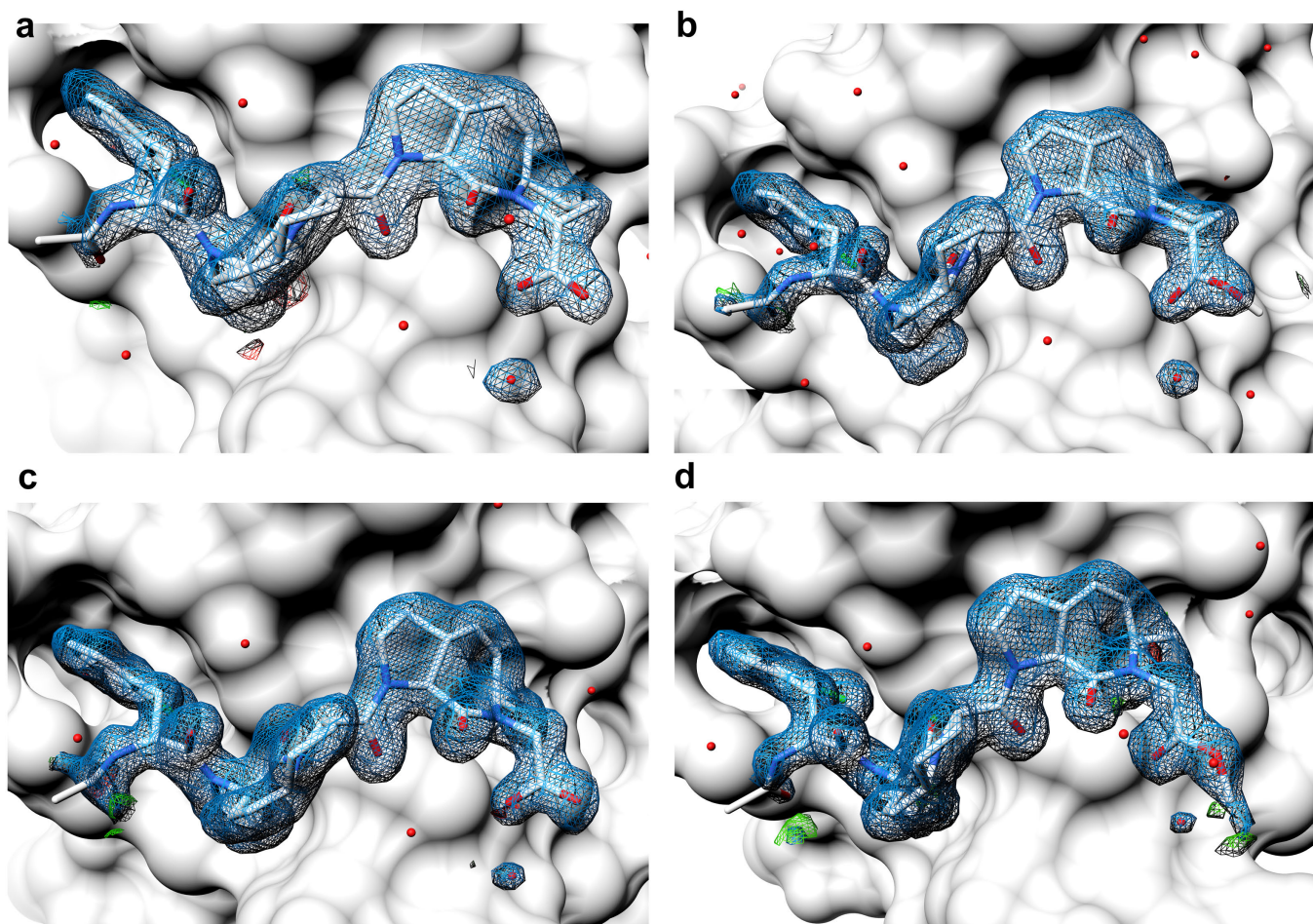


Fig. S9. Electron densities of inhibitor compositions **3** and **4** designed to contact the bound water molecule. 2mFO-DFc composite (1σ , blue) and mFO-DFc difference (3σ , red/green) maps are calculated at (a) **3b** 1.56 Å, (b) **3a** 1.42 Å, (c) **4b** 1.10 Å, (d) **4a** 1.35 Å. Even though the resolution ranges are comparable, complex structures with inhibitor **4** reveal a significantly weaker signal for the water. The occupancy was lowered to roughly 60% to account for a partially bound water at this position. Chemical structures of the mentioned ProM scaffolds are printed in SI Appendix Fig. S2.

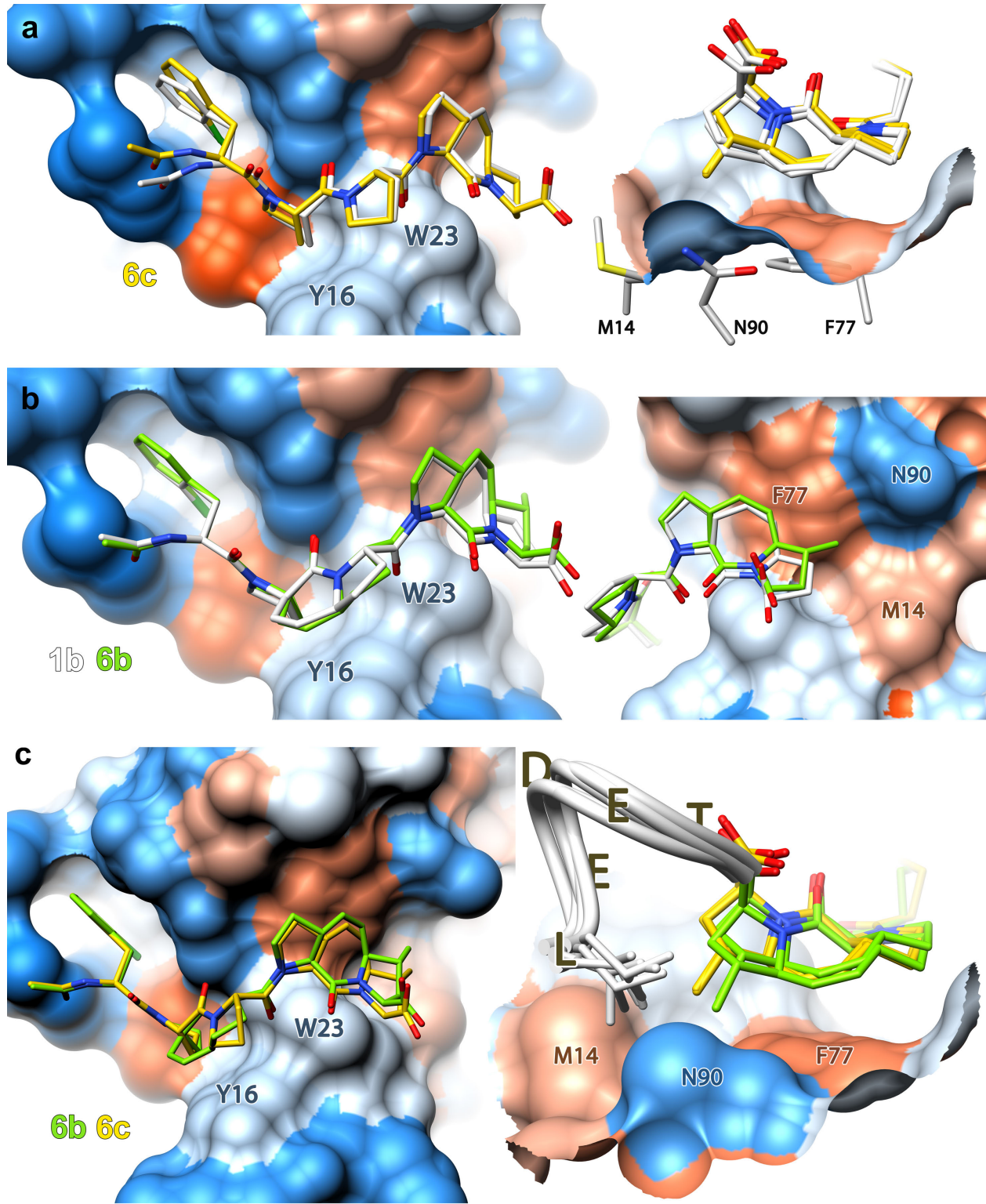


Fig. S10. Two ProM-9-based inhibitor compositions co-crystallized with ENAH EVH1

Compared to ProM-1, the methyl-substituted ProM-9 marginally influenced the positioning of the inhibitor, but allowed to cover more of the hydrophobic patch established by Phe77 and Met14 of ENAH EVH1. (a) Superposition of Ac-[2-Cl-Phe]PP[ProM-9]-OH (yellow, **6c**) with the according reference composition Ac-[2-Cl-Phe]PP[ProM-1]-OH (white). (b) Superposition of Ac-[2-Cl-Phe][ProM-2][ProM-9]-OH (green, **6b**) and Ac-[2-Cl-Phe]-[ProM-2]-[ProM-1]-OH (white, **1b**). (c) Superposition of Ac-[2-Cl-Phe]PP[ProM-9]-OH (yellow, **6c**) and Ac-[2-Cl-Phe][ProM-2][ProM-9]-OH (green, **6b**) (left) and both in superposition with TEDEL-containing ligands drawn as white ribbons (different structures) confirmed that ProM-9 pointed towards the apolar patch contacted by the terminal Leu (right).

The hot-spot within the main binding groove of Ena/VASP EVH1. ProM-1 can not be shuffled within $^1\text{FPPPPP}$ to replace any Pro-Pro tandem, and binding strength increases by -3 kJ/mol only if ProM-1 replaces ^4PP . This boost is independent of the overall inhibitor composition; in the presence of N- and C-terminal flanking residues the boost is -3.3 (0.6), while the core motif pentamer gains -3.4 (0.4) kJ/mol of ΔG on ENAH EVH1 (SI Appendix Tab. 7). Similar boosts are measured on VASP EVH1 (SI Appendix Tab. 8) when ProM-1 is incorporated into the ActA 13-mer, -3.0 (0.3) kJ/mol , or the 2-Cl-Phe-equipped core recognition motif, -3.6 (0.4) kJ/mol .

As ITC data suggest, the gain of affinity is solely enthalpy driven (6). Hence, we assume that the measured affinity boost is based on the interaction of the scaffold's vinylidene bridge with the underlying Phe77. Indeed, the crystal structures of ProM-1-containing complexes (PDB codes 4MY6, 5N9C, 5N9P or 5NAJ) confirmed that ProM-1 efficiently shielded Phe77 from the solvent (SI Appendix Fig. S11). Superposition of ^4PP - and $^4\text{ProM-1}$ -containing inhibitors (such as in the right panel of SI Appendix Fig. S11) highlight that the scaffold ProM-1 fit over the hydrophobic patch without affecting the backbone trace of the inhibitor.

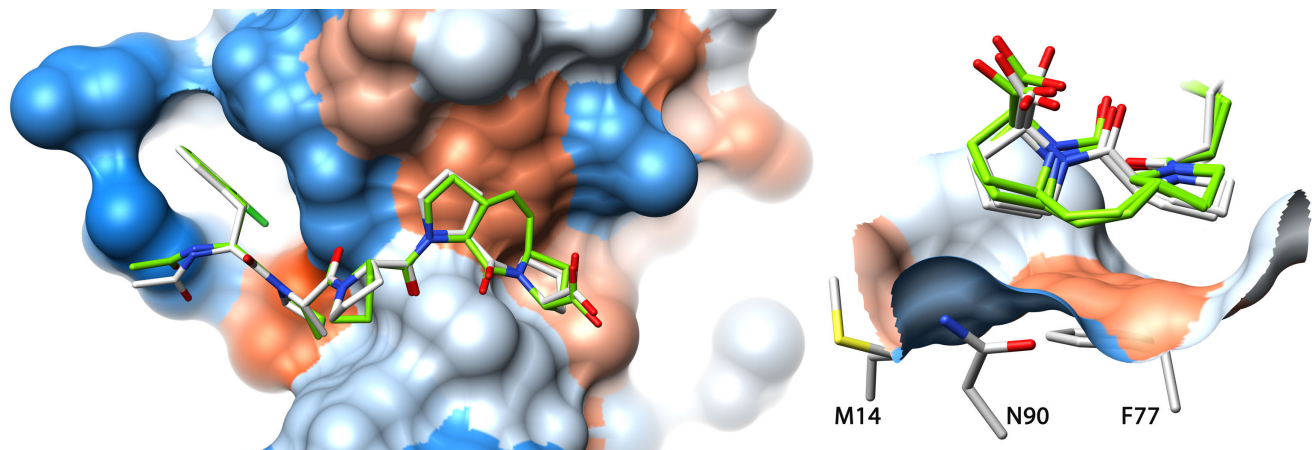


Fig. S11. Superposition of Ac-[2-Cl-Phe]PPPP-OH and Ac-[2-Cl-Phe]PP[ProM-1]-OH in complex with ENAH EVH1

Left panel: Replacement of the second pair of prolines by ProM-1 (green, PDB code 5N9C) did not affect the backbone trace relative to ^4PP (white, PDB code 5N91). Right panel: The vinylidene bridge snugly fit over Phe77 and shielded the hydrophobic patch from the solvent. Both complex structures contain two chains in the asymmetric unit, all are shown in the right panel. Chemical structure of ProM-1 is printed in SI Appendix Fig. S2.

Optimization of ⁴Pro by two scaffolds. The results of the spot array analysis showed that the third proline was exchangeable by aliphatic residues. ProM-1-based Xaa-Pro mimetica are interesting for other proline-rich segment recognizing domains apart from Ena/VASP EVH1, and could serve as templates for WW domains that recognize PLPPLP motifs. Like other Xaa-*trans*-Pro mimetica (31, 32), ProM-1 derivatives lack a freely rotating Xaa side chain as the vinylidene bridge fixates the C_β in one conformation. Xaa-*trans*-Pro scaffolds however display an important alteration compared to Pro-Pro mimicking scaffolds, namely the unsubstituted, protonated backbone amide of the Xaa amino acid (ProM-3, top panel SI *Appendix* Fig. S12), which alters the chemical property of the scaffold compared to a Pro-Pro mimetica. In case of ProM-3, the protonated backbone amide lead to a unique crystal packing in which the scaffold itself was involved in a crystal contact. Several attempts to force ENAH EVH1 in complex with Ac-[2-Cl-Phe][ProM-2][ProM-3]-OH to grow in a different packing failed. Independent of the crystal space group used as seeds, the crystal packing could not be altered, suggesting that ProM-3 introduced dominant polar interactions on the solvent-exposed side of the bound inhibitor. Due to the increased interactions with the solvent, compositions with ProM-3 were therefore expected to loose affinity compared to ProM-1-containing inhibitors. Indeed, ⁴ProM-3-containing inhibitors bound to ENAH- and VASP EVH1 with the same affinity as ⁴PP, while parent compositions with ⁴ProM-1 bound 4-5 times stronger (SI *Appendix* Tabs. 7 and 8). The presence of possible intrachain hydrogen bonds by ProM-3 presumably weakened the stabilization by water (33) and increased the solvation of the inhibitor, which in turn tended to interact less strongly with other solutes (34). The hydration by more water molecules did not provide favorable conditions for PPII conformation (35) and the increased mobility of the scaffold finally raised the entropic penalty upon binding (34). The resulting weakened affinity confirms the hypothesis that backbone solvation is the major determinant of proline-rich segments to adopt pre-structured, extended helical conformations (35, 36).

The hypothesis was supported by the crystal structure and affinity measurements of compositions containing ProM-4 (lower panel of SI *Appendix* Fig. S12). The cyclization of ProM-4 with a piperidine moiety conserved the amide N substitution within the inhibitor but caused a less rigid scaffold as compared to ProM-1. The piperidine moiety as N-terminal building block led to a different exit vector of ProM-4 and caused a slight rearrangement within the binding groove of ENAH EVH1 relative to the parent inhibitor. However, the ProM-4 composition bound not significantly worse compared to the ProM-1-containing reference inhibitor, neither to ENAH EVH1 nor VASP EVH1 (SI *Appendix* Tabs. S7 and S8). The notion that even bulkier substitutions for prolines are valid as long as the backbone amide remains substituted is in agreement with reported inhibitors for SH3 domains, where replacement of single prolines by amide N-substituted peptoids yields in high-affinity inhibitors (37–39). As we aimed to maximize the ligand efficiency, ProM-4-containing inhibitors were not investigated further.

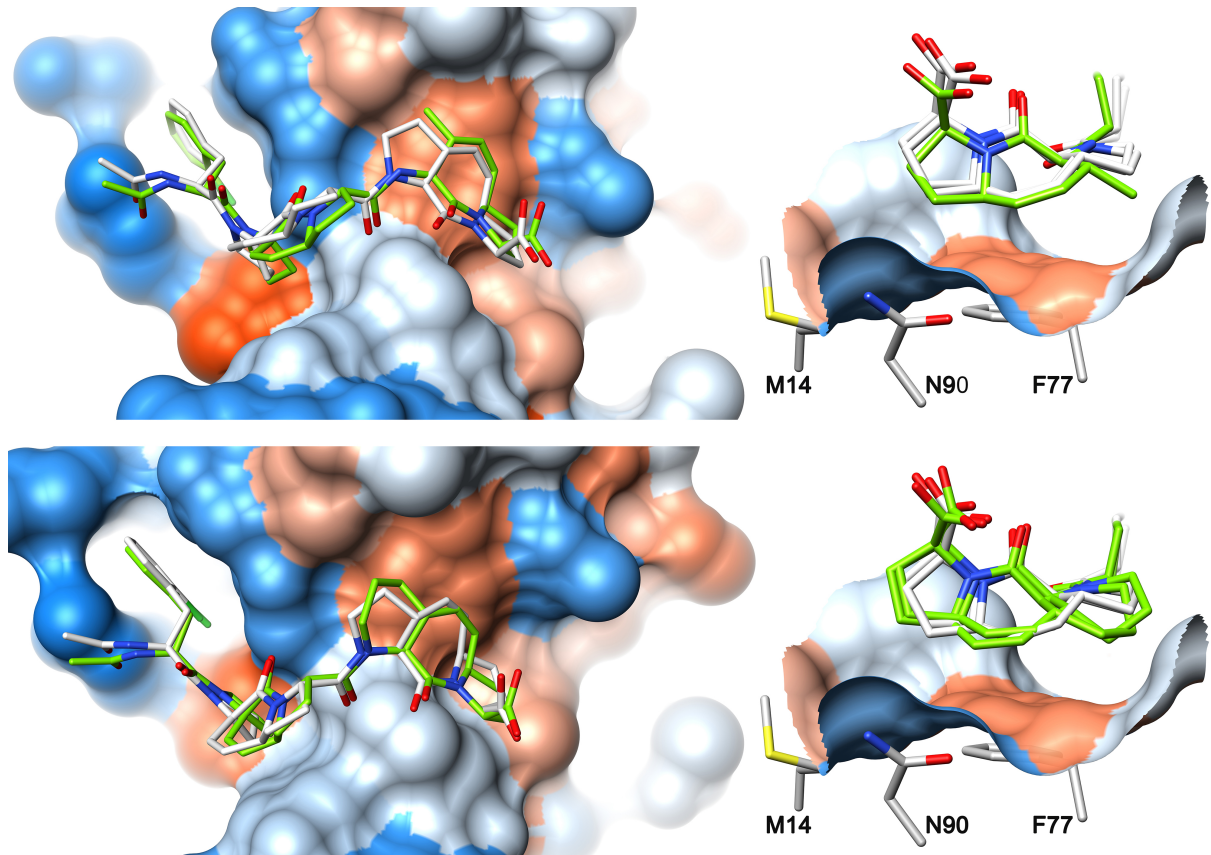


Fig. S12. Superposition of crystal structures of ENAH EVH1 in complex with inhibitors Ac-[2-Cl-Phe][ProM-2][ProM-1]-OH (1b**) and the related compositions R-[ProM-3]-OH and R-[ProM-4]-OH**

Top panel: The scaffold ProM-3 was designed as Xaa-*trans*-Pro to mimic aliphatic interactions of ⁴Xaa as seen in the SPOT substitution Fig. S3. Formally removing the C_δ of the N-terminal ring of ProM-1 (**1b**, white) yielded in ProM-3 (green), which bound canonically within the main binding groove without any major rearrangement compared to inhibitor **1b**.

Lower panel: The scaffold ProM-4 was designed to conserve the amide N-substitutions of Pro-*trans*-Pro while inducing some flexibility within the inhibitor by enlarging the N-terminal ring of ProM-1 (white). The piperidine moiety of ProM-4 (green) yields to a different exit vector that causes visible rearrangement of the whole scaffold on the C-terminal side. Solvent accessible surfaces of ENAH EVH1 are color coded by hydrophobicity (blue-white-red for hydrophilic-hydrophobic). Complex structure with Ac-[2-Cl-Phe][ProM-2][ProM-3]-OH contains one chain (PDB code 5NBF), inhibitor **1b** (PDB code 4MY6) and Ac-[2-Cl-Phe][ProM-2][ProM-4]-OH (PDB code 5NCF) each contain two chains in the asymmetric unit, all are shown. Chemical structures of the mentioned ProM scaffolds are printed in SI Appendix Fig. S2.

Inhibitor selectivity. The procedure is described in the methods part on page 3. Here, 10 or 11 HMQC SOFAST spectra with 200 μ M protein and different inhibitor excess were recorded. Each spectrum overlay was plotted with the `nmrglue` module in python, drawn with the same contour level start value. The sparky peak lists were processed and perturbations fitted by a script written in R language. The same selection criteria were used for all 9 HMQC experiments (peak perturbation >0.1 ppm and K_d with coefficient significance of $P<0.001$). Affinities meeting the criteria were plotted in a bar chart with continuous color gradient (`colorRampPalette`) and the same color palette used to create a command text string readable by Chimera to color the amino acids and sidechain atoms (marked as Trp NE, Asn ND or Gln NE in the following figures). Amino acid numbering was subsequently added in Photoshop (Adobe) and placed roughly at the position of the resonance.

For Yap1 WW1, the assignment was kindly gifted by Dr. Maria Macias. The sequence of the deposited NMR structure (PDB code 2LAY) was changed to align with the amino acid sequence of the peak table (renumbering D170 to D5). As the secondary structure of Yap1 WW1 seems to stabilize upon binding the ligand, some of the assigned peaks were not visible at low inhibitor excess. Roughly 5 of the assigned peaks had to be discarded for that reason.

For Fyn SH3, none of the deposited spectra in the Biological Magnetic Resonance Data Bank (BMRB) fit on the recorded spectrum of our construct. Clearly identifiable peaks had to be assigned manually using the spectrum shown by Mal *et al.* (40). For plotting the affinities, the solution NMR structure of Morton *et al.* (PDB code 1NYF) was chosen as the amino acid sequence numbering used by Mal matched with this structure. As our Fyn SH3 spectrum was almost identical to the one shown by Mal *et al.*, 44 out of the 58 amino acids in the 1NYF structure could be tracked.

For Profilin, the assigned spectrum extracted from BRMB ID 4082 coincided almost perfectly with our spectrum. Of the 154 assigned peaks, 13 were not tracked due to ambiguity of their initial position. For plotting the affinities, however, the refined solution NMR structure of BRMB ID 4082 (PDB code 1PFL) was not used. Instead, the affinities were plotted onto a ternary complex of Profilin-Actin with the poly-proline sequence of VASP (PDB code 2PAV), which has the identical amino acid sequence as 1PFL.

	Inhibitor 1		Inhibitor 4a		Inhibitor 7	
	K_d [μ M]	Decrease	K_d [μ M]	Decrease	K_d [μ M]	Decrease
ENAH EVH1	4.1	(ref.)	0.47	(ref.)	0.12	(ref.)
Fyn SH3	5400	1300 \times	2400	5200 \times	1900	16000 \times
Profilin	780	190 \times	630	1300 \times	210	1800 \times
Yap1 WW1	1000	250 \times	460	980 \times	1100	9600 \times

Tab. S10. Mean affinities of fitted peak perturbations and relative affinity losses compared to ENAH EVH1

Mean affinities were calculated by transforming all fitted K_d of the HSQC experiments first to the free Gibbs energy (ΔG), which is assumed to be much closer normal distributed than the K_d . The arithmetic mean of ΔG values was then calculated back into the K_d written in the table. Additionally, the table lists the fold decrease of binding strength of each inhibitor composition relative to ENAH EVH1 (reference, ref.), highlighting that the affinity-improved inhibitors bound worse to off-target proteins Fyn SH3, Profilin, and Yap1 WW1 compared to the initial inhibitor 1.

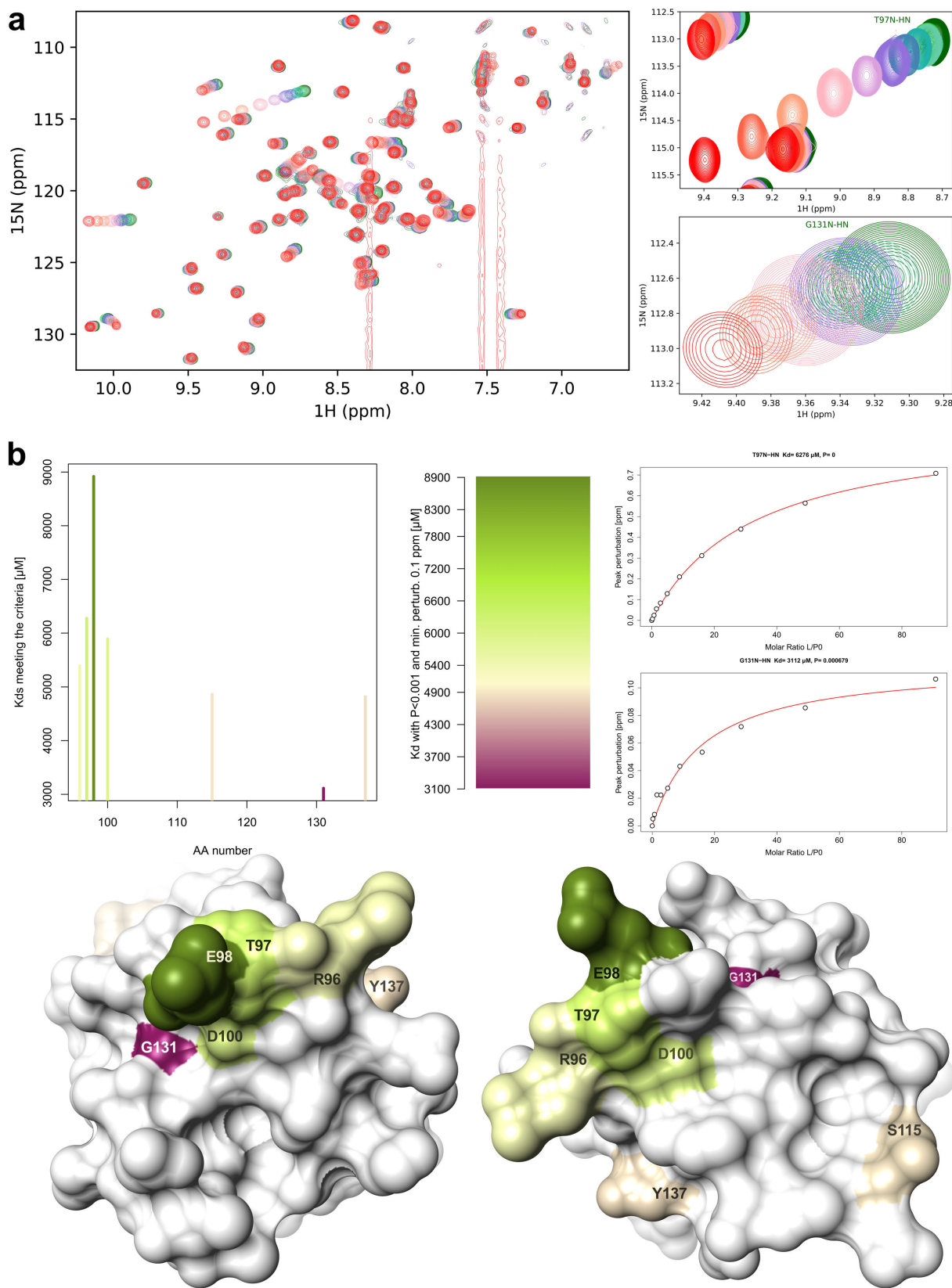


Fig. S13. ^1H - ^{15}N HSQC titration of Fyn SH3 and Ac-[2-Cl-Phe][ProM-2][ProM-1]-OEt

(a) Spectra overlay and detailed perturbation of T97N-HN and G131N-HN caused by titration of inhibitor 1. (b) Upper panel: Affinities of accepted fits of peak perturbations along the amino acid (AA) sequence. Plotted on the right panel are the two fitted peak perturbations shown in detail above. Lower panel: Color coding of the bar plot drawn on the solvent accessible surface of Fyn SH3. The binding grooves of Fyn SH3 are formed by Y91, Y137, W119, Y93, and D100 (41).

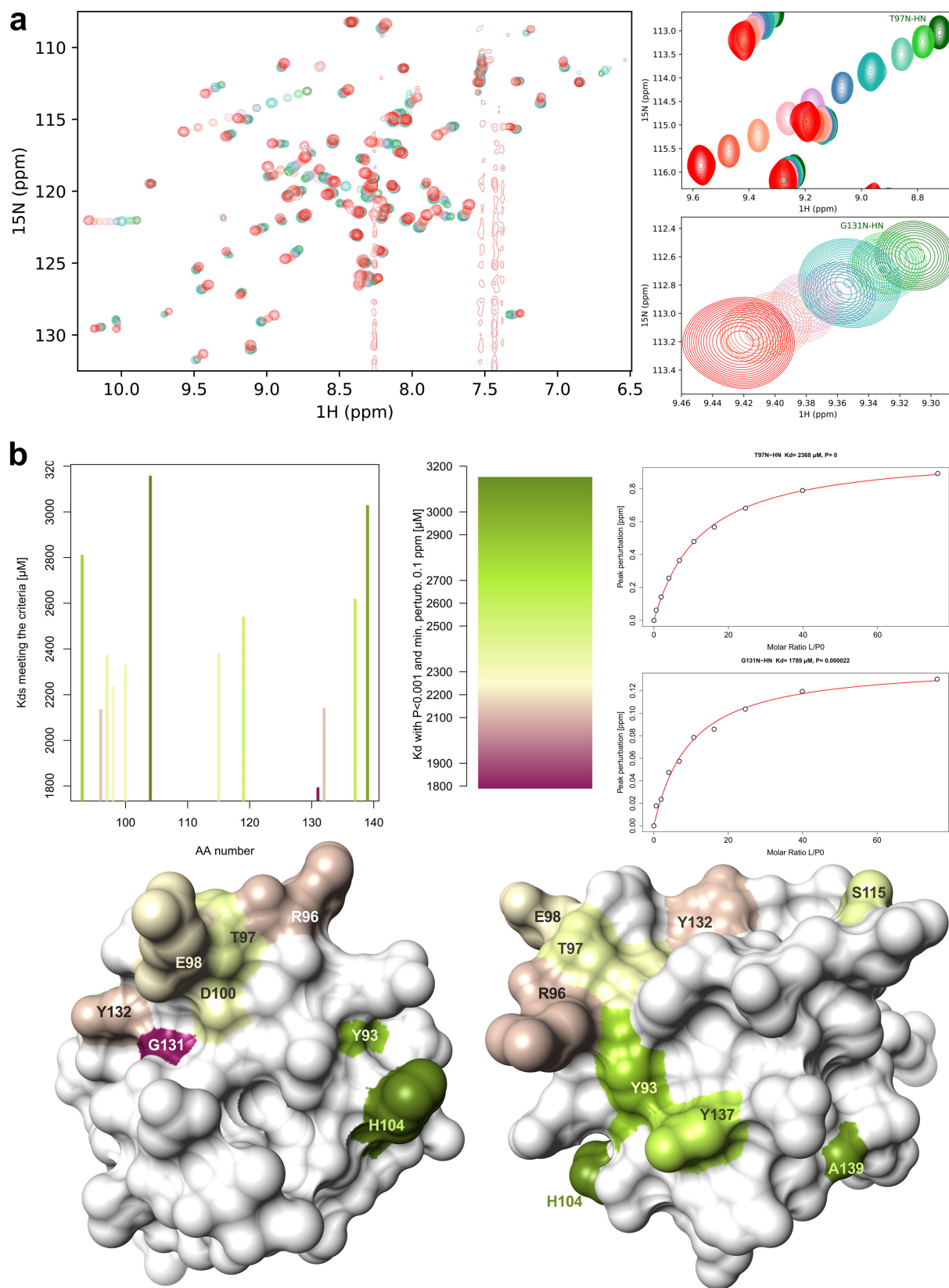


Fig. S14. ^1H - ^{15}N HSQC titration of Fyn SH3 and Ac-[2-Cl-Phe][ProM-2][ProM-15]-OMe

(a) Spectra overlay and detailed perturbation of T97N-HN and G131N-HN caused by titration of inhibitor **4a**. (b) Upper panel: Affinities of accepted fits of peak perturbations along the amino acid (AA) sequence. Plotted on the right panel are the two fitted peak perturbations shown in detail above. Lower panel: Color coding of the bar plot drawn on the solvent accessible surface of Fyn SH3. The binding grooves of Fyn SH3 are formed by Y91, Y137, W119, Y91, Y93, and D100 (41).

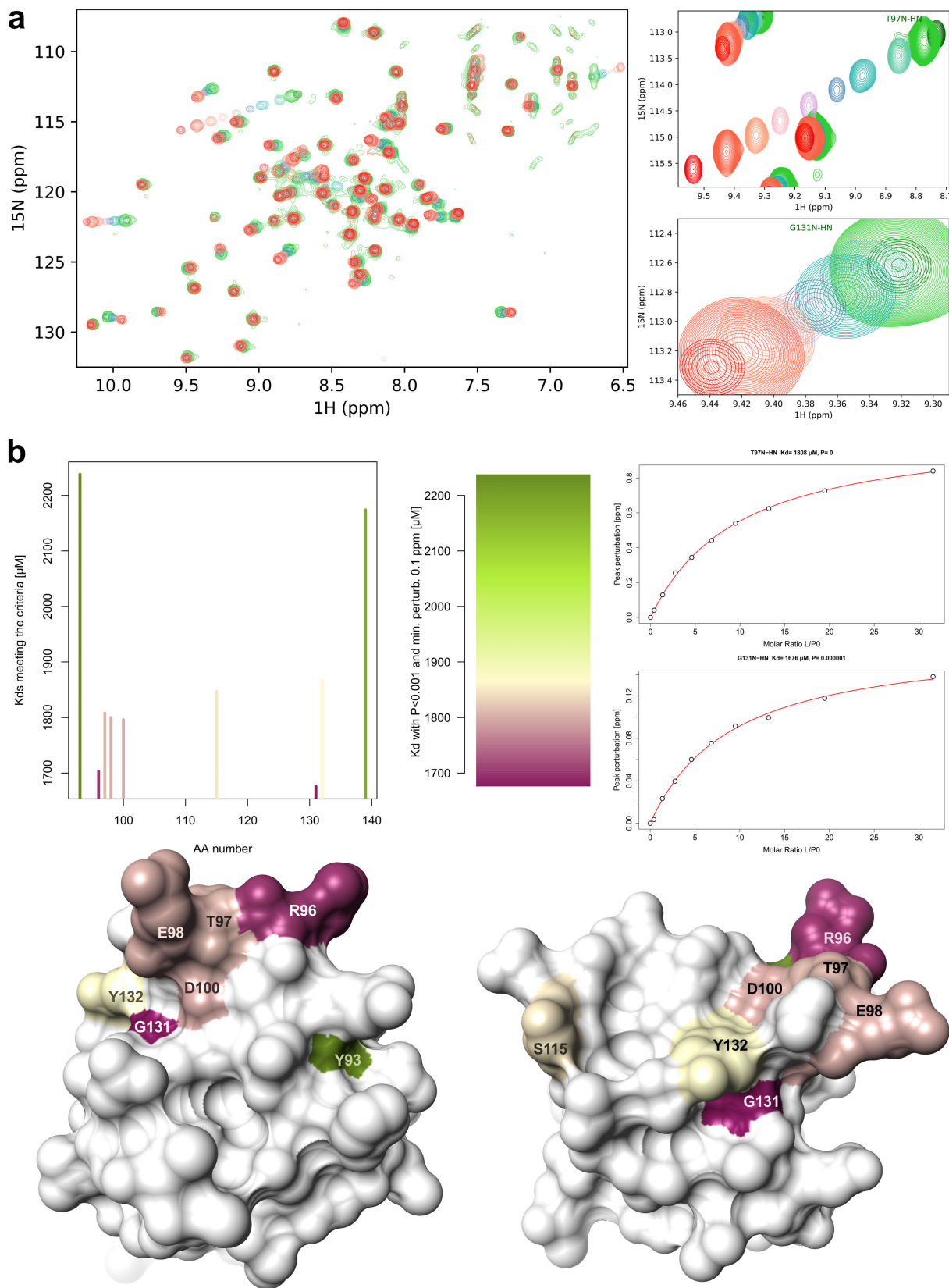


Fig. S15. ^1H - ^{15}N HSQC titration of Fyn SH3 and Ac-[2-Cl-Phe][ProM-2][ProM-13]-OEt (6)

(a) Spectra overlay and detailed perturbation of T97N-HN and G131N-HN caused by titration of inhibitor 6. (b) Upper panel: Affinities of accepted fits of peak perturbations along the amino acid (AA) sequence. Plotted on the right panel are the two fitted peak perturbations shown in detail above. Lower panel: Color coding of the bar plot drawn on the solvent accessible surface of Fyn SH3. The binding grooves of Fyn SH3 are formed by Y91, Y137, W119, Y93, and D100 (41).

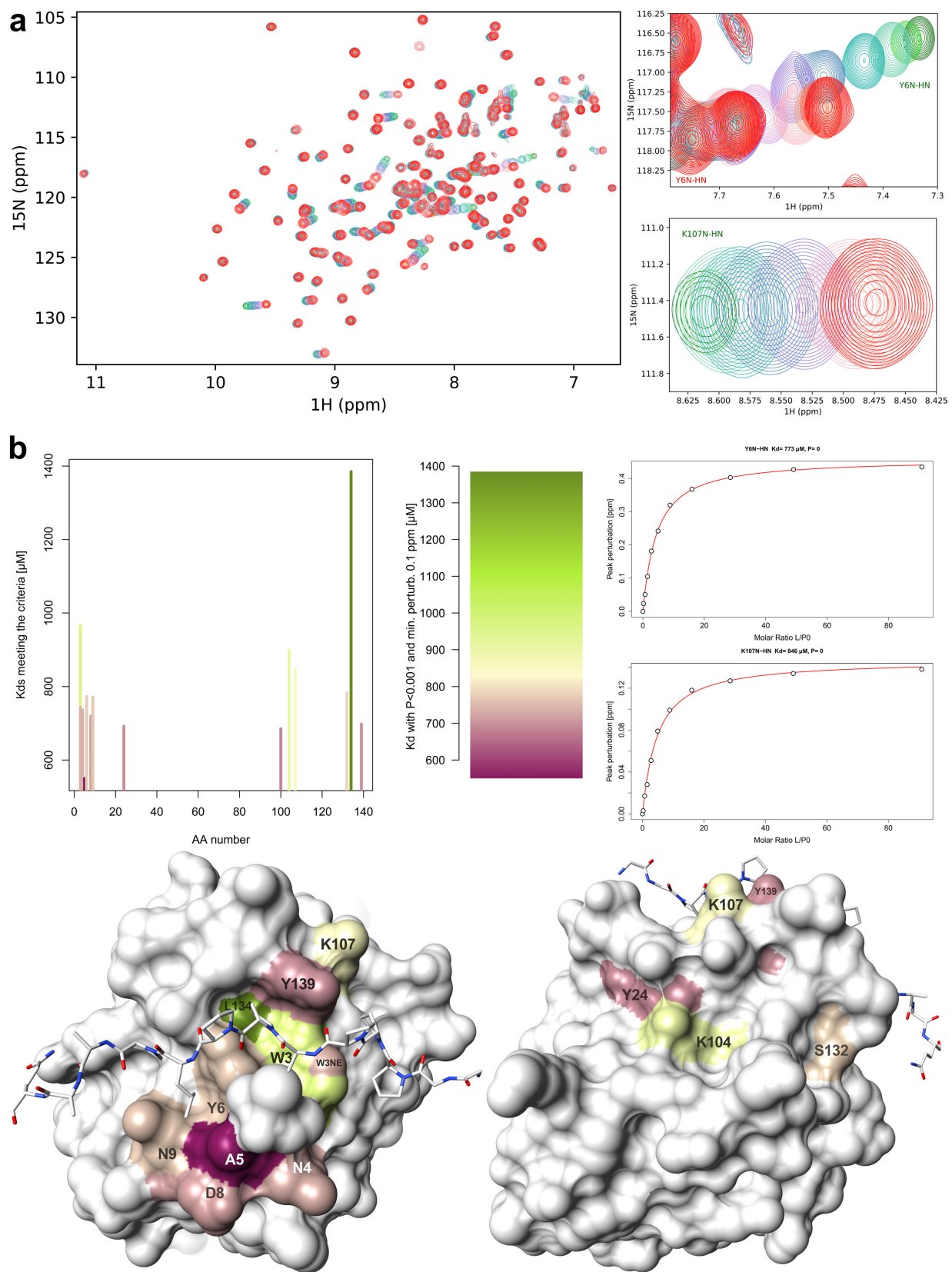


Fig. S16. ^1H - ^{15}N HSQC titration of Profilin and Ac-[2-Cl-Phe][ProM-2][ProM-1]-OEt

(a) Spectra overlay and detailed perturbation of Y6N-HN and K107N-HN caused by titration of inhibitor 1. (b) Upper panel: Affinities of accepted fits of peak perturbations along the amino acid (AA) sequence. Plotted on the right panel are the two fitted peak perturbations shown in detail above. Lower panel: Color coding of the bar plot drawn on the solvent accessible surface of Profilin. All perturbations are found close to the binding pocket recognizing the proline-rich motif of VASP.

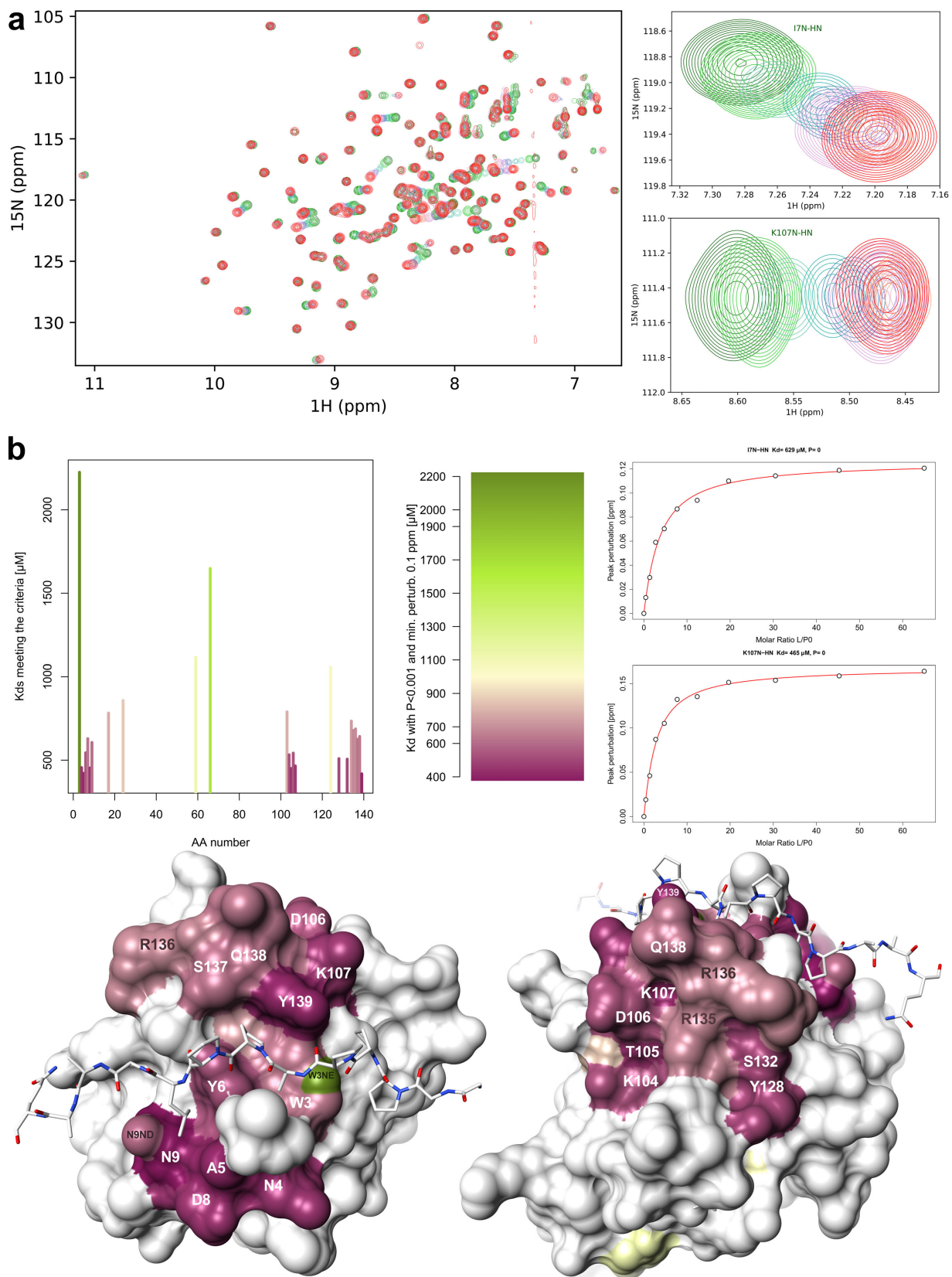


Fig. S17. ^1H - ^{15}N HSQC titration of Profilin and Ac-[2-Cl-Phe][ProM-2][ProM-15]-OMe

(a) Spectra overlay and detailed perturbation of I7N-HN and K107N-HN caused by titration of inhibitor **4a**. (b) Upper panel: Affinities of accepted fits of peak perturbations along the amino acid (AA) sequence. Plotted on the right panel are the two fitted peak perturbations shown in detail above. Lower panel: Color coding of the bar plot drawn on the solvent accessible surface of Profilin. Almost all perturbations are found close to the binding pocket recognizing the proline-rich motif of VASP.

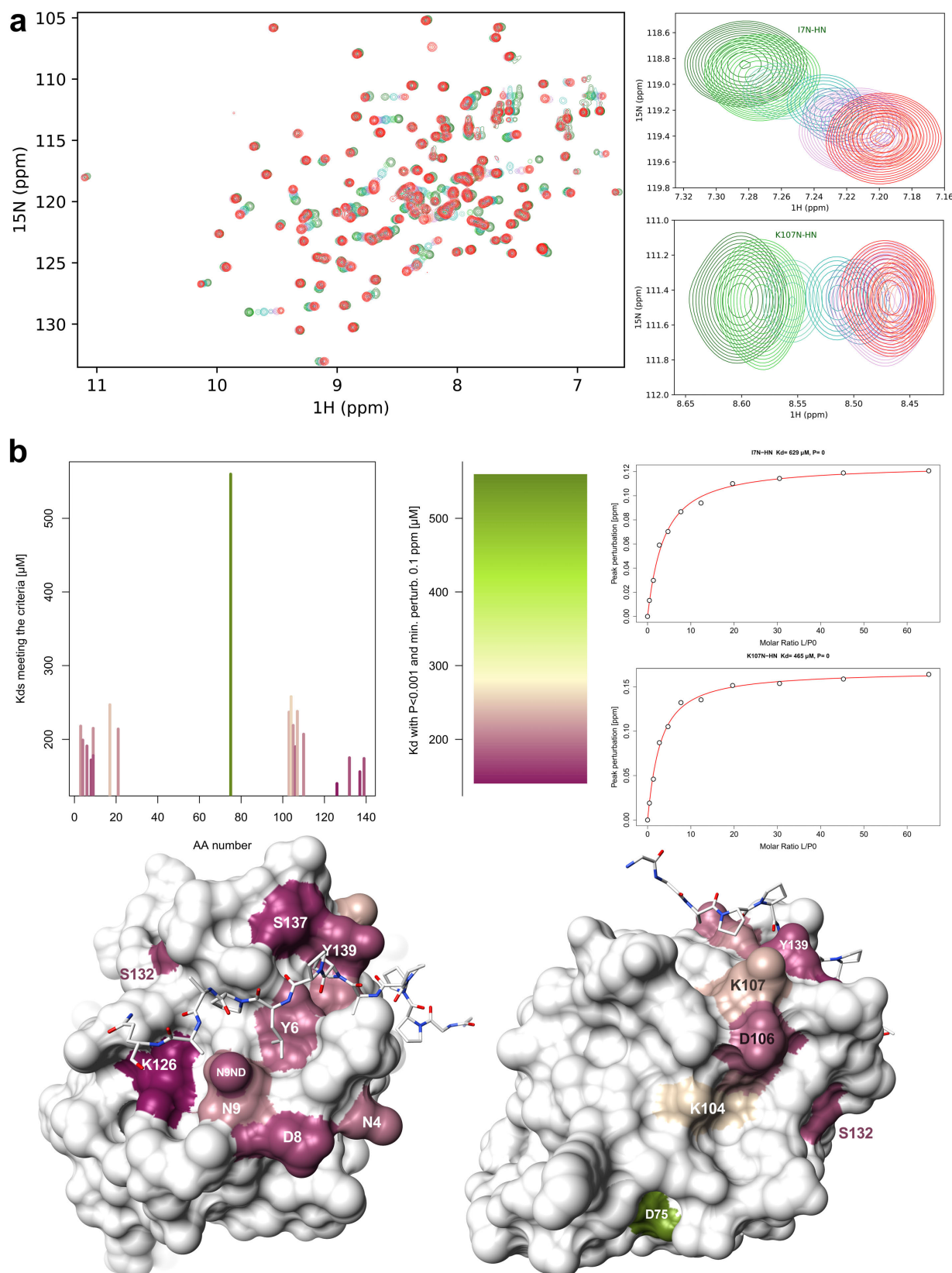


Fig. S18. ^1H - ^{15}N HSQC titration of Profilin and Ac-[2-Cl-Phe][ProM-2][ProM-13]-OEt

(a) Spectra overlay and detailed perturbation of I7N-HN and K107N-HN caused by titration of inhibitor **6**. (b) Upper panel: Affinities of accepted fits of peak perturbations along the amino acid (AA) sequence. Plotted on the right panel are the two fitted peak perturbations shown in detail above. Lower panel: Color coding of the bar plot drawn on the solvent accessible surface of Profilin. All perturbations except a weak interaction by D75 are found close to the binding pocket recognizing the proline-rich motif of VASP.

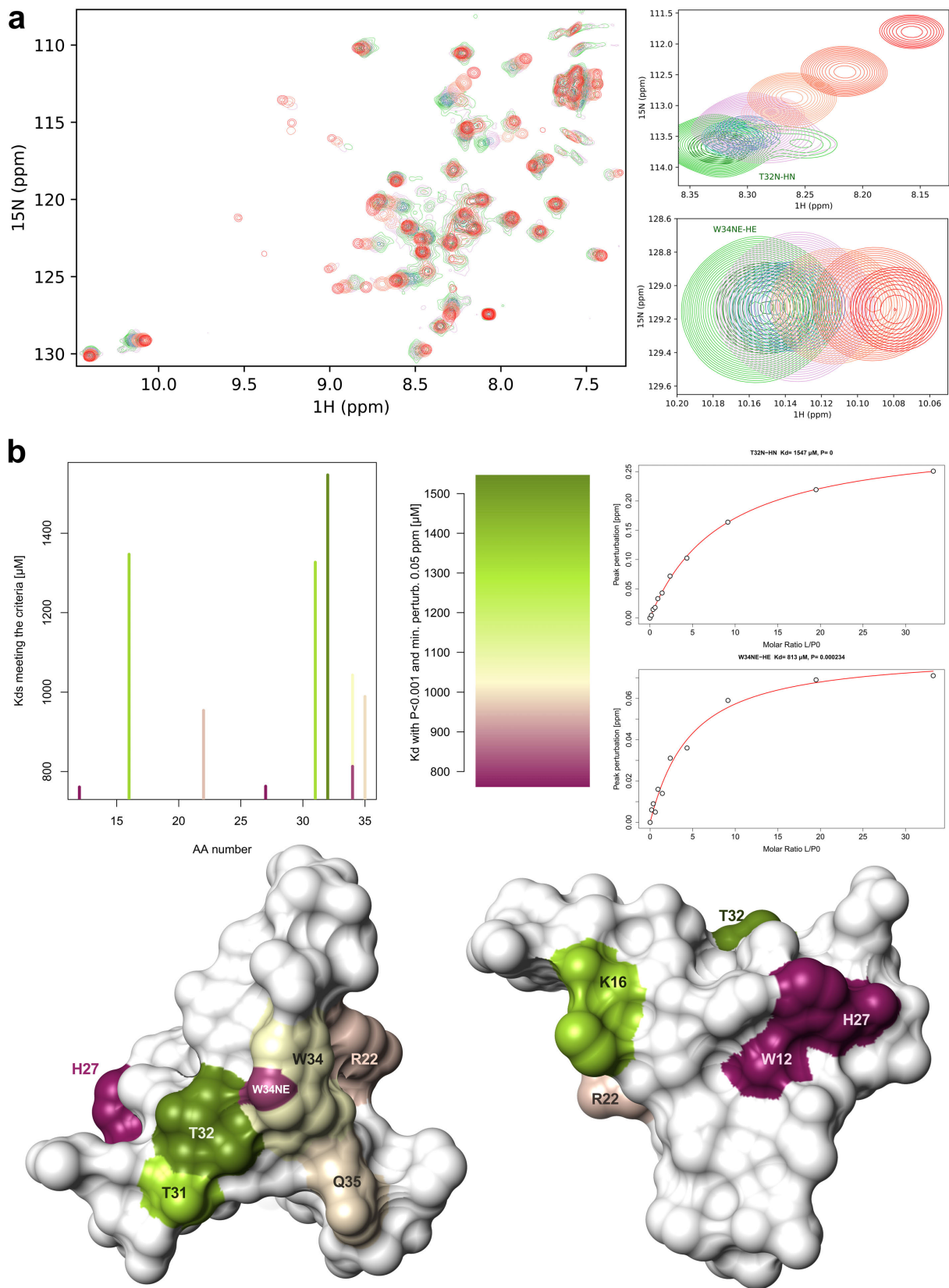


Fig. S19. ^1H - ^{15}N HSQC titration of Yap1 WW1 and Ac-[2-Cl-Phe][ProM-2][ProM-1]-OEt

(a) Spectra overlay and detailed perturbation of T32N-HN and W42NE-HE caused by titration of inhibitor 1. (b) Upper panel: Affinities of accepted fits of peak perturbations along the amino acid (AA) sequence. Plotted on the right panel are the two fitted peak perturbations shown in detail above. Lower panel: Color coding of the bar plot drawn on the solvent accessible surface of Yap1 WW1. The interaction site of Yap1 WW1 is formed by Q30, T32 Y23, W34, and H27 (42).

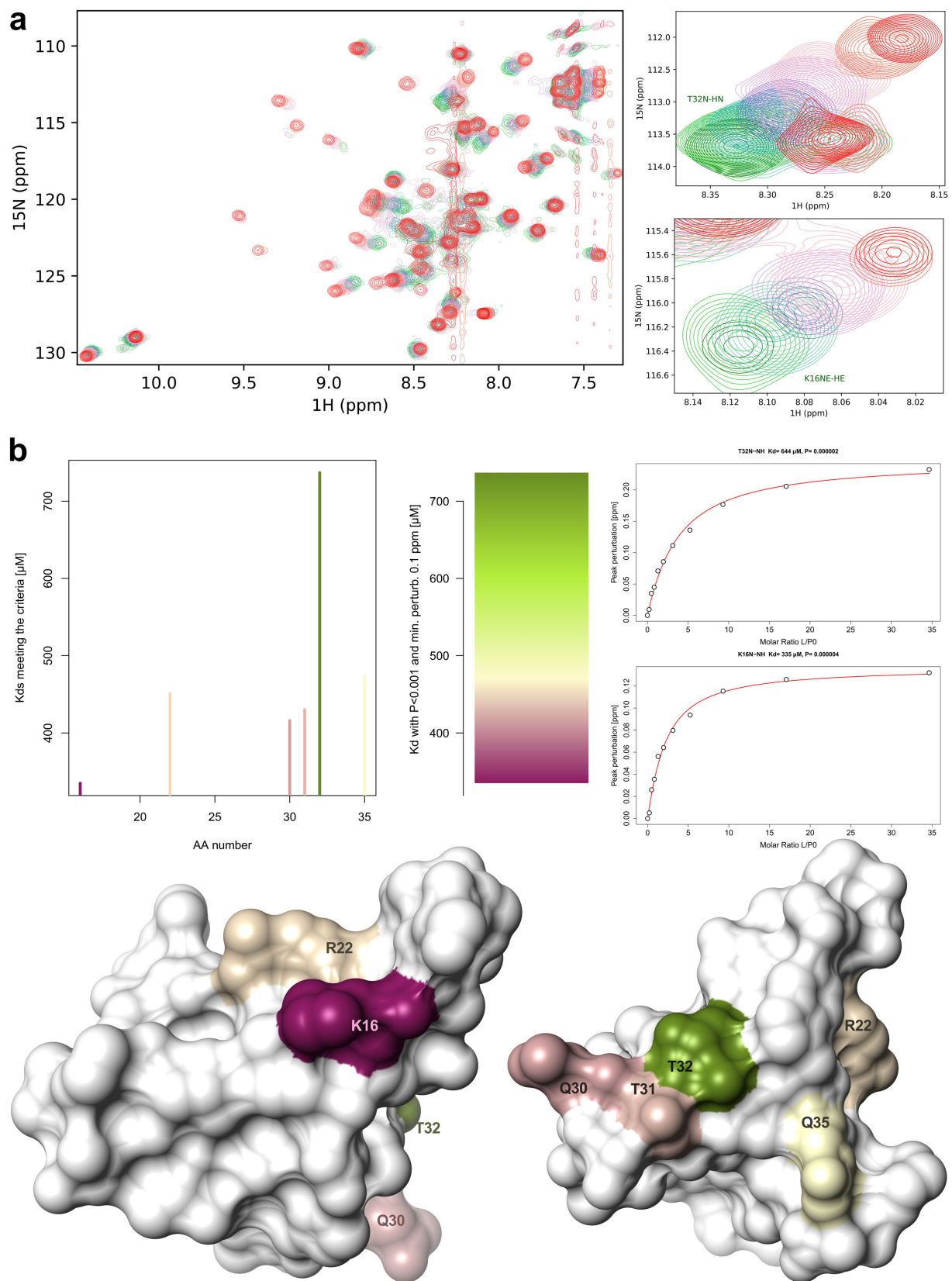


Fig. S20. ¹H-¹⁵N HSQC titration of Yap1 WW1 and Ac-[2-Cl-Phe][ProM-2][ProM-15]-OMe

(a) Spectra overlay and detailed perturbation of T32N-HN and K16N-HN caused by titration of inhibitor **4a**. (b) Upper panel: Affinities of accepted fits of peak perturbations along the amino acid (AA) sequence. Plotted on the right panel are the two fitted peak perturbations shown in detail above. Lower panel: Color coding of the bar plot drawn on the solvent accessible surface of Yap1 WW1. The interaction site of Yap1 WW1 is formed by Q30, T32 Y23, W34, and H27 (42).

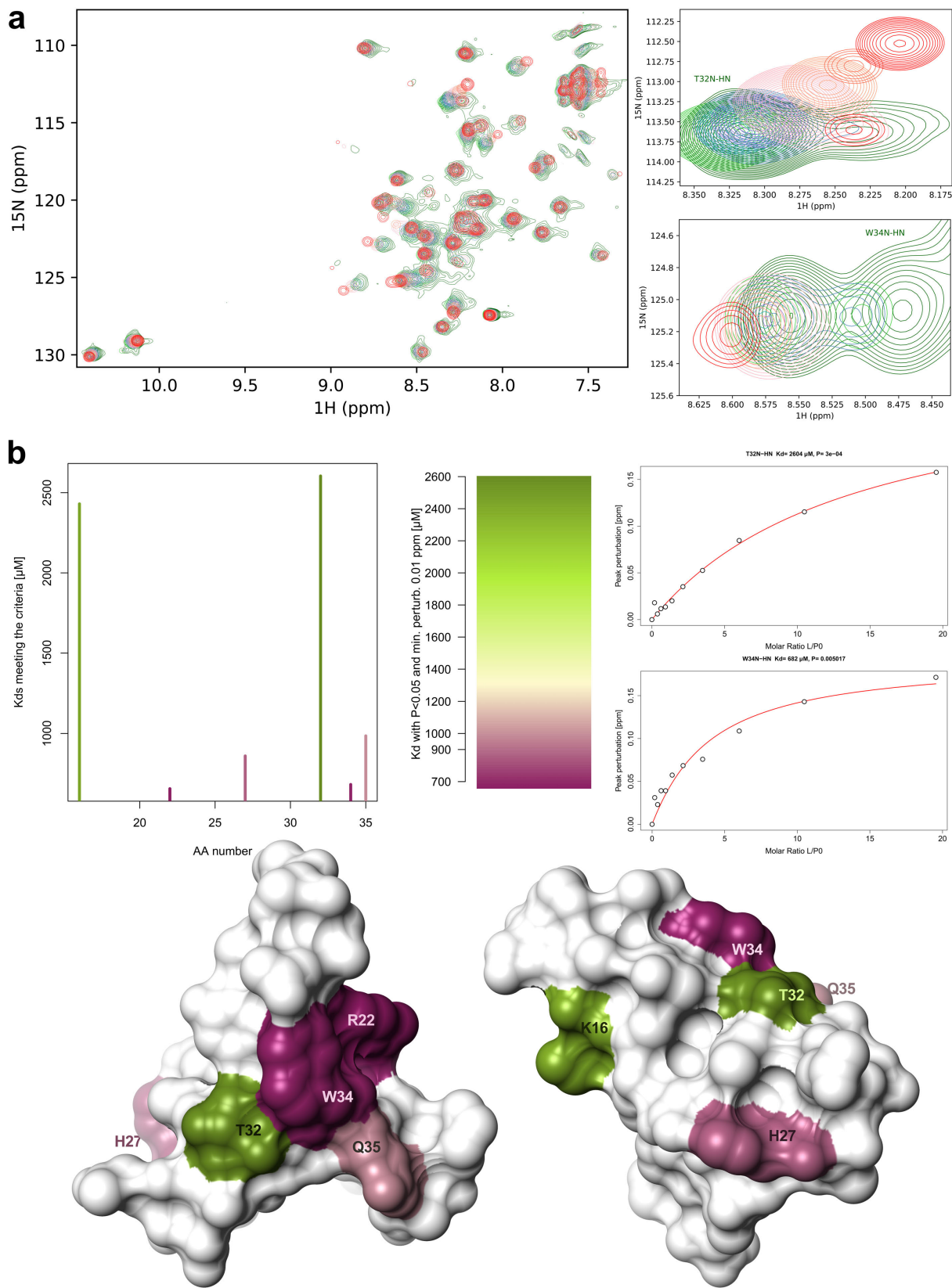


Fig. S21. ^1H - ^{15}N HSQC titration of Yap1 WW1 and Ac-[2-Cl-Phe][ProM-2][ProM-13]-OEt

(a) Spectra overlay and detailed perturbation of T32N-HN and W34N-HN caused by titration of inhibitor **6**. (b) Upper panel: Affinities of accepted fits of peak perturbations along the amino acid (AA) sequence. Plotted on the right panel are the two fitted peak perturbations shown in detail above. Lower panel: Color coding of the bar plot drawn on the solvent accessible surface of Yap1 WW1. The interaction site of Yap1 WW1 is formed by Q30, T32 Y23, W34, and H27 (42).

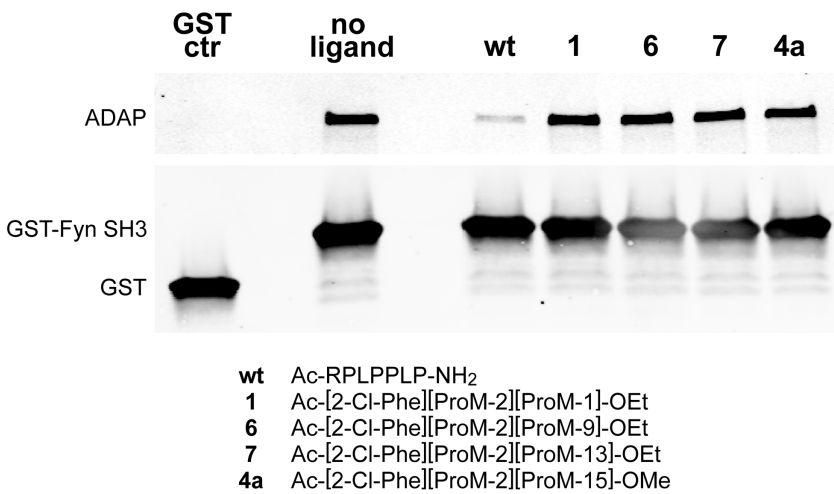


Fig. S22. Pulldown experiment of GST-tagged Fyn SH3 from Jurkat cell lysate

Natural binding partner ADAP binds to Fyn SH3 via proline-rich segments and is pulled from Jurkat cell lysate by bead-bound Fyn SH3 (43). ADAP is displaced from Fyn SH3 by the synthetic peptide Ac-RPLPPLP-NH₂ (44) but not by the inhibitors designed for Ena/VASP EVH1. Peptide and inhibitors were used at 50 μ M active concentration, 1 mg/ml protein concentration of the lysate. Chemical structures of the mentioned ProM scaffolds are printed in SI Appendix Fig. S2.

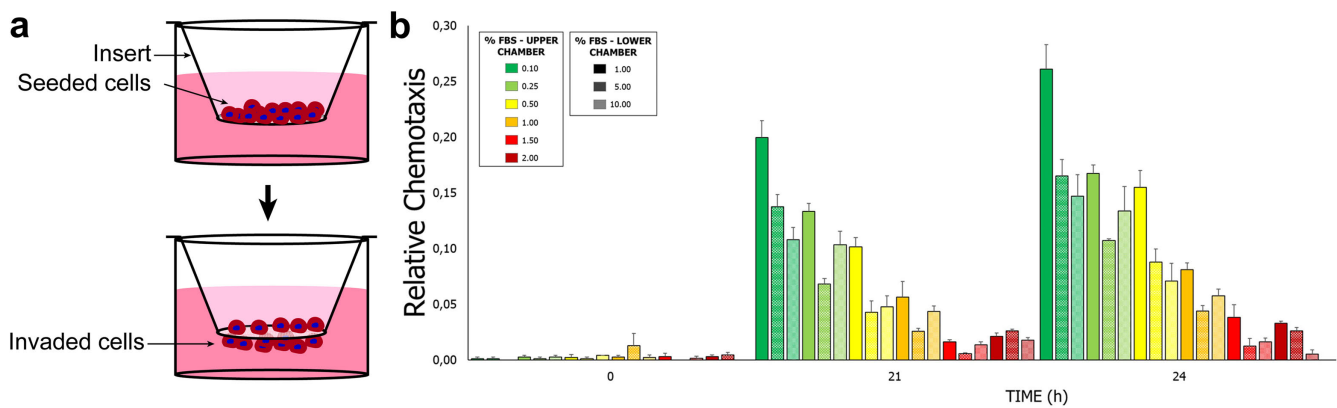


Fig. S23. IncuCyte chemotaxis assay, set-up and FBS gradient optimization

(a) Schematic figure of the IncuCyte membrane-based migration assay. (b) The FBS gradient between upper and lower wells was optimized beforehand to maximize the relative chemotaxis, e.g. the relative confluence of cells migrated. MDA-MB-231 migrated most efficiently over a gradient of 0.1 (upper) to 1% (lower). Steeper gradients and higher FBS concentrations in the upper well resulted in significantly less cells migrating to the lower well.

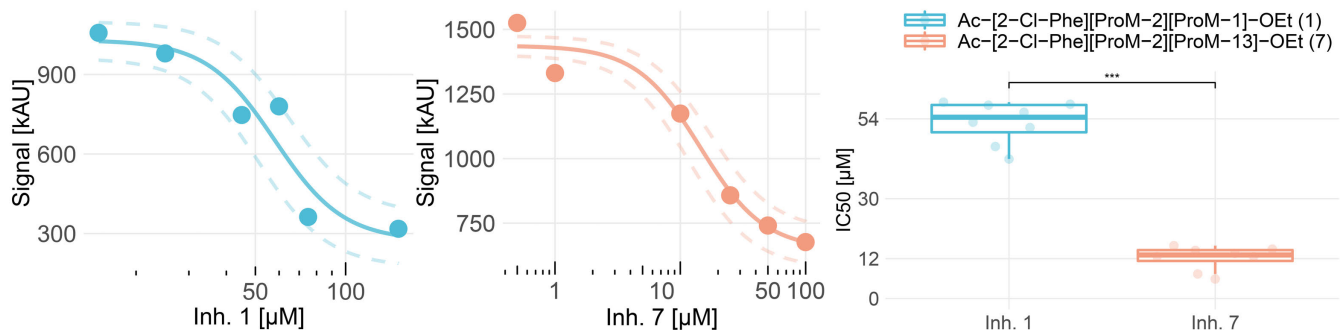


Fig. S24. Boyden chamber invasion assay

Left: MDA-MB-231 stably expressing mCherry were incubated inhibitors **1** or **7**, which reduced invasion in a dose-dependent manner. (Representative fluorescence signals after 13 h and IC₅₀ curve with 3σ dashed line). Right: IC₅₀ were calculated during linear signal increase and plotted as group ($P=2.4 \times 10^{-10}$). The calculated IC₅₀ values confirm the IncuCyte chemotaxis assay mentioned in the main text with inhibitor **7** having a superior potency compared to **1** (mean IC₅₀ 12 μ M vs 53 μ M, $P < 0.0001$).

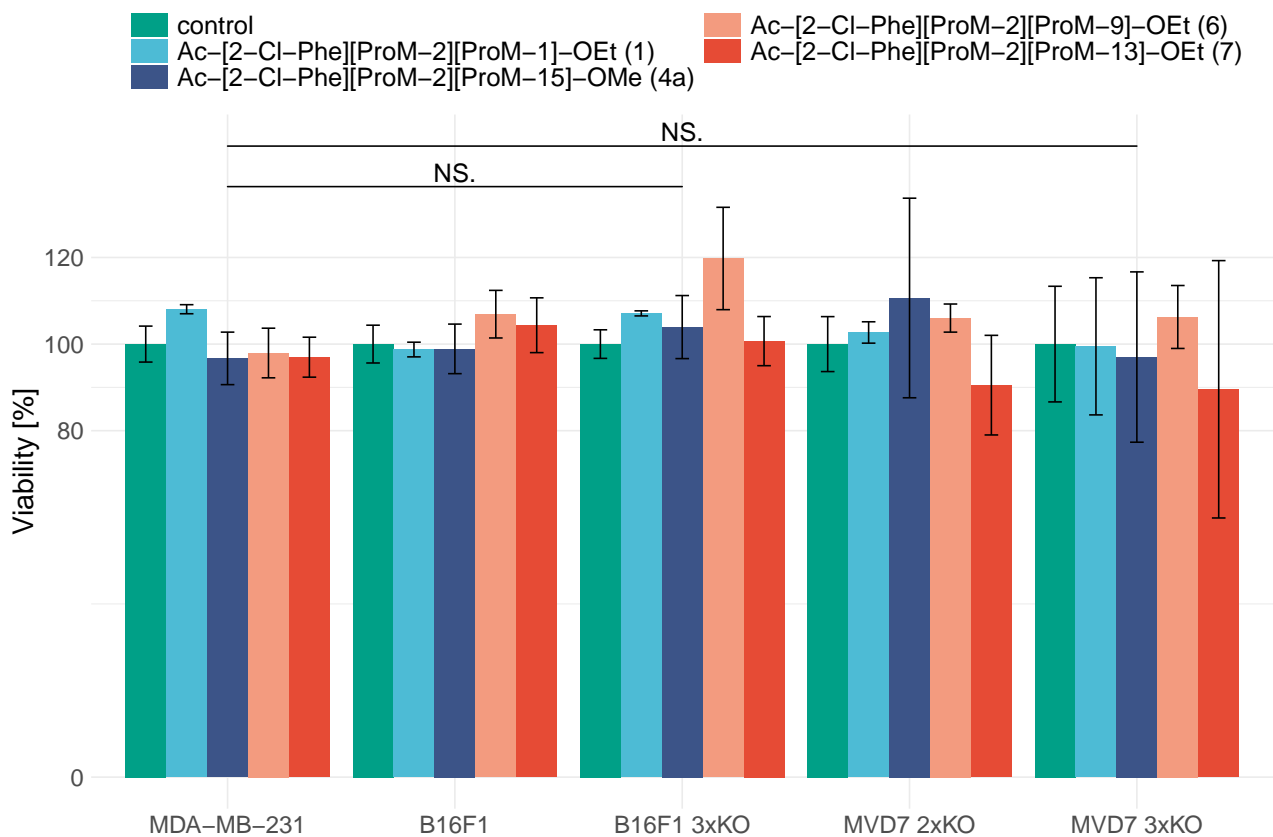


Fig. S25. Cell viability assay

Cells were incubated for 24 h with inhibitors **1**, **4a**, **6**, or **7** at 180 μ M. Fluorescence of living-cell-mediated, reduced Alamar blue (Invitrogen) was measured indicating no toxicity up to an inhibitor concentration of 180 μ M as used as maximal concentration in the IncuCyte chemotaxis assay. Three cell lines were tested: MDA-MB-231, B16F1 mouse melanoma wild-type and Ena/VASP triple knockout (3xKO), and mouse fibroblast cell line (MVD7) ENAH and VASP double (2xKO) and Ena/VASP triple knockout (3xKO). The mouse cell lines were kindly gifted by Prof. Dr. Jan Faix. Fluorescence signals normalized to the mean of the control without any inhibitor. Chemical structures of the mentioned ProM scaffolds are printed in SI Appendix Fig. S2.

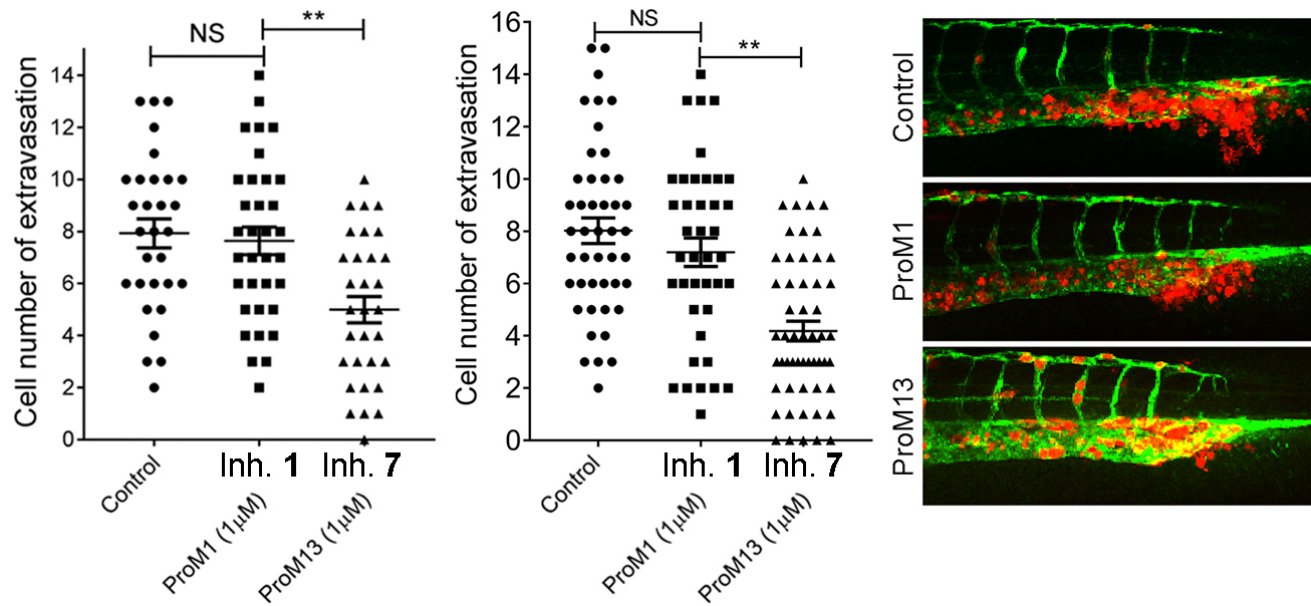


Fig. S26. Duplicates of zebrafish assays

Zebrafish assays were performed twice for each inhibitor. Representative duplicates of a zebrafish extravasation assay under inhibitor treatment with 1 μ M Ac-[2-Ci-Phe][ProM-2][ProM-1]-OEt (**1**) and Ac-[2-Ci-Phe][ProM-2][ProM-13]-OEt (**7**). Chemical structures of the mentioned ProM scaffolds are printed in SI Appendix Fig. S2.

Inhibitor characterization. Inhibitors were weighed out on fine scales (Sartorius ME36S-0CE or Mettler AT21 Comparator) and dissolved in sterile-filtered PBS or 40 mM sodium phosphate, 100 mM NaCl and titrated to pH 7.3. The batches designated for cellular experiments did not contain any reducing agents such as TCEP or DDT as mentioned in the affinity section of the methods part. FT-based affinity measurements were carried out to determine the amount of active substance, and activity-corrected concentrations were used in all cellular experiments.

The substance batches that went into cellular and *in vivo* experiments were analyzed in detail and listed first. Thereafter follow analytic data of inhibitors mentioned in the main text. Two general trends notable in nearly all of the batches are discussed here and not further mentioned:

1. MALDI TOF as well as LCMS generally show a small impurity with a molecular weight offset by +14 Da from the $[M+H]^+$ fragment as well as $[M+Na]^+$ and $[M+K]^+$. As the synthesis strategy does not allow any side reaction that would add an additional CH₂ group, the most likely impurity is a mixture between ethyl and propyl esters (for -OEt compositions) or methyl and ethyl esters (for -OMe compositions), respectively. We assume that the mixture of ester functions may have formed during masking the C-terminal scaffold by traces of ethanol and propanol in the according solvents. Furthermore, as the difference between $[M+Na+14]^+$ and $[M+K]^+$ is only 2 Da, we suggest that only a minor fraction of the recorded $[M+K]^+$ ions contributed to the impurity. Given the similar affinities of -OMe and -OEt compositions (SI Appendix Tabs. 7 and 8), we do not expect that the impurity had any effect in the cellular assays.
2. Optical activity at 280 and 254 nm is low, and inhibitors are best visible at 220 nm, where only minor impurities are detectable. UV/Vis spectrograms generally reveal a distinct double-peak elution pattern of the inhibitors. Investigation of this behavior by solution NMR and LCMS revealed that each fraction splits again into a double-peak when stored at room temperature. Furthermore, upon heating the column, the double-peak pattern of the analytical HPLC merges into one peak with an area roughly the size of the double-peak. Hence, we suggest that the observed double-peak elution pattern originates from two rotamers of the product with slightly different retention times, supposedly formed by the slow *cis-trans* isomerization of the [2-Cl-Phe]–[ProM-2] peptide bond.

Ac-[L-2Cl-F]-[ProM-2]-[ProM-1]-OMe (1a)

M(C₃₆H₄₂ClN₅O₇) 692.210 g/mol.

Yield 87% (528 mg, 76 μmol).

R_f 0.29 (MeOH/CH₂Cl₂, 1:15).

HR-MS (ESI): m/z = [M+H]⁺ calculated: 692.2846; determined: 692.2848; [M+Na]⁺ calculated 714.2665; determined: 714.2673.

¹H NMR (600 MHz, CDCl₃, mixture of rotamers): δ [ppm] = 7.38 - 7.30 (m, 1H, H-33), 7.26 - 7.14 (m, 3H, H-30/31/32), 6.41 (d, J = 8.1 Hz, 0.3H, -NH^{rot2}), 6.16 (dd, J = 41.5 Hz, 9.0 Hz, 0.7H, -NH^{rot2}), 5.94 - 5.74 (m, 2H, H-17/18), 5.67 - 5.52 (m, 1H, H-5 o. 6), 5.22 - 5.14 (m, 1H, H-11), 4.99; 4.94 (2×t, J = 8.2 Hz, 8.0 Hz, 0.7H, H-23^{rot1}), 4.85 (t, J = 8.4 Hz, 0.3H, H-23^{rot2}), 4.80 - 4.70 (m, 2H, H-5 o. 6/19), 4.60 - 4.53 (m, 1H, H-16), 4.41 - 4.33 (m, 1H, H-7), 4.18 - 4.04 (m, 1H, H-13), 3.99 - 3.89 (m, 1H, H-1), 3.84 - 3.77 (m, 0.7H, H-1^{‘rot1}), 3.71; 3.70 (2×s, 3H, H-25), 3.59 - 3.48 (m, 1H, H-13[‘]), 3.38 (dd, J = 14.2 Hz, 3.8 Hz, 0.3H, H-1^{rot2}), 3.23 - 3.10 (m, 1.4H, H-28/28^{rot2}), 3.04 - 2.95 (m, 1H, H-15), 2.85 (dd, J = 14.2 Hz, 10.7 Hz, 0.6H, H-28^{‘rot1}), 2.50 - 2.44 (m, 0.6H, H-10^{rot1}), 2.41 - 2.36 (m, 0.4H, H-10^{rot2}), 2.35 - 2.24 (m, 2H, H-3[‘]/22[‘]), 2.22 - 1.70 (m, 14H, H-2/3/9/10[‘]/14/21/22/36).

¹³C NMR (150 MHz, CDCl₃, mixture of rotamers): δ [ppm] = 172.3 (C-8), 171.1; 170.9 (C-20), 170.1 (C-26), 169.6; 169.2 (C-24), 169.0; 168.9 (C-35), 166.9; 166.8 (C-12), 134.6; 134.5 (C-29), 134.4 (C-34), 132.0; 131.9 (C-17), 131.4; 130.9 (C-5), 129.5; 129.5 (C-6), 129.4; 129.4 (C-33), 128.5 (C-18), 128.4; 128.3 (C-32), 126.6; 126.5 (C-31), 123.1; 122.9 (C-30), 65.3; 65.2 (C-4), 62.1; 62.0 (C-23), 59.4; 59.3 (C-16), 59.0; 57.5 (C-11), 57.3; 56.8 (C-19), 56.2; 56.1 (C-7), 52.2 (C-25), 50.6; 50.44 (C-27), 48.6; 48.5 (C-1), 47.1; 47.0 (C-13), 40.4 (C-15), 38.1; 37.7 (C-3), 37.3; 36.0 (C-21), 32.9 (C-28), 31.6; 31.5 (C-9), 31.3; 31.0 (C-14), 28.1; 28.0 (C-22), 27.1; 26.9 (C-10), 23.9; 23.6 (C-2), 23.3; 23.0 (C-36).

IR (ATR) ν (cm⁻¹) = 3313 (bs), 3056 (w), 2956 (w), 1744 (s), 1637 (s), 1524 (w), 1437 (m), 1324 (w), 1265 (s), 1207 (m), 1053 (w), 896 (w), 731 (s), 702 (s).

[α]_λ²⁰ (c = 0.515, CHCl₃) = -456.3 ° (436 nm), -259.2 ° (546 nm), -226.6 ° (579 nm), -218.1 ° (589 nm).

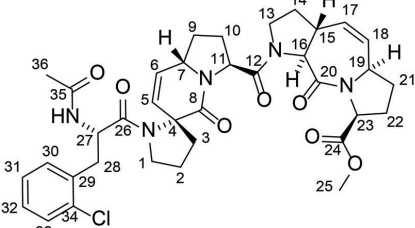


Fig. S27. Representative full characterization of inhibitor 1a

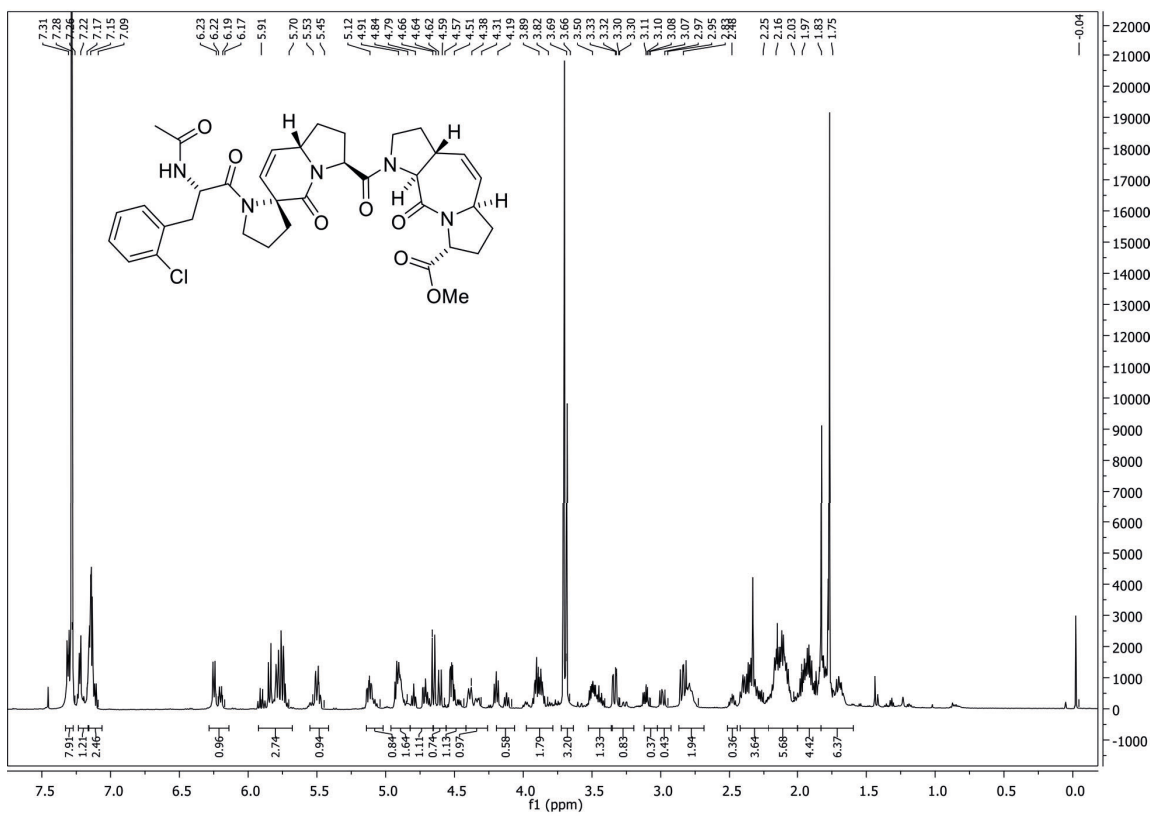
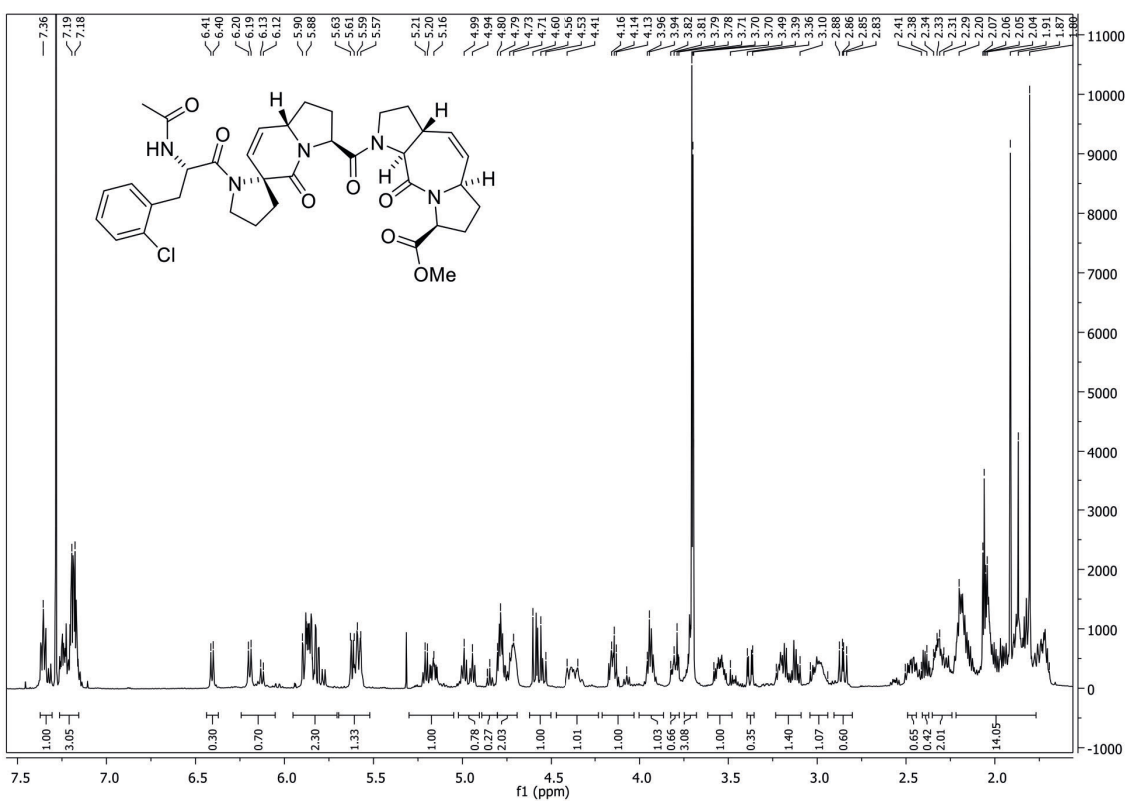
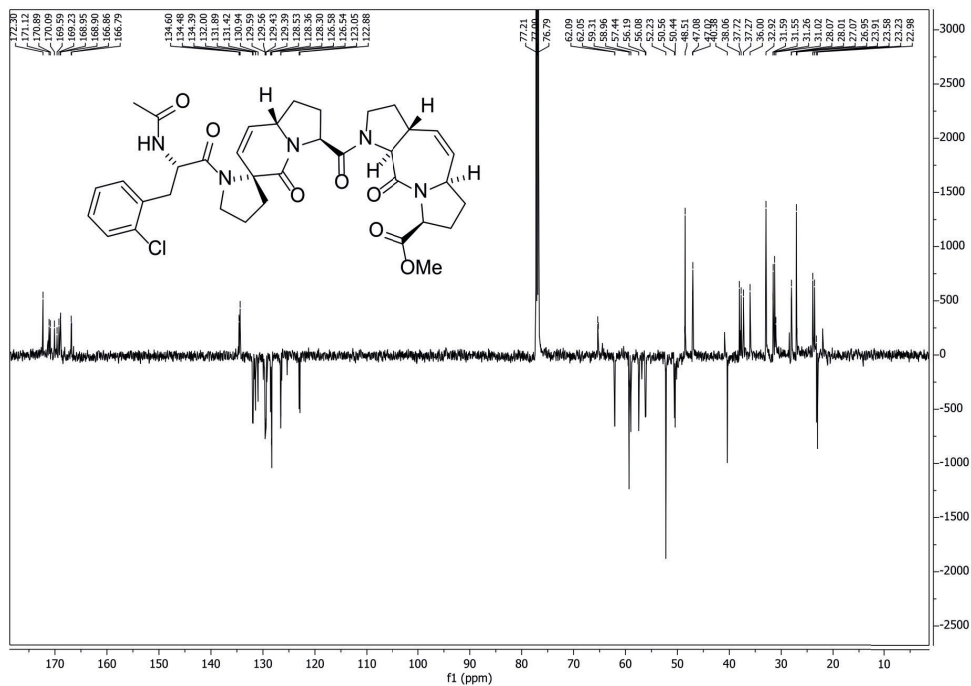
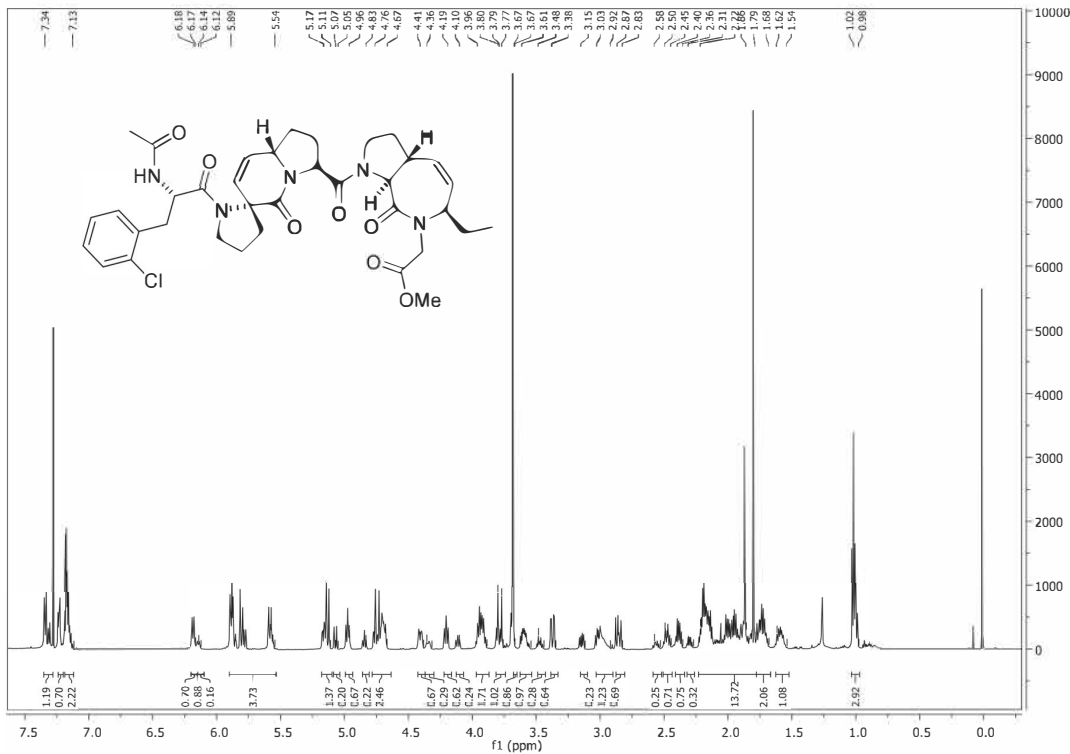


Fig. S28. 1D ¹H NMR of inhibitors **1a and **3a****

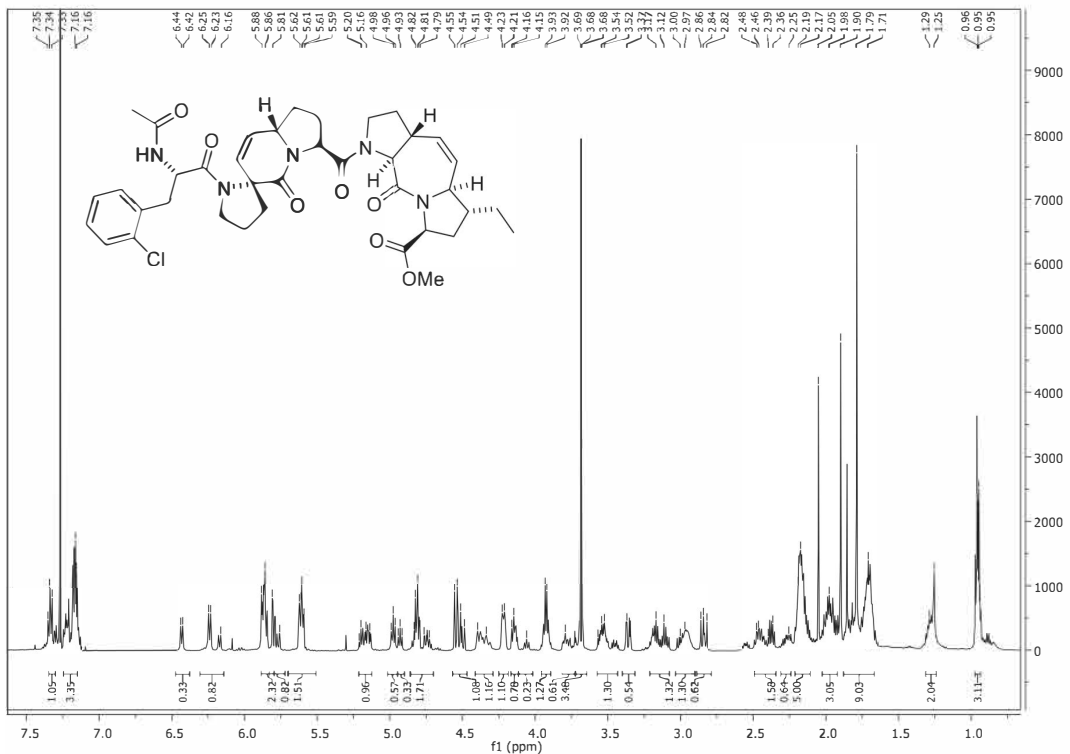


Identification code	slim377_2
Empirical formula	C ₃₆ H ₄₂ Cl N ₅ O ₇
Moiety formula	C ₃₆ H ₄₂ Cl N ₅ O ₇
Formula weight	692.19
Temperature	(100(2) K
Wavelength	1.54178 Å
Crystal system	Orthorhombic
Space group	P2 ₁ 2 ₁ 2 ₁
Unit cell dimensions	a = 9.6745(3) Å a = 90°. b = 15.9575(5) Å b = 90°. c = 21.8232(6) Å g = 90°.
Volume	3369.08(18) Å ³
Z	4
Density (calculated)	1.365 Mg/m ³
Absorption coefficient	1.484 mm ⁻¹
F(000)	1464
Crystal size	0.200 x 0.200 x 0.070 mm ³
Theta range for data collection	3.431 to 72.509°
Index ranges	-11<=h<=11, -14<=k<=19, -27<=l<=26
Reflections collected	29741
Independent reflections	6632 [R(int) = 0.0356]
Completeness to theta = 67.679°	99.9 %
Absorption correction	Semi-empirical from equivalents
Max. and min. transmission	0.7536 and 0.5432
Refinement method	Full-matrix least-squares on F ²
Data / restraints / parameters	6632 / 0 / 444
Goodness-of-fit on F ²	1.030
Final R indices [$\bar{I} > 2\sigma(I)$]	R1 = 0.0327, wR2 = 0.0840
R indices (all data)	R1 = 0.0342, wR2 = 0.0851
Absolute structure parameter	0.049(5)
Extinction coefficient	n/a
Largest diff. peak and hole	0.301 and -0.417 e.Å ⁻³

Fig. S29. 1D ¹³C NMR and small molecule crystal structure of inhibitor **1a**



¹H NMR spectrum of **4a**, measured in CDCl₃ (600 MHz).



¹H NMR spectrum of **7a**, measured in CDCl₃ (600 MHz).

Fig. S30. 1D ^1H NMR of inhibitors 4a and 7a

Ac-[2-Cl-Phe][ProM-2][ProM-1]-OEt. Inhibitor Ac-[2-Cl-Phe][ProM-2][ProM-1]-OEt (**1**) has molecular weight of 706.24 Da. Shown here is the analysis of the inhibitor batch used in cellular experiments. MALDI TOF as well as LCMS show a small impurity with a molecular weight offset by 14 Da from $[M + H]^+$ as well as $[M + Na]^+$ and $[M + K]^+$ as mentioned before. UV/Vis spectrograms reveal a distinct double-peak elution of the inhibitor as mentioned before. The synthesis batch of **1** contained minor traces of Fmoc-[2-Cl-Phe][ProM-2][ProM-1]-OEt. These impurities are visible only when dissolved in acetonitrile-water mixtures (such as the LCMS and MALDI TOF of SI *Appendix* Fig. S31a and c). As Fmoc-compositions are not water soluble, the supernatant of the dissolved batches used for the cellular studies was free of Fmoc-impurities (see HPLC SI *Appendix* Fig. S31b and SI *Appendix* Tab 11).

Ret. time [min]	Relative peak area [%]
4.851	0.1
5.493	0.1
5.888	0.4
5.966	0.4
6.165	0.3
6.45	1.8
6.679	0.7
6.88	1.6
7.175	1.6
7.69	91.9
8.532	0.7
8.706	0.1
8.983	0.4
total	100

Tab. S11. HPLC peak table of inhibitor Ac-[2-Cl-Phe][ProM-2][ProM-1]-OEt at 220 nm

Peak areas of the HPLC run visible in SI *Appendix* Fig. S31b left panel, relative to the total area under the 220 nm spectrogram.

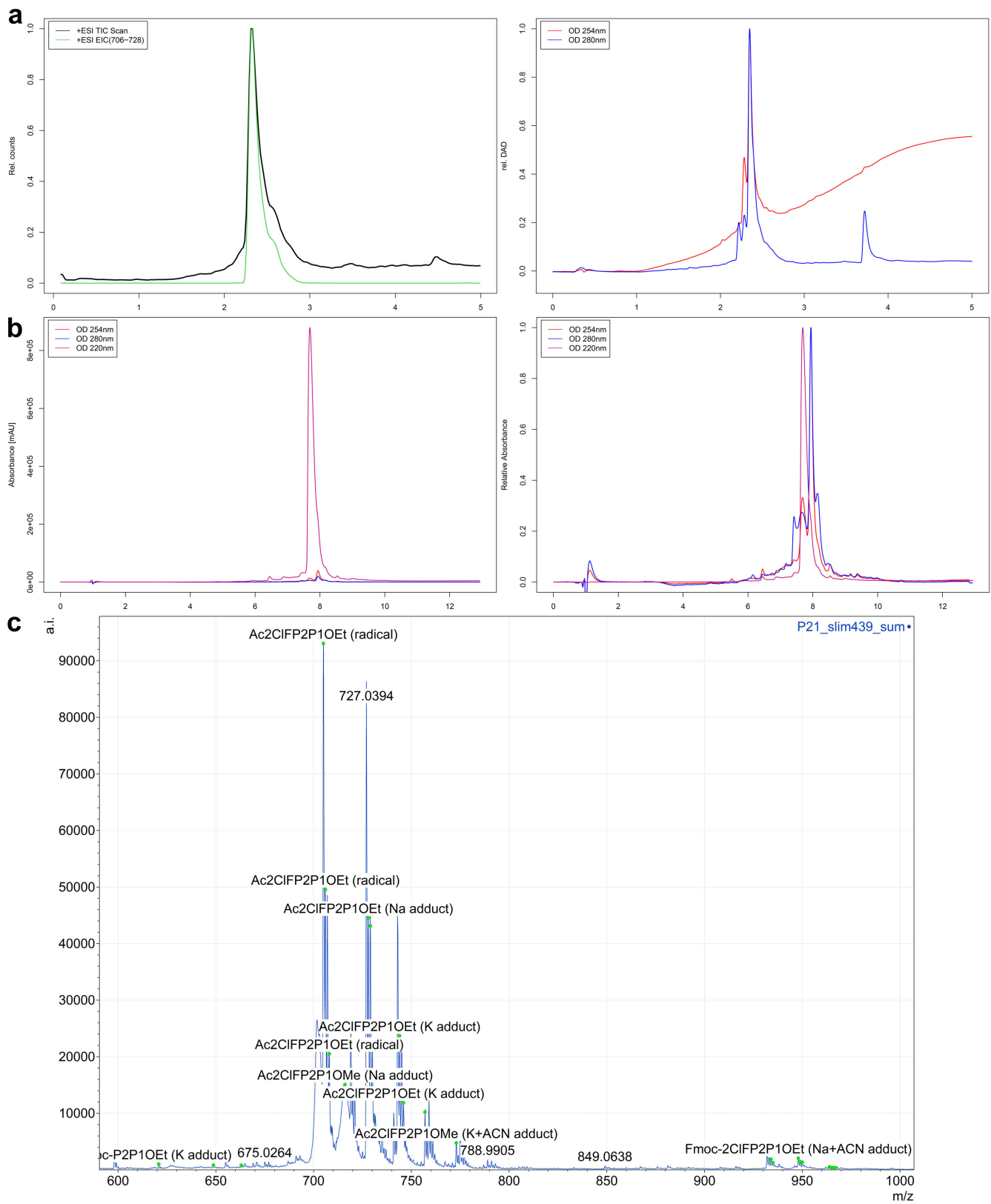


Fig. S31. Analysis of Ac-[2-Cl-Phe][ProM-2][ProM-1]-OEt (1)

(a) LCMS. TIC scan and UV spectrograms, both normalized to the maximal signal during acquisition time (minutes). (b) Analytical HPLC. UV spectograms on absolute scale (left) and normalized to the according maximal OD (right) during acquisition time (minutes). (c) MALDI TOF with assigned fragments.

Ac-[2-Cl-Phe][ProM-2][ProM-15]-OMe. Inhibitor Ac-[2-Cl-Phe][ProM-2][ProM-15]-OMe (**4a**) has molecular weight of 694.23 Da. Shown here is the analysis of the inhibitor batch used in cellular experiments. Generally, the impurity offset by 14 Da from $[M+H]^+$ as well as $[M+Na]^+$ and $[M+K]^+$ as mentioned before is more dominant for methyl ester-masked inhibitors compared to the ethyl ester compositions. Indeed, scanning for Ac-[2-Cl-Phe][ProM-2][ProM-15]-OEt ($[M+H]^+$ of 708.27 Da) reveals a notable signal in the total ion current (TIC) chromatogram profile (brown line SI *Appendix* Fig. S32a) but no further impurities. UV/Vis spectrograms reveal a distinct double-peak elution of the inhibitor as mentioned before. The supernatant used for cellular studies, as analyzed by MALDI TOF (SI *Appendix* Fig. S32c) is virtually free of Fmoc-bound intermediates.

Ret. time [min]	Relative peak area [%]
3.581	0.1
5.252	0.1
5.42	0.1
5.963	0.1
6.098	0.1
6.474	0.2
7.509	1.7
7.8	96.6
9.027	0.6
9.775	0.3
10.037	0.2
total	100

Tab. S12. HPLC peak table of inhibitor Ac-[2-Cl-Phe][ProM-2][ProM-15]-OMe at 220 nm

Peak areas of the HPLC run visible in SI *Appendix* Fig. S32b left panel, relative to the total area under the 220 nm spectrogram.

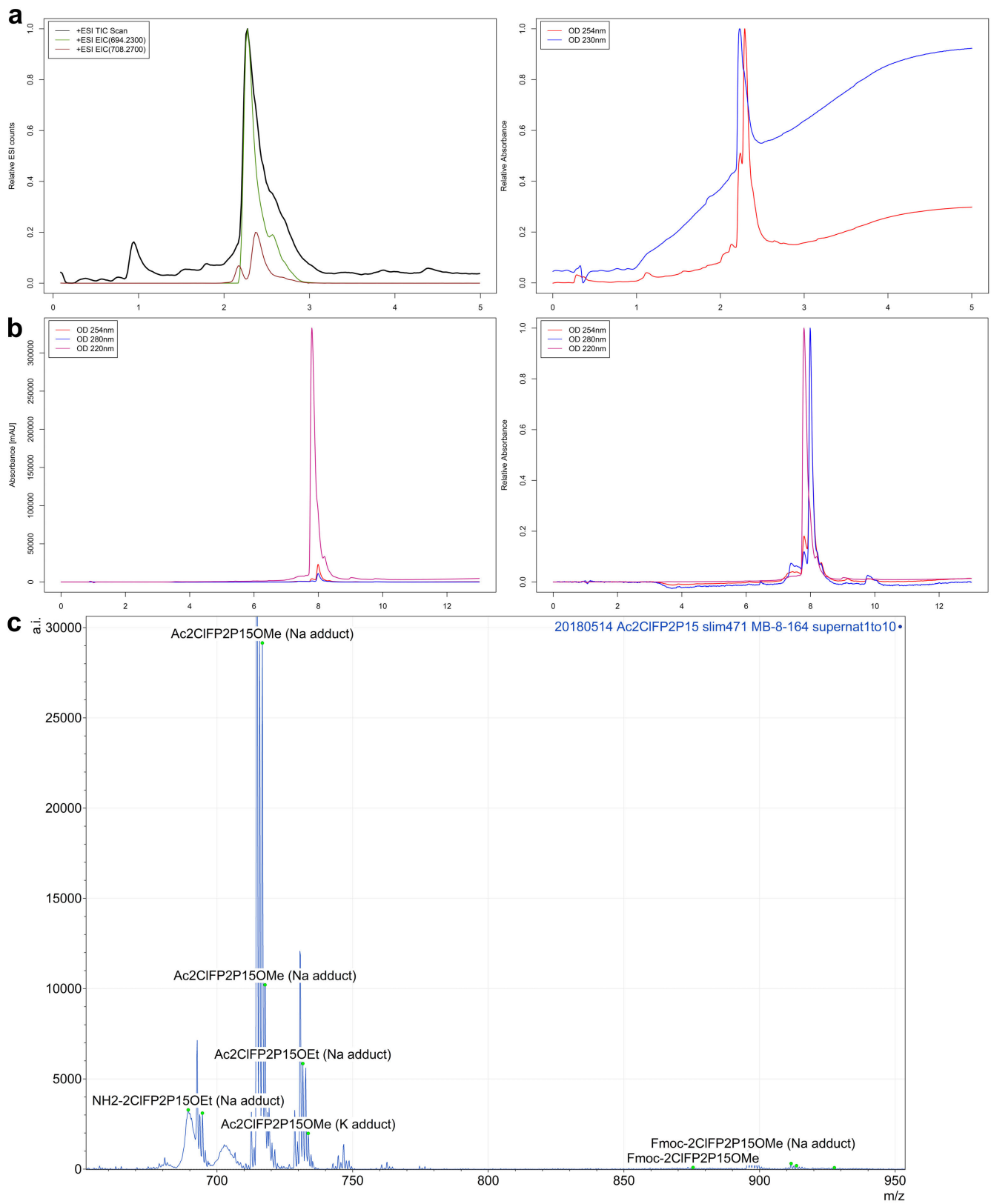


Fig. S32. Analysis of Ac-[2-Cl-Phe][ProM-2][ProM-15]-OMe (4a)

(a) LCMS. TIC scan and UV spectrograms, both normalized to the maximal signal during acquisition time (minutes). (b) Analytical HPLC. UV spectograms on absolute scale (left) and normalized to the according maximal OD (right) during acquisition time (minutes). (c) MALDI TOF with assigned fragments.

Ac-[2-Cl-Phe][ProM-2][ProM-9]-OEt. Inhibitor Ac-[2-Cl-Phe][ProM-2][ProM-9]-OEt (**6**) has molecular weight of 720.26 Da. Shown here is the analysis of the inhibitor batch used in cellular experiments. MALDI TOF as well as LCMS show a small impurity with a molecular weight offset by 14 Da from $[M+H]^+$ as well as $[M+Na]^+$ and $[M+K]^+$ as mentioned before. UV/Vis spectrograms reveal a distinct double-peak elution of the inhibitor as mentioned before. Even though LCMS and HPLC spectrograms reveal more peaks leading and trailing the double-peak, no ions other than $[M+H]^+$ $[M+Na]^+$ and $[M+K]^+$ were found (in accordance to the MALDI TOF).

Ret. time [min]	Relative peak area [%]
7.597	2.8
7.856	4.3
8.271	92.5
10.348	0.1
10.723	0.2
total	100

Tab. S13. HPLC peak table of inhibitor Ac-[2-Cl-Phe][ProM-2][ProM-9]-OEt at 220 nm

Peak areas of the HPLC run visible in SI Appendix Fig. S33b left panel, relative to the total area under the 220 nm spectrogram.

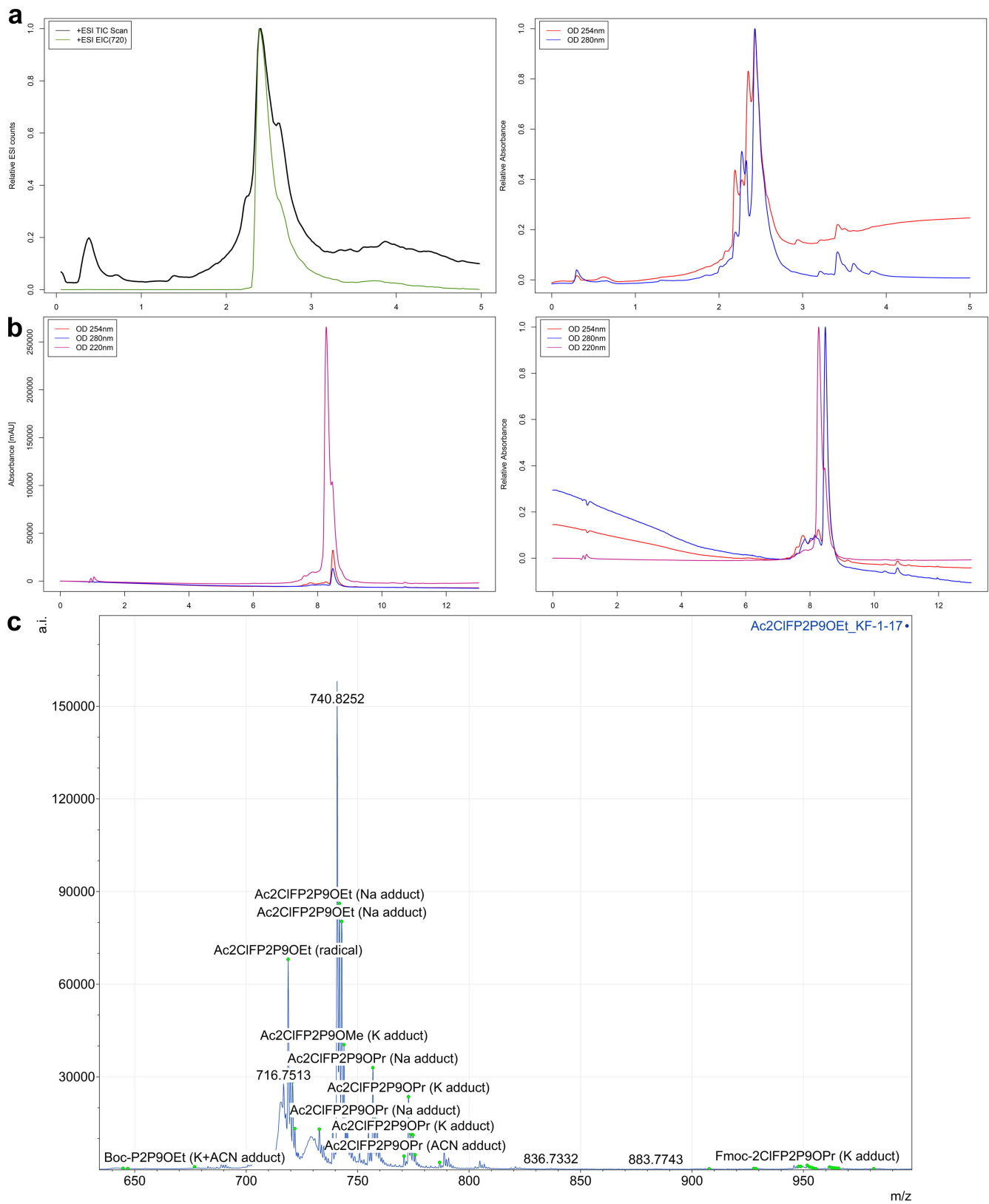


Fig. S33. Analysis of Ac-[2-Cl-Phe][ProM-2][ProM-9]-OEt (6)

(a) LCMS. TIC scan and UV spectrograms, both normalized to the maximal signal during acquisition time (minutes). (b) Analytical HPLC. UV spectograms on absolute scale (left) and normalized to the according maximal OD (right) during acquisition time (minutes). (c) MALDI TOF with assigned fragments.

Ac-[2-Cl-Phe][ProM-2][ProM-13]-OEt. Inhibitor Ac-[2-Cl-Phe][ProM-2][ProM-13]-OEt (**7**) has molecular weight of 734.29 Da. Shown here is the analysis of the inhibitor batch used in cellular experiments. MALDI TOF as well as LCMS show a small impurity with a molecular weight offset by 14 Da from $[M+H]^+$ as well as $[M+Na]^+$ and $[M+K]^+$ as mentioned before. UV/Vis spectrograms reveal a distinct double-peak elution of the inhibitor as mentioned before.

Ret. time [min]	Relative peak area [%]
2.133	0.1
3.588	0.3
5.252	0.3
5.418	0.5
5.968	0.2
6.454	0.4
6.646	0.2
7.552	0.2
7.757	0.8
7.915	0.2
8.064	0.5
8.439	1.8
8.8	94.6
total	100

Tab. S14. HPLC peak table of inhibitor Ac-[2-Cl-Phe][ProM-2][ProM-13]-OEt at 220 nm

Peak areas of the HPLC run visible in SI Appendix Fig. S34b left panel, relative to the total area under the 220 nm spectrogram.

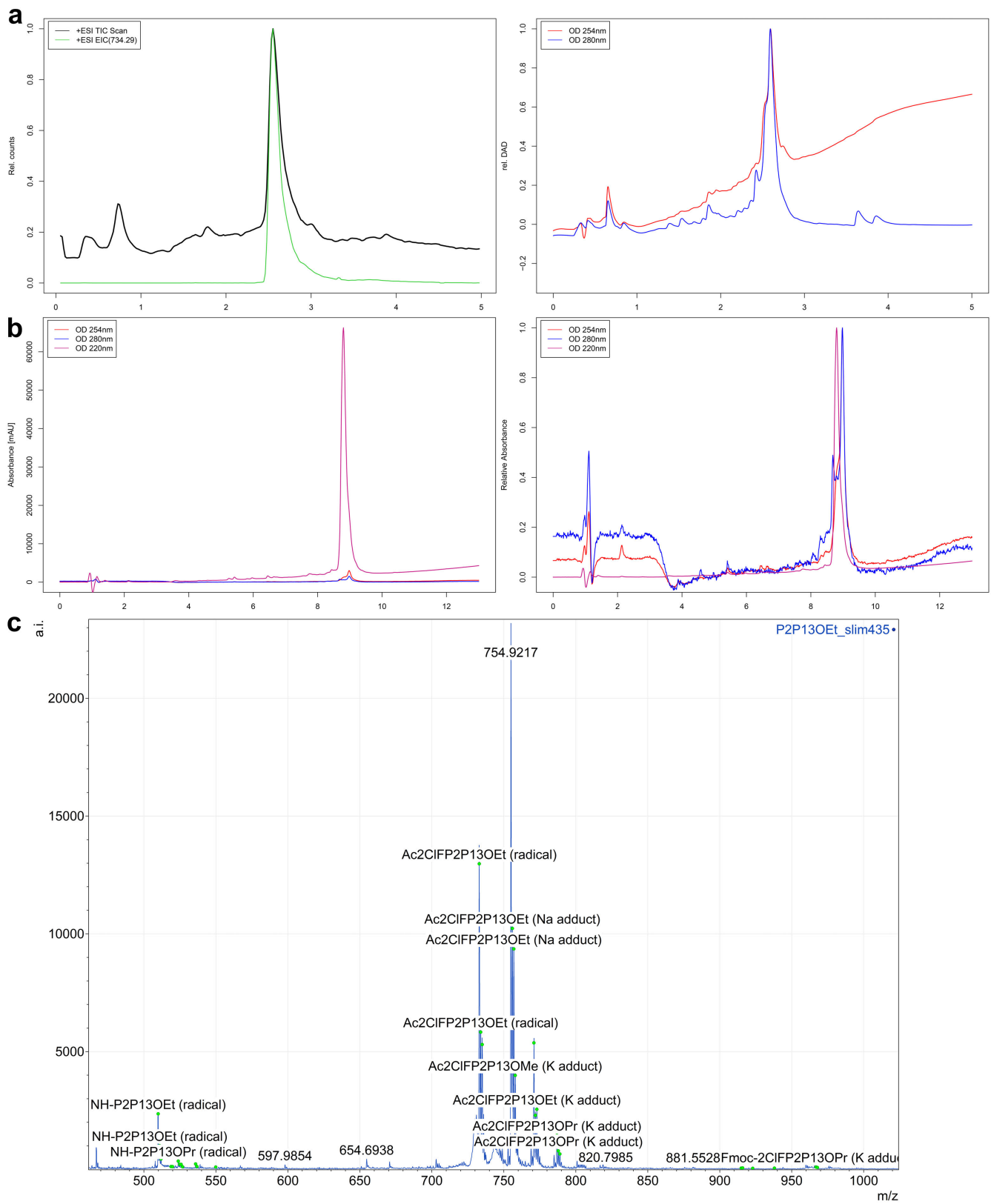
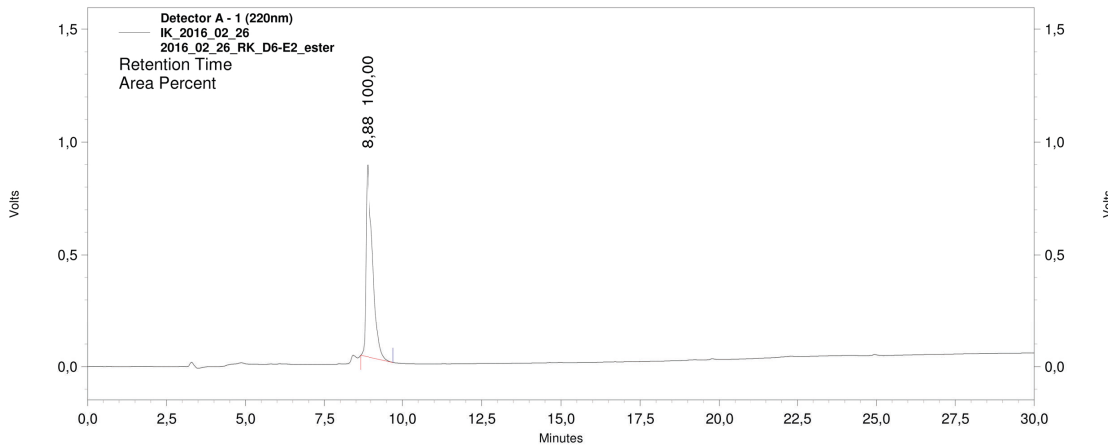


Fig. S34. Analysis of Ac-[2-Cl-Phe][ProM-2][ProM-13]-OEt (7)

(a) LCMS. TIC scan and UV spectrograms, both normalized to the maximal signal during acquisition time (minutes). (b) Analytical HPLC. UV spectrograms on absolute scale (left) and normalized to the according maximal OD (right) during acquisition time (minutes). (c) MALDI TOF with assigned fragments.



Detector A - 1 (220nm)					
Pk #	Retention Time	Area	Area %	Height	Height %
1	8,883	13219601	100,000	855541	100,000
Totals		13219601	100,000	855541	100,000

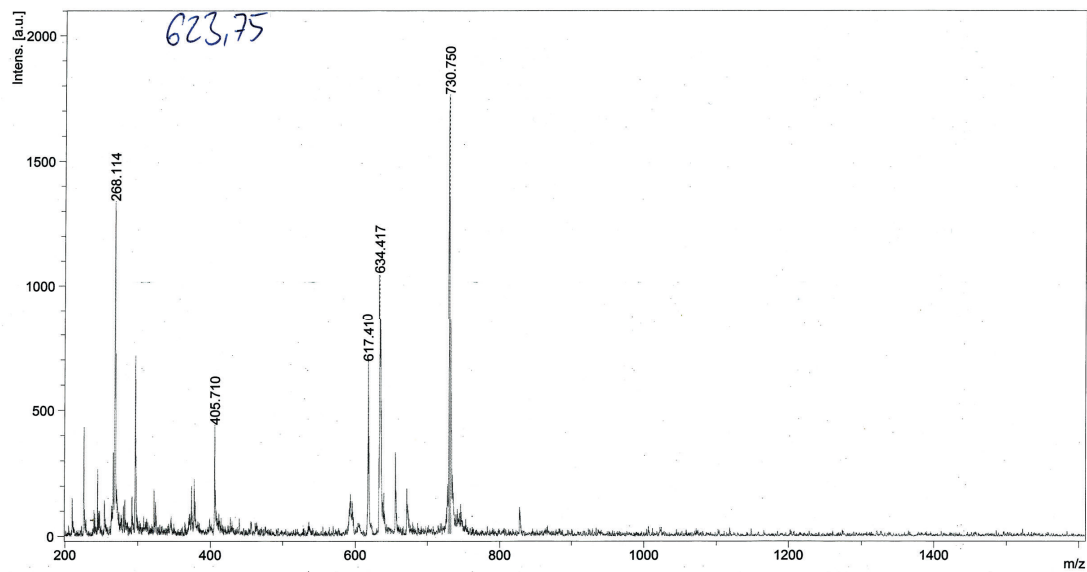
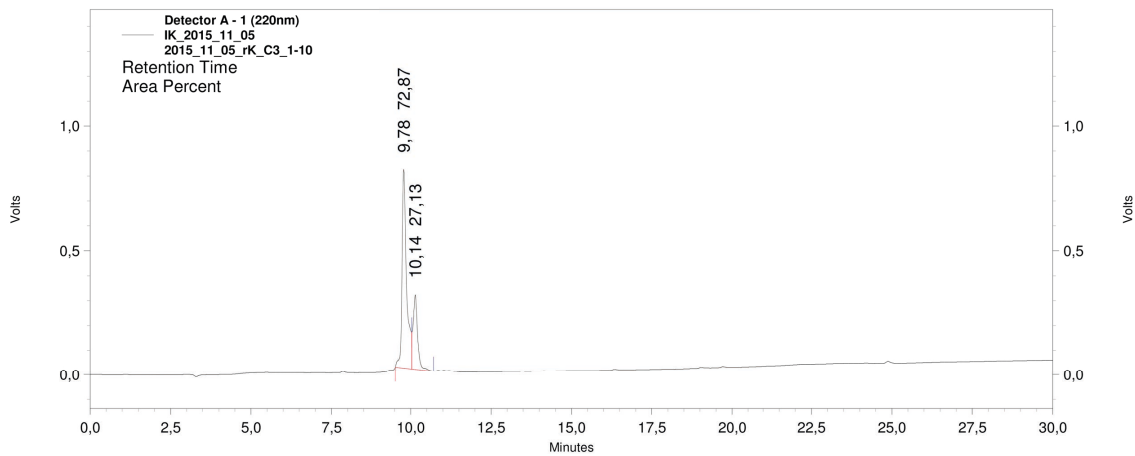


Fig. S35. Analysis of Ac-FPPPPP-OEt

HPLC and MALDI TOF of peptide **wt1**, molecular weight 623.75 Da. The peptide was synthesized as free acid, followed by Steglich esterification. Ac-FPPPP-OH is detected as $[M+Na]^+$ (618.7 Da) and $[M+K]^+$ (634.7 Da). The MALDI TOF ion with 730.75 Da could not be assigned. One ion, the hexapeptide Ac-FPPPPP-OH, $[M+Na]^+$ (728.34 Da) would have a similar molecular weight but is not detected in the HPLC. Instead, the UV/Vis spur reveals a hydrophobic substance eluting at the end of the acetonitrile gradient. However, no Fmoc-containing composition fit to 730.75 Da.



Detector A - 1 (220nm)					
Pk #	Retention Time	Area	Area %	Height	Height %
1	9,783	7870156	72,873	797946	72,715
2	10,142	2929704	27,127	299411	27,285

Totals			10799860	100,000	1097357	100,000
--------	--	--	----------	---------	---------	---------

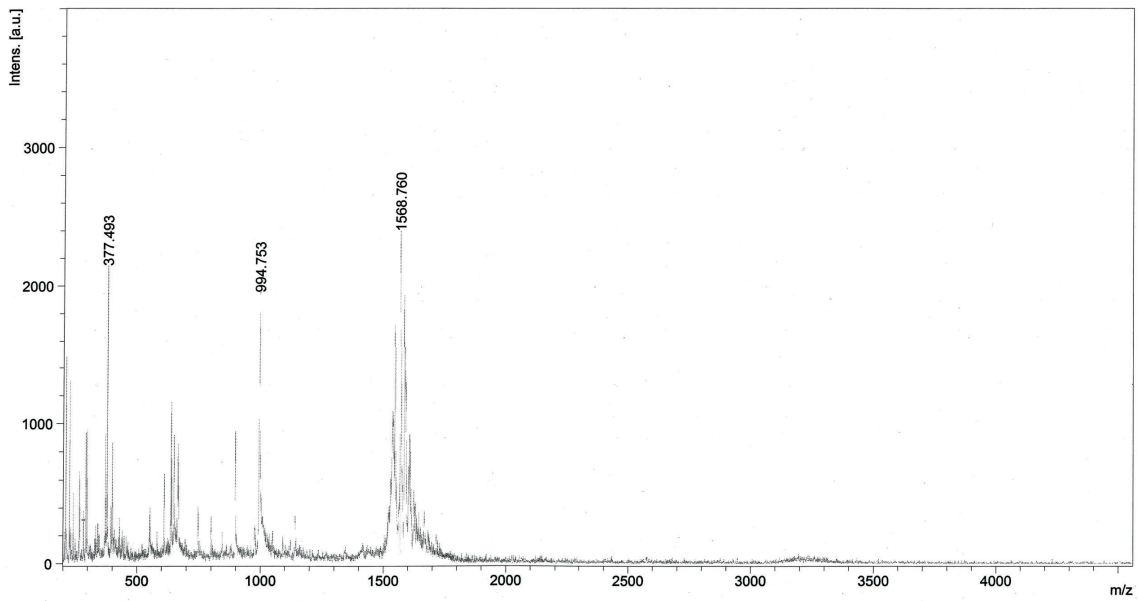
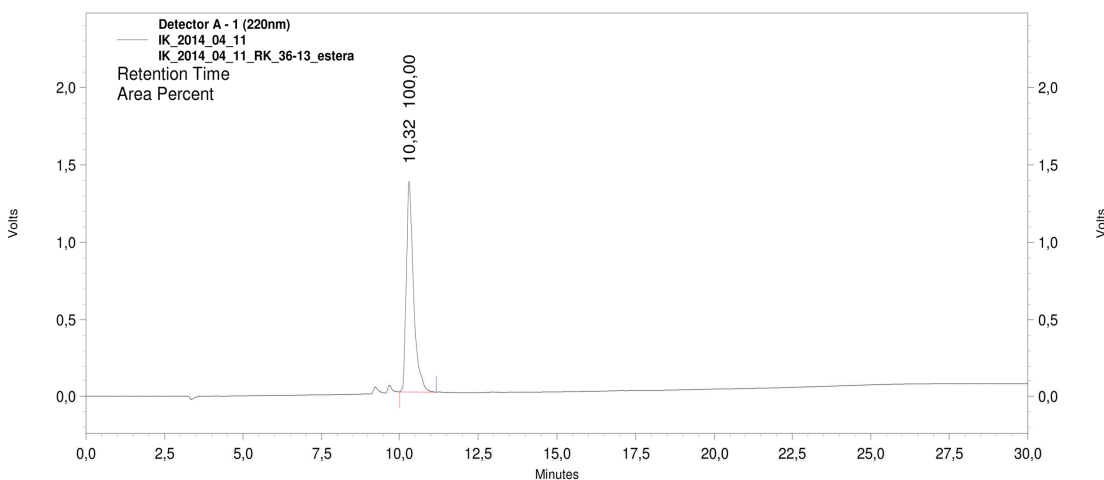


Fig. S36. Analysis of Ac-SFEFPPPPTEDEL-NH₂

HPLC and MALDI TOF of peptide wt2, molecular weight 1545.67 Da, visible as [M+Na]⁺.



Detector A - 1 (220nm)

Pk #	Retention Time	Area	Area %	Height	Height %
1	10,317	21920452	100,000	1365972	100,000
Totals		21920452	100,000	1365972	100,000

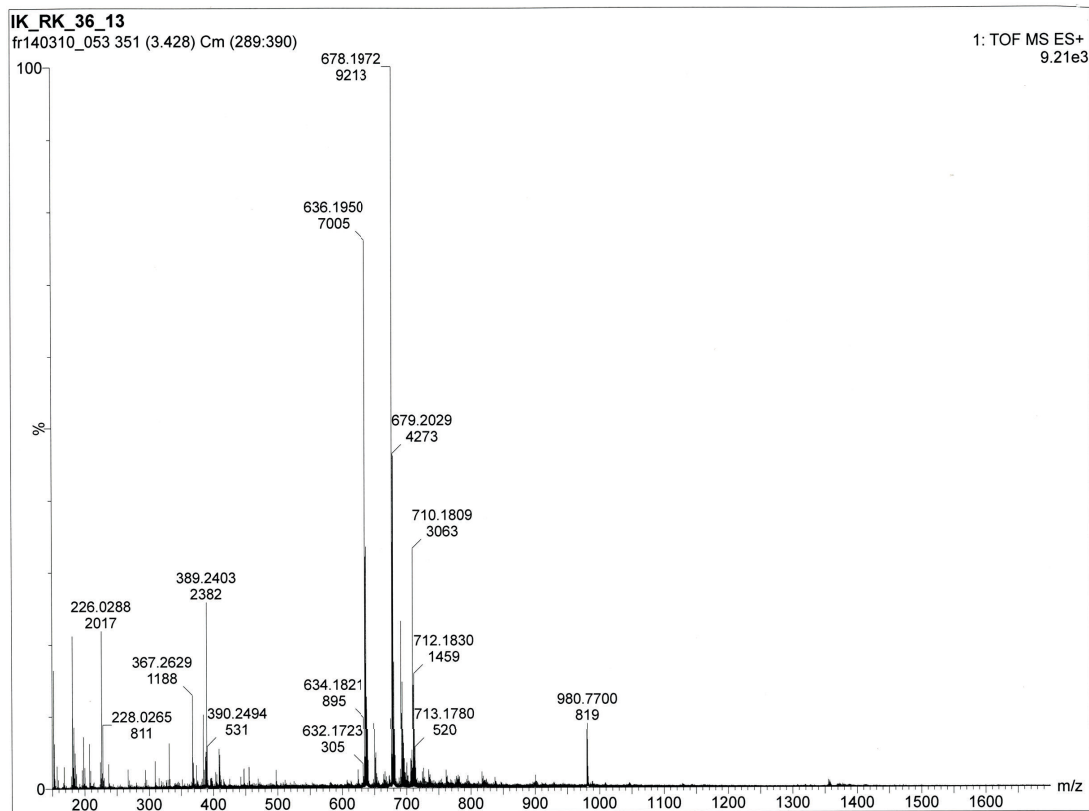
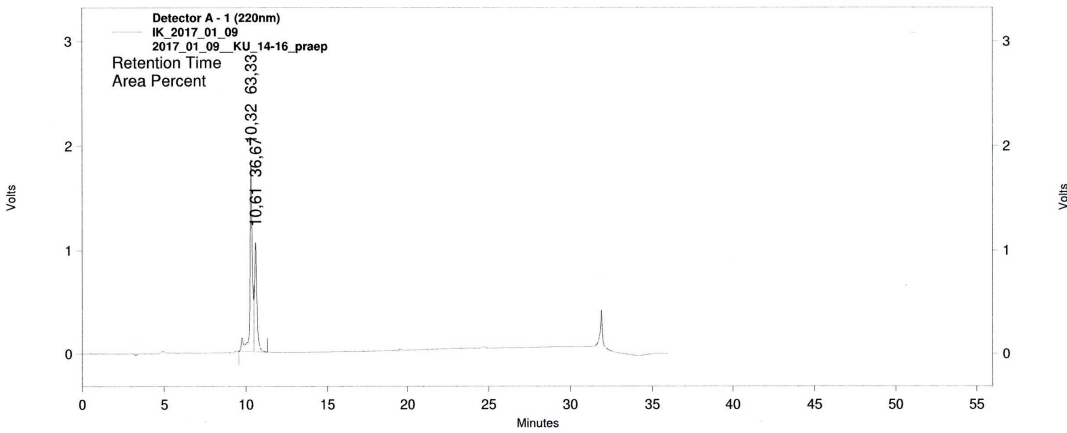


Fig. S37. Analysis of Ac-[2-Cl-Phe][ProM-2][ProM-1]-OH

HPLC and ESI-FTMS of inhibitor **1b**, molecular weight 678.18 Da. MALDI TOF reveals $[M+H]^+$ as well as the deacetylated fragment (636.2 Da). The small impurity with 980.8 Da could originate from a fraction of Fmoc-bound precursor (858.4 Da).



Detector A - 1 (220nm)

Pk #	Retention Time	Area	Area %	Height	Height %
1	10,325	19008274	63,330	1847890	63,637
2	10,608	11006554	36,670	1055923	36,363
Totals		30014828	100,000	2903813	100,000

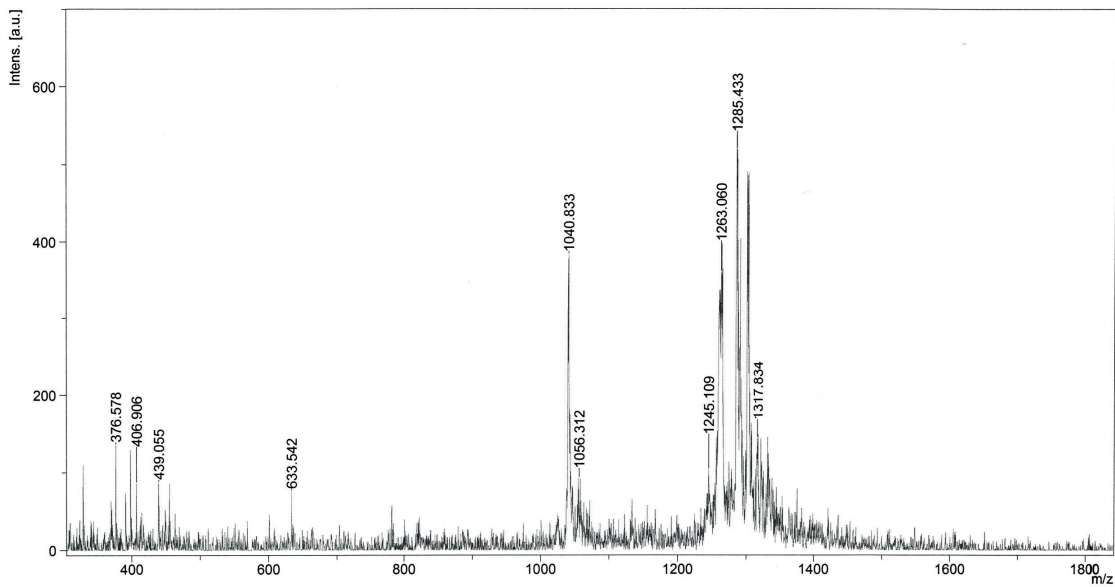
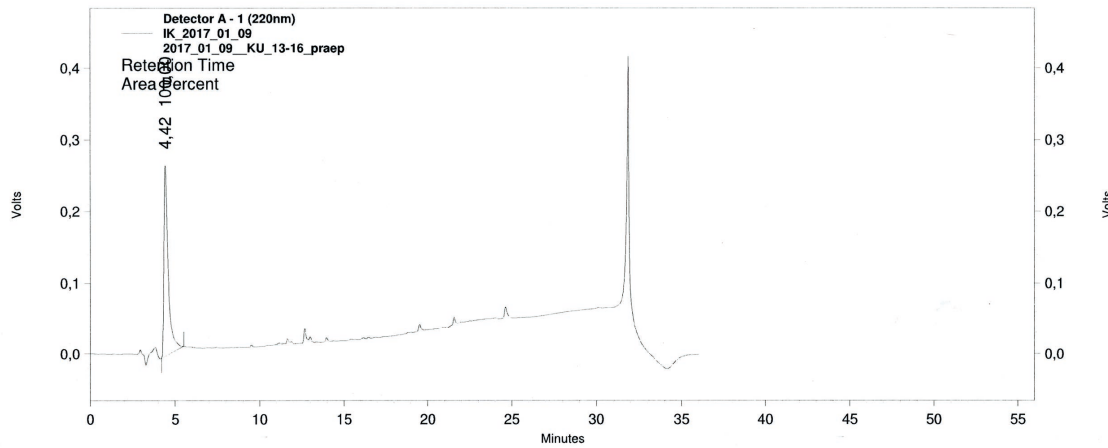


Fig. S38. Analysis of Ac-[2-Cl-Phe][ProM-2][ProM-1]TEDEL-NH₂

HPLC and MALDI TOF of compound **2ΔN**, molecular weight 1264.78 Da. Beside the expected ions, MALDI TOF reveals a significantly smaller ion (1040.8 Da). We suspect that this side product originated from unsuccessful coupling of Fmoc-ProM-2 to the growing chimera. The deacetylated fragment Ac-[2-Cl-Phe][ProM-1]TEDEL-NH₂ weighs 1004 Da, its [M+K]⁺ 1043.5 Da. Due to the absence of two prolines within the core recognition motif, such a composition would not bind in *in vitro* assays.



Detector A - 1 (220nm)					
Pk #	Retention Time	Area	Area %	Height	Height %
1	4,417	4623050	100,000	267360	100,000
Totals		4623050	100,000	267360	100,000

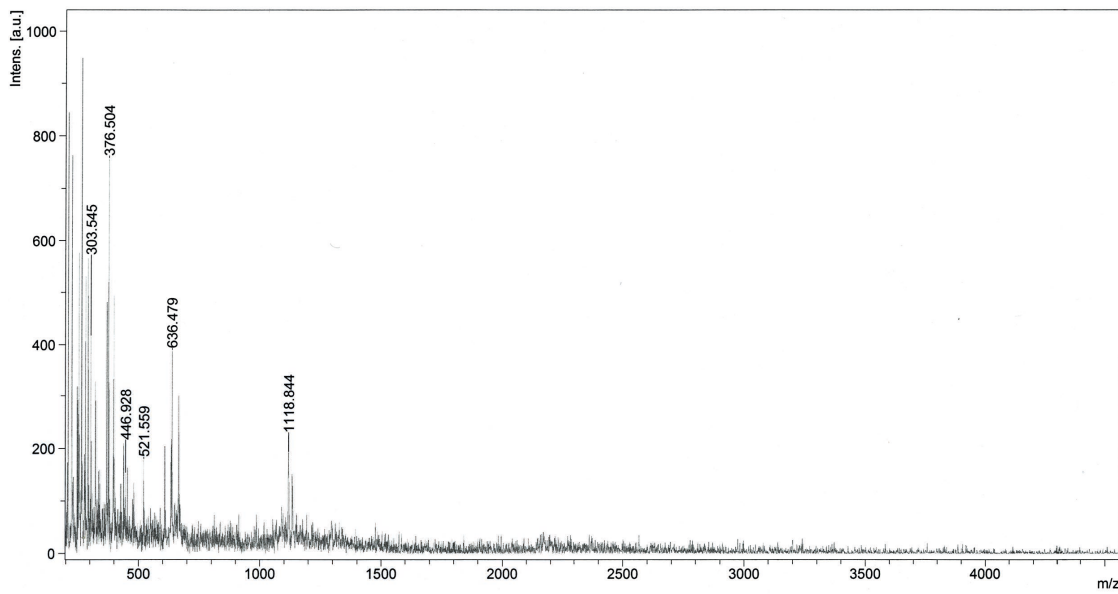


Fig. S39. Analysis of Ac-SFE[2-Cl-Phe][ProM-2][ProM-1]-OEt

HPLC and MALDI TOF of compound **2ΔC**, molecular weight 1069.61 Da. HPLC elution profile suggest several termination products. Some of the low molecular weight ions suggest that the ProM scaffolds might not have bound to the resin: The $[M+K]^+$ of the deacetylated fragment Ac-SFE-OEt (448.43 Da), Fmoc-SFE-OEt (631.7 Da), or Ac-SFE[2-Cl-Phe]-OEt (633.1 Da) all closely match the found ions in MALDI. The ion with 1118.8 Da mass should be the deacetylated product fragment (1014.5 Da) as no other composition matches that ion mass. Hydrophobic impurities were spun down after diluting the substance in phosphate buffer. Despite a low activity, the affinity could be determined accurately (percentage standard error K_d 5.7%).

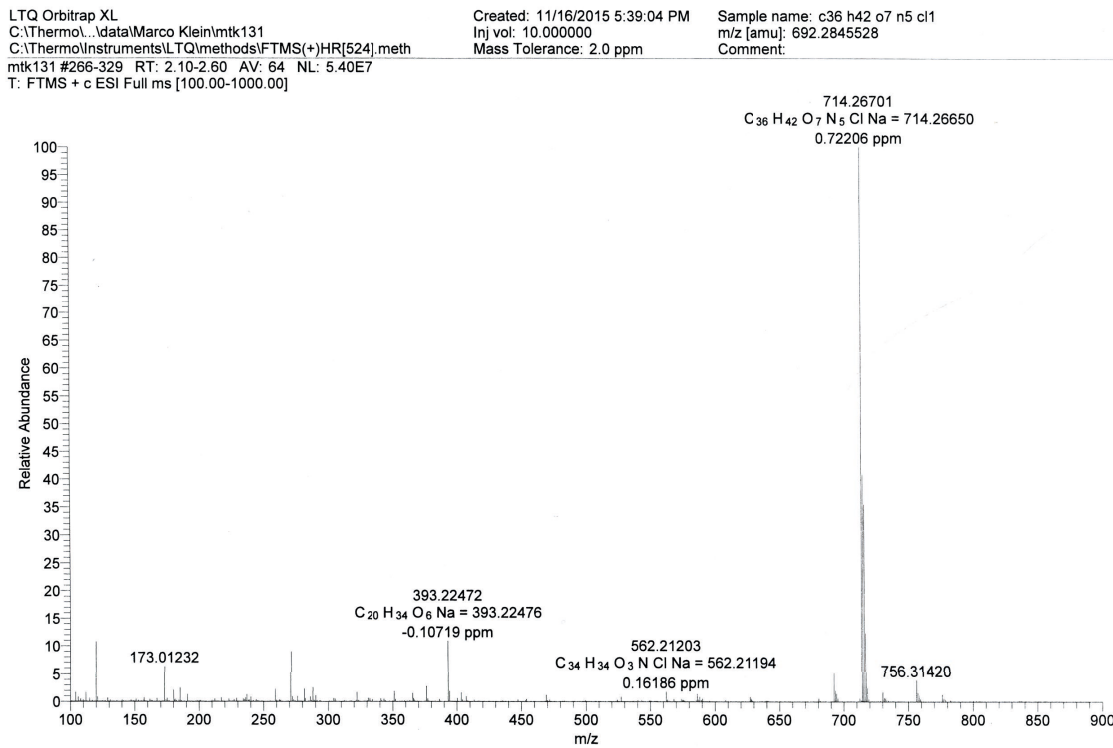
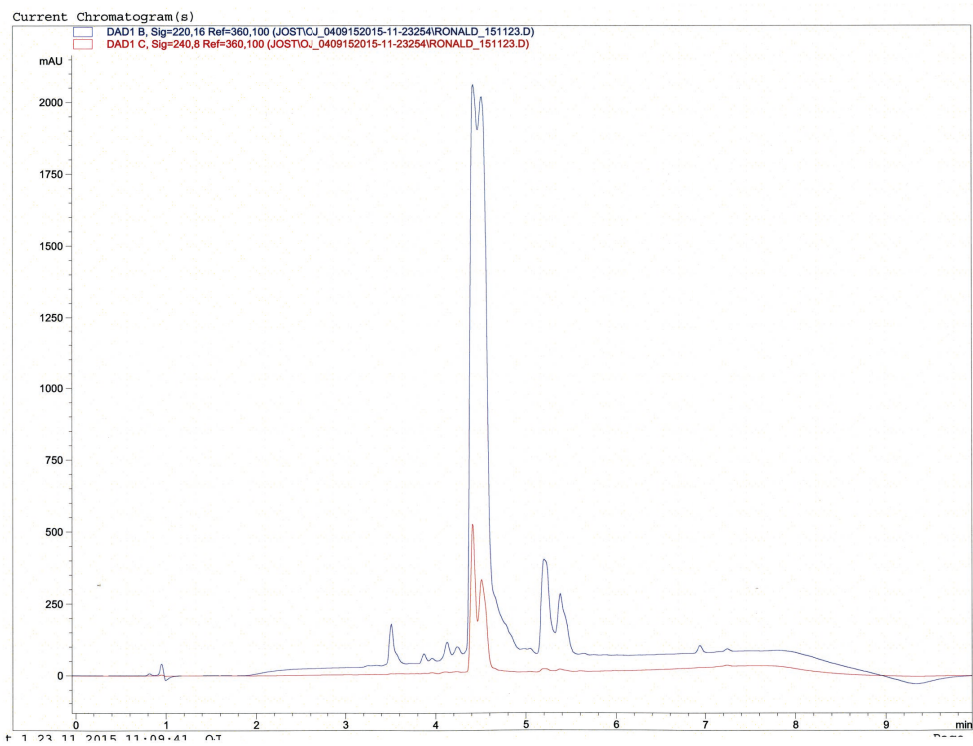
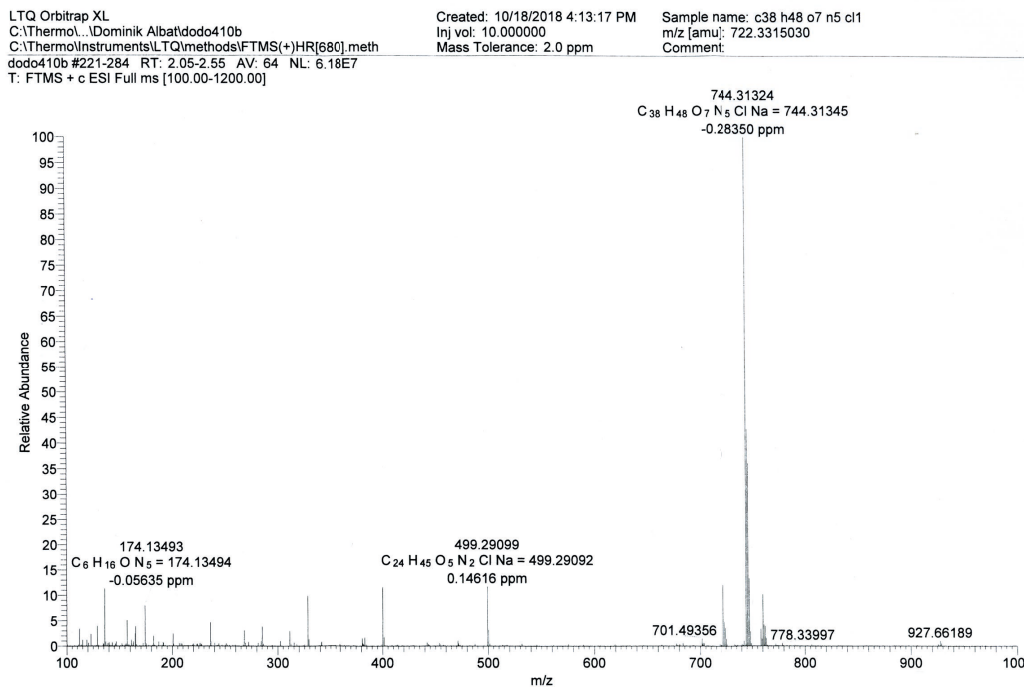


Fig. S40. Analysis of Ac-[2-Cl-Phe][ProM-2][ProM-12]-OMe

HPLC and ESI-FTMS of inhibitor **3a**, molecular weight 692.21 Da, visible as $[M+Na]^+$. The HPLC shows the typical double peak pattern mentioned before.



¹H-NMR:

(500 MHz, CDCl₃, mixture of rotamers) δ [ppm] = 7.36 – 7.13 (m, 4H, H35, H36, H37 and H38), 6.15 (d, ³J = 8.9 Hz, 0.7H, -NH^{rot1}), 6.15 (d, ³J = 9.0 Hz, 0.3H, -NH^{rot2}), 5.91 – 5.74 (m, 2.7H, H10 and H22^{rot1} and H23 or H22 and H23^{rot1}), 5.63 – 5.50 (m, 1H, H9), 5.20 – 5.12 (m, 1.4H, H12^{rot1} and H31^{rot1}), 5.09 (d, ³J = 12.0 Hz, 0.3H, H12^{rot2}), 4.97 (t, ³J = 8.0 Hz, 0.8H, H18^{rot1}), 4.84 (d, ³J = 8.5 Hz, 1.2H, H5 and H18^{rot2}), 4.80 – 4.69 (m, 1.3H, H2^{rot1}, H31^{rot2} and H22^{rot2} or H23^{rot2}), 4.42 – 4.36 (m, 0.7H, H21^{rot1}), 4.35 – 4.29 (m, 0.3H, H21^{rot2}), 4.22 – 4.17 (m, 0.7H, H15a^{rot1}), 4.13 – 4.07 (m, 0.3H, H15a^{rot2}), 3.99 – 3.88 (m, 1.5H, H27a and H27b^{rot1}), 3.72 (d, ³J = 17.7 Hz, 1.3H, H2^{rot2}), 3.67 (⁴pd, J = 5.0 Hz, 3H, H4), 3.64 – 3.54 (m, 1H, H15b), 3.52 – 3.43 (m, 0.5H, H27b^{rot2}), 3.37 (dd, ²J = 14.2, ⁴J = 3.8 Hz, 0.7H, H32a^{rot1}), 3.14 (dd, ³J = 13.0, ³J = 6.1 Hz, 0.3H, H32a^{rot2}), 3.05 – 2.92 (m, 1H, H11), 2.84 (dd, ³J = 14.2, ³J = 10.6 Hz, 0.7H, H32b^{rot1}), 2.52 – 2.44 (m, 0.8H, H19^{rot1}), 2.43 – 2.37 (m, 0.3H, H32b^{rot2}), 2.34 – 2.26 (m, 0.5H, H26^{rot1}), 2.24 – 1.87 (m, 6.7H, H19^{rot2}, H26^{rot2}, H27 and H14 or H20), 1.86 (s, 1H, H40^{rot1}), 1.79 (s, 2H, H40^{rot2}), 1.76 – 1.54 (m, 3H, H7 and H14 or H20), 1.47 (t, ³J = 7.5 Hz, 2H, H6), 1.01 – 0.90 (m, 6H).

¹³C-NMR:

(125 MHz, CDCl₃, mixture of rotamers) δ [ppm] = 172.3, 172.2 (2·s, C13); 171.6, 171.1 (2·s, C17); 170.5, 170.2 (3·s, C3 and C30); 169.4 (C39); 167.2, 166.7 (2·s, C25); 135.4, 134.9, 134.7, 134.6 (4·s, C33 and C34); 132.1, 131.8 (2·s, C38); 131.5, 130.7 (2·s, C22 and C23); 131.0 (C9); 129.6, 129.4, 128.5, 126.8, 126.6 (5·s, C35, C36 and C37); 123.1 (C10); 65.5, 64.6 (2·s, C24); 60.3, 60.2 (2·s, C12); 59.6, 59.2 (2·s, C21); 57.1, 56.4 (2·s, C18); 52.2 (C4); 51.5 (2·s, C5); 50.6, 50.4 (2·s, C31); 48.7 (2·s, C28); 47.5 (2·s, C15); 43.3 (C2); 42.4 (2·s, C11); 42.2, 41.2 (2·s, C6); 38.3, 38.0 (2·s, C26); 36.2 (2·s, C32); 31.5, 31.0 (4·s, C14 and C20); 28.6, 28.2 (2·s, C19); 25.1 (C7); 24.1, 22.2 (2·s, C27); 23.4, 23.3, 23.2, 21.8 (C8 and C40).

Fig. S41. Analysis of Ac-[2-Cl-Phe][ProM-2][ProM-17]-OMe

ESI-FTMS and assigned ¹H and ¹³C NMR chemical shifts (spectra printed on next page) of inhibitor **5a**, molecular weight 722.28 Da, visible as [M+Na]⁺.

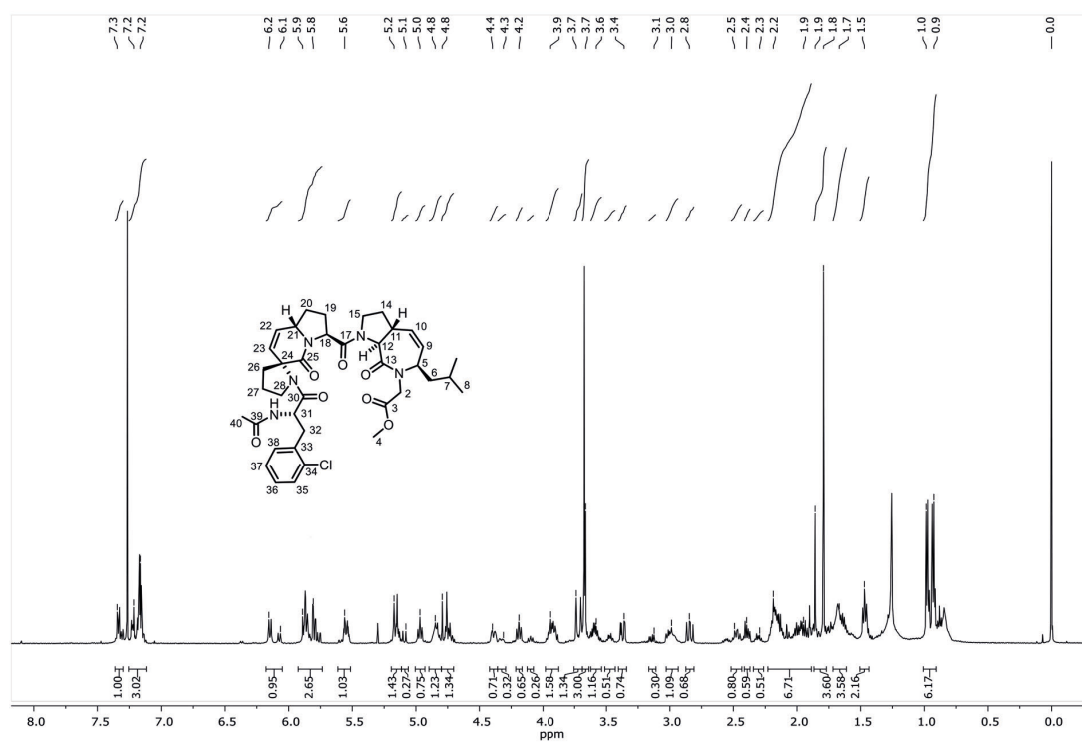


Figure 1: ^1H -NMR spectrum of Ac-[L-2-Cl-F][ProM-2][ProM-17]-OMe, 500 MHz.

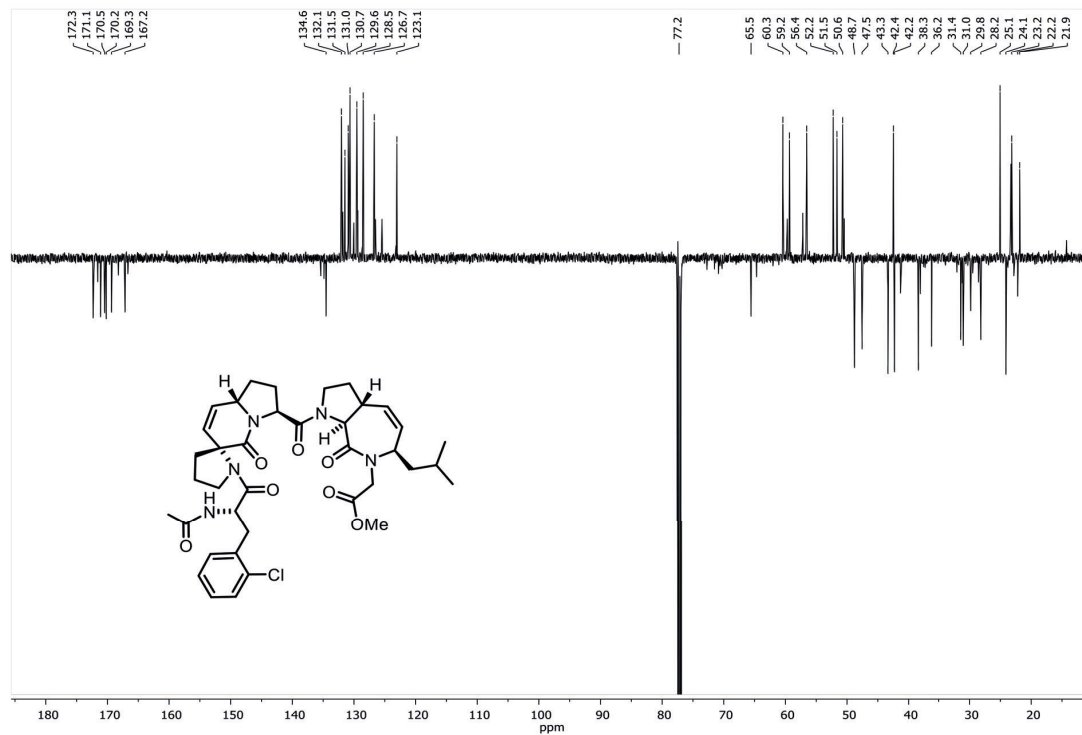
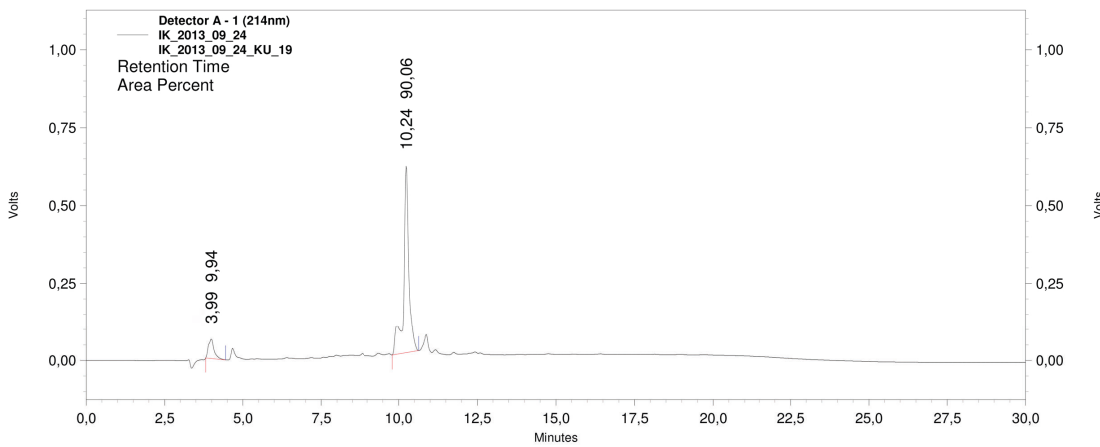


Figure 2: ^{13}C -NMR spectrum of Ac-[L-2-Cl-F][ProM-2][ProM-17]-OMe, 125 MHz.

Fig. S42. Analysis of Ac-[2-Cl-Phe][ProM-2][ProM-17]-OMe

1D ^1H and ^{13}C NMR spectra of inhibitor **5a**. Chemical shift tables printed on previous page lower panel.



Detector A - 1 (214nm)					
Pk #	Retention Time	Area	Area %	Height	Height %
1	3,992	772901	9,944	62387	9,395
2	10,242	6999337	90,056	601657	90,605

Totals		7772238	100,000	664044	100,000
--------	--	---------	---------	--------	---------

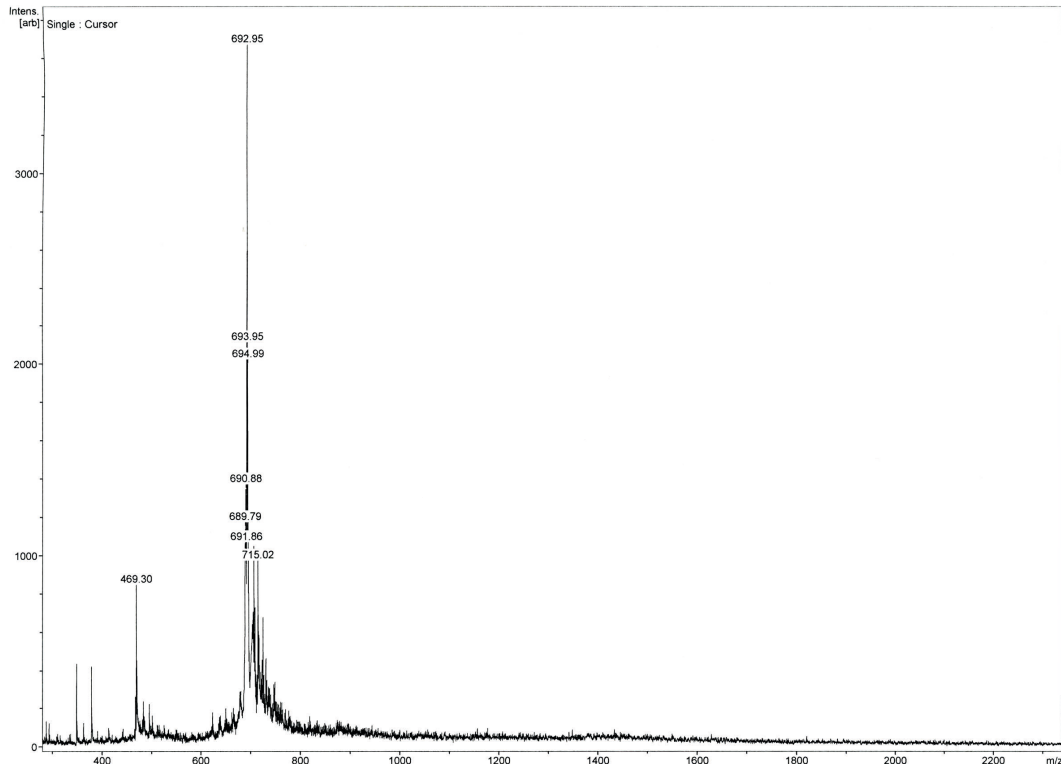
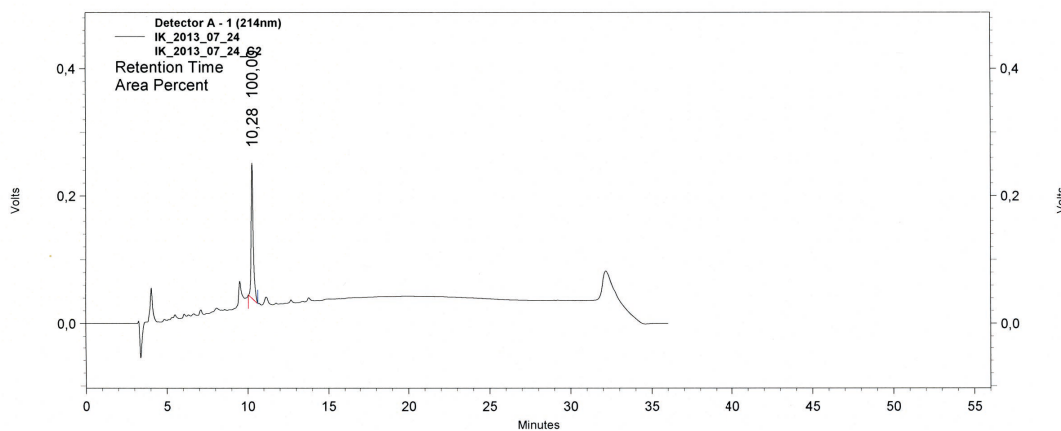


Fig. S43. Analysis of Ac-[2-Cl-Phe][ProM-2][ProM-9]-OH

HPLC and MALDI TOF of inhibitor **6b**, molecular weight 692.21 Da, visible as $[M+H]^+$ and $[M+Na]^+$. The additional small weight ion might belong to the termination product [ProM-2][ProM-9]-OH ($[M+H]^+$ 468.55 Da)



Detector A - 1 (214nm)		Area	Area %	Height	Height %
Pk #	Retention Time				
1	10,283	1851273	100,000	211237	100,000

Totals		1851273	100,000	211237	100,000
--------	--	---------	---------	--------	---------

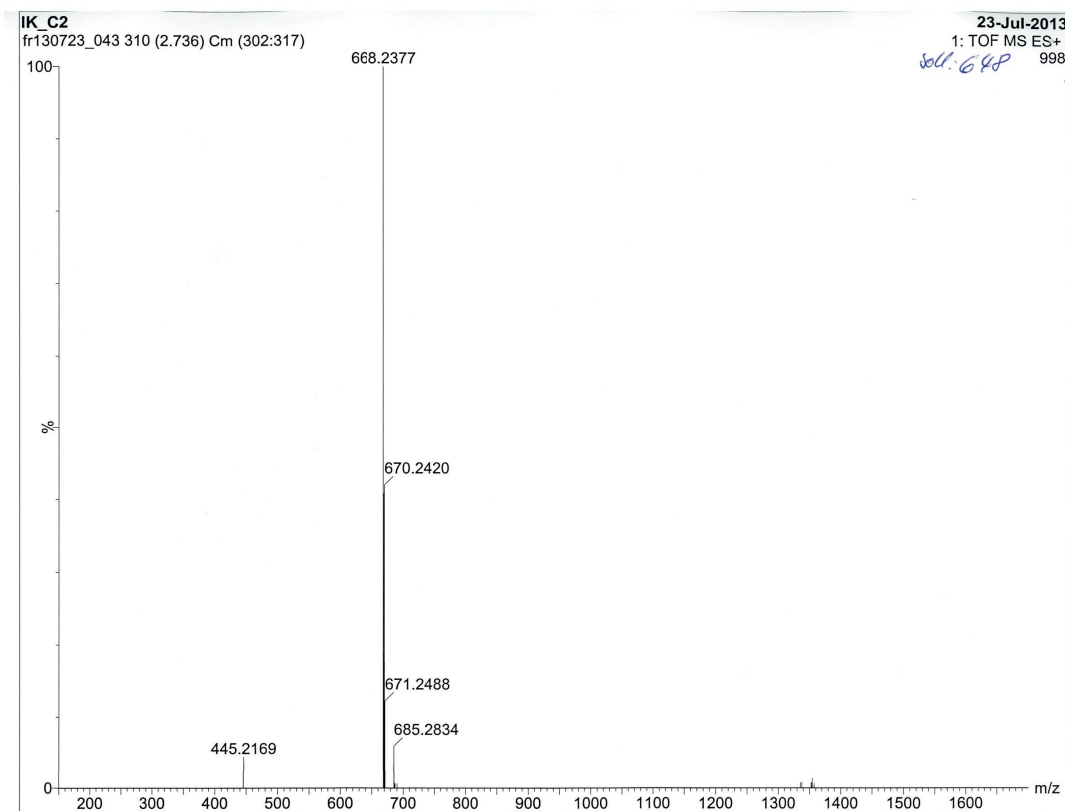


Fig. S44. Analysis of Ac-[2-Cl-Phe]PP[ProM-9]-OH

HPLC and MALDI TOF of inhibitor **6c**, molecular weight 668.19 Da, visible as $[M+H]^+$. The additional small weight ion might belong to the termination product PP[ProM-9]-OH ($[M+H]^+$ 444.52 Da)

- Zaminer J, et al. (2010) Addressing protein-protein interactions with small molecules: a pro-pro dipeptide mimic with a ppi helix conformation as a module for the synthesis of prd-binding ligands. *Angew Chem Int Ed Engl* 49:7111–7115.
- Reuter C, Neudörfl J, Schmalz HG (2010) Potassium (1-methoxy-carbonyl-2-methyl-prop-2-en-2-yl-ide)azinate. *Acta Crystallogr Sect E Struct Rep E66*.
- Huy P, Neudörfl J, Schmalz HG (2011) A practical synthesis of *Trans*-3-substituted proline derivatives through 1,4-addition. *Org Lett* 13(2):216–219.
- Hack V, et al. (2013) Efficient α -helix induction in a linear peptide chain by n-capping with a bridged-tricyclic diproline analogue. *Angew Chem Int Ed Engl* 52:9539–9543.
- Reuter C, et al. (2015) Design and stereoselective synthesis of prom-2: A spirocyclic diproline mimetic with polyproline type ii (ppi) helix conformation. *Chem Eur J* 21:8464–8470.
- Opitz R, et al. (2015) A modular toolkit to inhibit proline-rich motif-mediated protein-protein interactions. *Proc Natl Acad Sci U S A* 112:5011–5016.
- Chiha S, et al. (2018) Design and synthesis of building blocks for ppi-helix secondary-structure mimetics: A stereoselective entry to 4-substituted 5-vinylprolines. *Eur J Org Chem* 4:455–460.
- Dohmen S, et al. (2020) Pd-Catalyzed Asymmetric N-Allylation of Amino Acid Esters with Exceptional Levels of Catalyst Control: Stereo-Divergent Synthesis of ProM-15 and Related Bicyclic Dipeptide Mimetics. *Chem Eur J* 26(14):3049–3053.
- Heine HN (2000) Ph.D. thesis (Mathematisch-Naturwissenschaftlichen Fakultät I der Humboldt-Universität zu Berlin).
- Kabsch W (1993) Automatic processing of rotation diffraction data from crystals of initially unknown symmetry and cell constants. *J Appl Cryst* 26:795–800.
- Karplus PA, Diederichs K (2012) Linking crystallographic model and data quality. *Sci* 336:1030–1033.
- Karplus PA, Diederichs K (2015) Assessing and maximizing data quality in macromolecular crystallography. *Curr Opin Struct Biol* 22:60–68.
- McCoy AJ, et al. (2007) Phaser crystallographic software. *J Appl Crystallogr* 40:658–674.
- Johannesson P (1991) Moloc: using prolog for conceptual modelling. <http://www.moloc.ch>.
- Schüttelkopf AW, van Aalten DMF (2004) Prodrg: a tool for high-throughput crystallography of protein-ligand complexes. *Acta Crystallogr D Biol Crystallogr* 60:1355–1363.
- Lebedev AA, et al. (2012) Jligand: a graphical tool for the ccp4 template-restraint library. *Acta Crystallogr D Biol Crystallogr* 68:431–440.
- Adams PD, et al. (2010) Phenix: a comprehensive python-based system for macromolecular structure solution. *Acta Crystallogr D Biol Crystallogr* 66:213–221.
- Emsley P, Cowtan K (2004) Coot: model-building tools for molecular graphics. *Acta Crystallogr D Biol Crystallogr* 60:2126–2132.
- Pettersen EF, et al. (2004) UCSF Chimera—a visualization system for exploratory research and analysis. *J Comput Chem* 25(13):1605–1612.
- Goddard, T. D. and Kneller DG (year?) Sparky 3. University of California, San Francisco.
- Ren J, Liu S, Cui C, Ten Dijke P (2017) Invasive behavior of human breast cancer cells in embryonic zebrafish. *J Vis Exp* 122:e55459.
- Hamilton WC (1965) Significance tests on the crystallographic r factor. *Acta Crystallogr* 18:502–510.
- Brünger AT (1992) Free r value: a novel statistical quantity for assessing the accuracy of crystal structures. *Nature* 355(6359):472–475.
- Ball LJ, et al. (2000) Dual epitope recognition by the vasp evh1 domain modulates polyproline ligand specificity and binding affinity. *EMBO J* 19(18):4903–4914.
- Rost B (2001) Protein secondary structure prediction continues to rise. *J Struct Biol* 134:204–218.
- Buchan DWA, Minneci F, Nugent TCO, Bryson K, Jones DT (2013) Scalable web services for the psipred protein analysis workbench. *Nucleic Acids Res* 41:340–348.
- Pistor S, Chakraborty T, Walter U, Wehland J (1995) The bacterial actin nucleator protein acta of listeria monocytogenes contains multiple binding sites for host microfilament proteins. *Curr Biol* 5(5):517–525.
- Smith GA, Theriot JA, Portnoy DA (1996) The tandem repeat domain in the listeria monocytogenes acta protein controls the rate of actin-based motility, the percentage of moving bacteria, and the localization of vasodilator-stimulated phosphoprotein and profilin. *J Cell Biol* 135(3):647–660.
- Aurora, R and Rose GD (1998) Helix capping. *Protein Sci* 7:21–38.
- Beneken J, et al. (2000) Structure of the homer evh1 domain-peptide complex reveals a new twist in polyproline recognition. *Neuron* 26(1):143–154.
- Seneci P, et al. (2009) Rational design, synthesis and characterization of potent, non-peptidic smac mimics/xiap inhibitors as proapoptotic agents for cancer therapy. *Bioorg Med Chem* 17(16):5834–5856.
- Allard B, et al. (2015) Synthesis and evaluation of a (3R,6S,9S)-2-oxo-1-azabicyclo[4.3.0]nonane scaffold as a mimic of xaa-trans-pro in poly-l-proline type ii helix conformation. *Org Biomol Chem* 13(15):4562–4569.
- Bochicchio B, Tamburro AM (2002) Polyproline ii structure in proteins: identification by chiroptical spectroscopies, stability, and functions. *Chirality* 14(10):782–792.
- Williamson MP (1994) The structure and function of proline-rich regions in proteins. *Biochem J* 297 (Pt 2):249–260.
- Adzhubei AA, Sternberg MJ, Makarov AA (2013) Polyproline-ii helix in proteins: structure and function. *J Mol Biol* 425(12):2100–2132.
- Creamer T, Campbell M (2002) Determinants of the polyproline ii helix from modeling studies. *Adv Protein Chem* 62:263–282.
- Nguyen J, Turk C, Cohen F, Zuckermann R, Lim W (1998) Exploiting the basis of proline recognition by sh3 and ww domains: design of n-substituted inhibitors. *Sci* 282:2088–2092.
- Nguyen JT, et al. (2000) Improving sh3 domain ligand selectivity using a non-natural scaffold. *Chem Biol* 7:463–473.
- Li H, Lawrence D (2005) Acquisition of fyn-selective sh3 domain ligands via a combinatorial library strategy. *Chem Biol* 12:905–912.
- Mal TK, Matthews SJ, Kovacs H, Campbell ID, Boyd J (1998) Some nmr experiments and a structure determination employing a [15n,2h] enriched protein. *J Biomol NMR* 12:259–276.
- Feng S, Kasahara C, Rickles RJ, Schreiber SL (1995) Specific interactions outside the proline-rich core of two classes of Src homology 3 ligands. *Proc Natl Acad Sci U.S.A.* 92(26):12408–12415.
- Iglesias-Bexiga M, et al. (2015) WW domains of the yes-kinase-associated-protein (YAP) transcriptional regulator behave as independent units with different binding preferences for PPxY motif-containing ligands. *PLoS ONE* 10(1):e0113828.
- da Silva AJ, et al. (1997) Cloning of a novel T-cell protein FYB that binds FYN and SH2-domain-containing leukocyte protein 76 and modulates interleukin 2 production. *Proc Natl Acad Sci U.S.A.* 94(14):7493–7498.
- Sparks AB, Quilliam LA, Thorn JM, Der CJ, Kay BK (1994) Identification and characterization of Src SH3 ligands from phage-displayed random peptide libraries. *J Biol Chem* 269(39):23853–23856.